Analysis of Craniofacial Images using Computational Atlases and Deformation Fields

Hildur Ólafsdóttir

Kongens Lyngby 2007
IMM-PHD-2007-187

Technical University of Denmark
Informatics and Mathematical Modelling
Building 321, DK-2800 Kongens Lyngby, Denmark
Phone +45 45253351, Fax +45 45882673
reception@imm.dtu.dk
www.imm.dtu.dk

IMM-PHD: ISSN 0909-3192

Preface

This thesis was prepared at the Image Analysis and Computer Graphics group at DTU Informatics and submitted to the Technical University of Denmark – DTU, in partial fulfilment of the requirements for the degree of Doctor of Philosophy, Ph.D., in Applied Mathematics. The project was funded by a Ph.D.-grant from DTU.

The work herein represents selected parts of the research work carried out in the Ph.D. period. The thesis consists of five research papers and an introductory part containing an overview and background information.

The work was carried out in a close collaboration with the 3D Craniofacial Image Research Lab – an inter-disciplinary research unit at the School of Dentistry, University of Copenhagen. Part of the research work was carried out at the Research group for Computational Imaging & Simulation Technologies in Biomedicine (CISTIB), Pompeu Fabra University, Barcelona.

The project was supervised by Associate Professor Bjarne K. Ersbøll and Professor Rasmus Larsen, both at DTU Informatics.

Kgs. Lyngby, April 2008

Hildur Ólafsdóttir

Hildur Ólafsdóttir

Acknowledgements

This section is devoted to the several people, who have put their effort, time and energy into this thesis work.

First of all, I want to express my gratitude to my advisors, Bjarne K. Ersbøll and Rasmus Larsen for their engagement in the project through discussions, good advice and contributions to the papers. Additionally, they are thanked for providing an excellent professional and social framework at the image group.

It has been extremely pleasant to work at the 3D Lab. The relaxed social atmosphere and professional feed-back was as good as it could be. First of all, I would like to thank Tron A. Darvann for his immense contribution. Everything from data preprocessing, assisting with visualisations and practical programming issues to discussing theory and spending time on criticising every detail until he was convinced. Nuno V. Hermann deserves many thanks for bearing with me when I kept asking her about the anatomical nomenclature. Another and greater contribution of hers was the expertise she provided in manually annotating the images and rating our methods for extensive validation. Per Larsen is also thanked for his good suggestions and support and my deepest gratitude goes to the head of 3D Lab, Sven Kreiborg for establishing collaborations and explaining me all about Crouzon syndrome in a way an engineer could understand. I am also grateful to Stéphanie Lanche, who did her M.Sc. project at DTU and 3D Lab, for a great collaboration and fruitful discussions. All the other people staying at the lab for a shorter or longer period, thanks a lot for a great time.

The time I spent at the image analysis group at DTU Informatics was also excellent. Special thanks go to my office mates for most of the period, Karl

Sjöstrand and Mikkel B. Stegmann for their friendship, support, fun conference trips etc. I am extremely grateful to Karl, who was willing to take the time to discuss my projects even though he was turning in his thesis a couple of weeks later and for later reviewing this thesis in great detail. Many thanks to Mikkel who supervised my MSc. thesis and allowed me to continue to ask him for advice during my Ph.D. until he stopped at DTU Informatics. I am grateful to Michael Sass Hansen for carefully reviewing the thesis and for the smooth collaboration. Special thanks go to Line H. Clemmensen, who corrected the Danish abstract of the thesis. All the other past and present Ph.D. students at DTU Informatics are thanked for excellent discussions and social activities during the years. Eina, Tove and Kirsten are thanked for making all the practical issues so simple.

The three months I spent at CISTIB, UPF, Barcelona were extremely fruitful. Especially thanks to Alejandro F. Frangi for his many ideas and discussions and to Estanislao Oubel for an excellent collaboration. I am grateful to all the other people at CISTIB for making my stay in Barcelona unforgettable.

There are many people behind the datasets I got the chance to work on. I am indebted to the people at St. Louis Children's Hospital, who were involved in the data collection for all three studies. Many thanks to the Department of Physiology, Anatomy and Genetics at Oxford University for growing the mice for the Crouzon study. I am grateful to the collaboration involving the unicoronal synostosis data. In addition to St. Louis Children's hospital, Helsinki University Central Hospital and Copenhagen University Hospital gathered data for the particular study.

Finally, warm thanks to my fiance Thórhallur and our son Halldór for taking care of each other during the thesis writing period, even though Thórhallur was to hand in his own thesis only a couple of months later.

Abstract

The topic of this thesis is automatic analysis of craniofacial images. The methods proposed and applied contribute to the scientific knowledge about different craniofacial anomalies, in addition to providing tools for detailed and robust analysis of craniofacial images for clinical and research purposes.

The basis for most of the applications is non-rigid image registration. This approach brings one image into the coordinate system of another resulting in a deformation field describing the anatomical correspondence between the two images. A computational atlas representing the average anatomy of a group may be constructed and brought into correspondence with a set of images of interest. Having established such a correspondence, various analyses may be carried out. This thesis discusses two types of such analyses, i.e. statistical deformation models and novel approaches for the quantification of asymmetry. The analyses are applied to the study of three different craniofacial anomalies.

The craniofacial applications include studies of Crouzon syndrome (in mice), unicoronal synostosis plagiocephaly and deformational plagiocephaly. Using the proposed methods, the thesis reveals novel findings about the craniofacial morphology and asymmetry of Crouzon mice. Moreover, a method to plan and evaluate treatment of children with deformational plagiocephaly, based on asymmetry assessment, is established. Finally, asymmetry in children with unicoronal synostosis is automatically assessed, confirming previous results based on manual reference points *and* providing a higher level of detail.

Resumé

Denne afhandling omhandler automatisk analyse af kraniofaciale billeder. De anvendte og foreslåede metoder bidrager til forståelsen af kraniofaciale misdannelser, samt skaffer værktøjer til detaljeret og robust analyse af kraniofaciale billeder til kliniske og forskningsbaserede formål.

Ikke-rigid billedregistrering er den grundlæggende metode som er brugt i de fleste af anvendelserne i afhandlingen. Denne metode transformerer et billede over i koordinatsystemet til et andet billede. Transformationen giver et deformationsfelt som beskriver den anatomiske korrespondance mellem de to billeder. Et atlas, som repræsenterer den gennemsnitlige anatomi af en gruppe af billeder, kan konstrueres og bringes i korrespondance med et sæt billeder af interesse. Ved hjælp af en sådan korrespondance kan adskillige analyser gennemføres. Denne afhandling diskuterer to typer af analyser, nemlig statistiske deformationsmodeller og nye metoder til kvantificering af asymmetri. Analyserne er benyttet til at studere tre forskellige kraniofaciale misdannelser.

De kraniofaciale anvendelser inkluderer studier af Crouzon syndrom (hos mus), enkeltsidig coronal synostose plagiocefali og lejringsbetinget plagiocefali. Ved hjælp af de foreslåede metoder fremkommer der i afhandlingen ny viden om kraniofacial morfologi og asymmetri i Crouzon-mus. Desuden er der udviklet en metode til planlægning og evaluering af behandling af spædbørn med lejringsbetinget plagiocefali. Endelig er asymmetri hos børn med enkeltsidig coronal synostose plagiocefali undersøgt automatisk, og tidligere studier, baseret på landmarks, er bekræftet i højere rumlig opløsning.

Contents

Part I

Summary

Chapter 1

Introduction

The skull of a newborn baby is composed of five major bones, separated by growth zones, also commonly called sutures. For the brain to grow normally, the sutures remain open and gradually grow together, forming the adult skull. Several factors can disturb the normal growth process. Conditions associated with disturbed craniofacial development are often referred to as *craniofacial anomalies*.

In the treatment of children with craniofacial anomalies, 3D images play an integrated and crucial role. By use of volumetric 3D imaging techniques, such as Computed Tomography (CT) and Magnetic Resonance Imaging (MRI), detailed views of the internal anatomy are presented. Currently, most of the analysis of these images is restricted to a qualitative inspection by a specialist, while quantitative analysis relies on time-consuming manual measurements on a limited number of reference points.

The aim of this thesis is to automate the analysis using modern image processing techniques. Using such methods greatly increases the level of detail and reproducibility of the quantitative analyses during diagnosis and treatment. Furthermore, in order to better understand abnormal craniofacial shape and growth caused by different craniofacial anomalies, population studies may be carried out, studying the craniofacial anatomy and pathology in detail.

Hence, the overall goal of this thesis is to provide answers to questions such as,

1. What craniofacial syndrome does a particular individual have and how severe is it? (differential dignosis)
2. What changes took place since the last examination? (evaluation of growth and treatment progression)
3. What are the typical features of a particular type of craniofacial anomaly, and how do they vary in a population? (population studies)

In order to answer these questions, it is essential to be able to compare image data from one time point to another or from patient to patient. To do so, detailed anatomical information about every image element or correspondence of the anatomies are needed. A strong candidate methodology, with the potential to provide answers to the questions above, is *non-rigid image registration*. This approach accurately deforms one image into the coordinate system of another, enabling a quantitative comparison on a voxel-to-voxel basis. Additionally, the deformations resulting from the registration may be analysed to assess the shape and geometry of the different parts of the anatomy. The possibility of using deformations for analysing difference in (craniofacial) anatomy was noted already in 1917 by D´Arcy Thompson [219] and Figure 1.1 shows some of his examples.

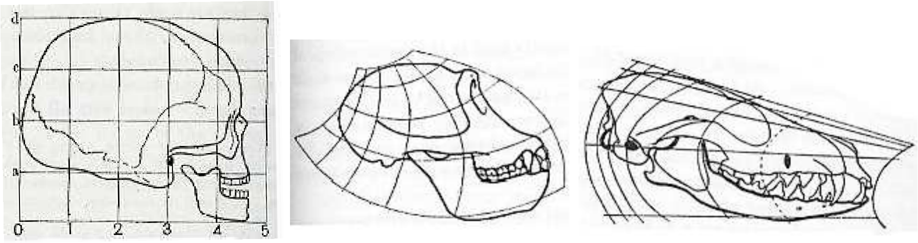

(a) (b) (c)

Figure 1.1: From [219]. Comparison of the shape of (a) a human skull, (b) a chimpanzee skull and (c) a dog skull. The deformation grids represent the correspondence to a human skull.

While D'Arcy Thompson's approach was manual and in 2D, modern non-rigid image registration is able to provide 3D deformation fields fully automatically. Although one of the pioneering theoretical developments of non-rigid registration algorithms was first applied to the craniofacial region [30], few advances have been made in applying this technology to craniofacial data until recent promising demonstrations by [119] and [26]. This thesis further adds to these applications by presenting the use of non-rigid registration to study and analyse craniofacial anomalies.

1.1 Objectives

The main topic of this thesis is application of non-rigid registration to craniofacial images in order to partly or fully answer the three questions stated above.

In particular, the thesis focuses on the analysis of craniofacial shape and asymmetry in three craniofacial anomalies: Crouzon syndrome (in mice), unicoronal synostosis plagiocephaly and deformational plagiocephaly.

From a technical point of view the objectives are the creation and applications of a computational atlas. This includes the analysis of shape and geometry from deformation fields using statistical modelling techniques. Moreover, it involves the point-wise quantification and statistical modelling of asymmetry from deformation fields.

1.2 Thesis overview

This thesis is composed of two parts. The first gives a background and overview of the contributions and basic methods applied in the thesis. The second part includes a selection of papers and technical reports written during the project period. Each paper comprises a chapter and a brief description of each of them is given below. The chapters are all inter-connected and the main theme is the analysis of shape and asymmetry using deformation fields from non-rigid registration. The chapters reach from a direct analysis of the deformations in Chapter 7, to statistical deformation models in Chapters 8 and 9 and quantification of asymmetry from deformations in Chapters 10 and 11. Reading the thesis in full should be carried out by reading Chapter 1- 5 and before proceeding to the discussion in Chapter 6, Part II should be read.

- **Chapter 7** describes the creation of computational, craniofacial mouse atlases for studying the Crouzon mouse model. Two types of atlases are constructed, using affine and non-rigid registration. It is demonstrated how linear parameters may be assessed and the performance with respect to the two different atlases is analysed. Furthermore, deformation fields from non-rigid registration of a normal atlas to a Crouzon atlas are inspected and analysed.
- **Chapter 8** presents craniofacial statistical deformation models using principal components analysis (PCA). Intra- and inter-group models are created and discussed. With respect to the ability to discriminate between the mouse groups studied in this chapter, only the first mode of variation for the inter-group models is applicable.

- **Chapter 9** discusses statistical deformation models in more detail. It presents the use of sparse principal components analysis (SPCA) to localise the discriminative modes of variations. Compared to PCA and independent component analysis (ICA), SPCA performs better with respect to discriminative ability in the particular mouse models studied here.
- **Chapter 10** describes a novel method for defining asymmetry in surface scans of infants with deformational plagiocephaly. Bilateral asymmetry is defined in each point of a deformed symmetric template by the ratio of left and right distances to a pre-defined midpoint. Finally, a statistical model of asymmetry is presented.
- **Chapter 11** presents another asymmetry measure, based on the deformation field acquired by image registration of a subject image to a symmetric reference image. Asymmetry is defined in each voxel (or each point) by comparing the displacement vectors on the left and right side of the head. This approach gives a measure of asymmetry in length units (mm), while the approach from Chapter 10 gives a relative measure of asymmetry (in terms of a dimensionless number).

1.3 Publications

The publications related to part II of the thesis are listed below. The citation of the paper covering each chapter is written in bold face.

Chapter 7

[162] H. Ólafsdóttir, T.A. Darvann, N.V. Hermann, E. Oubel, B.K. Ersbøll, A.F. Frangi, P. Larsen, C.A. Perlyn, G.M. Morriss-Kay, and S. Kreiborg. Computational mouse atlases and their application to automatic assessment of craniofacial dysmorphology caused by the Crouzon mutation Fgfr2$^{\mathrm{C342Y}}$. *Journal of Anatomy*, 211(1):37–52, 2007.

[158] H. Ólafsdóttir, E. Oubel, A.F. Frangi, T.A. Darvann, N.V. Hermann, S. Kreiborg, P. Larsen, B.K. Ersbøll, C.A. Perlyn, and G.M. Morriss-Kay. Automatic assessment of global craniofacial differences between Crouzon mice and wild-type mice in terms of the cephalic index. In P. Larsen T.A. Darvann, N.V. Hermann and S. Kreiborg, editors, *MICCAI 2006 workshop: Craniofacial Image Analysis for Biology, Clinical Genetics, Diagnostics and Treatment*, pages 49–57, 2006.

[157] H. Ólafsdóttir, T.A. Darvann, E. Oubel, A.F. Frangi, N.V. Hermann, B.K. Ersbøll, and C.A. Perlyn. Towards describing Crouzon syndrome via a craniofacial atlas. In S.I. Olsen, editor, *15th Danish Conference on Pattern Recognition and Image Analysis (DSAGM)*, pages 108–114, 2006.

Chapter 8

[**160**] H. Ólafsdóttir, T.A. Darvann, Ersboll B.K., N.V. Hermann, E. Oubel, R. Larsen, A.F. Frangi, P. Larsen, C.A. Perlyn, G.M. Morriss-Kay, and S. Kreiborg. Craniofacial statistical deformation models of wild-type mice and Crouzon mice. In J.P.W. Pluim and J.M. Reinhardt, editors, *Medical Imaging 2007: Image Processing*, volume 6512, page 65121C. SPIE, 2007.

Chapter 9

[**163**] H. Ólafsdóttir, M.S. Hansen, K. Sjöstrand, T.A. Darvann, N.V. Hermann, E. Oubel, B.K. Ersbøll, R. Larsen, A.F. Frangi, P. Larsen, C.A. Perlyn, G.M. Morriss-Kay, and S. Kreiborg. Sparse statistical deformation model for the analysis of craniofacial malformation in the Crouzon mouse. In B.K. Ersbøll and K.S. Pedersen, editors, *Scandinavian Conference on Image Analysis 2007*, volume 4522 of *LNCS*, pages 112–121. Springer, 2007.

[91] M.S. Hansen, H. Ólafsdóttir, T.A. Darvann, N.V. Hermann, E. Oubel, R. Larsen, B.K. Ersbøll, A.F. Frangi, P. Larsen, C.A. Perlyn, G.M. Morris-Kay, and S. Kreiborg. Estimation of independent non-linear deformation modes for analysis of craniofacial malformations in Crouzon mice. In J.A. Fessler M. Wernick, editor, *2007 IEEE International Symposium on Biomedical Imaging*. IEEE, 2007.

Chapter 10

[**121**] S. Lanche, T.A. Darvann, H. Ólafsdóttir, N.V. Hermann, A.E. Van Pelt, D. Govier, M.J. Tenenbaum, S. Naidoo, P. Larsen, S. Kreiborg, R. Larsen, and A.A. Kane. A statistical model of head asymmetry in infants with deformational plagiocephaly. In B.K. Ersbøll and K.S. Pedersen, editors, *Scandinavian Conference on Image Analysis 2007*, volume 4522 of *LNCS*, pages 898–907. Springer, 2007.

[122] S. Lanche, T.A. Darvann, H. Ólafsdóttir, N.V. Hermann, A.V. Pelt, D. Gover, M.J. Tenebaum, S. Naidoo, P. Larsen, S. Kreiborg, R. Larsen, and A.A. Kane. A method for evaluating treatment in infants with deformational plagiocephaly. In *Image Analysis and In-Vivo Pharmacology*, 2007. (abstract).

[172] A. Van Pelt, T.A. Darvann, D. Govier, S. Naidoo, M.J. Tenebaum, N.V. Hermann, S. Lanche, H. Ólafsdóttir, P. Larsen, R. Larsen, S. Kreiborg, and A.A. Kane. Longitudinal evaluation of 3D asymmetry following orthotic helmet treatment of deformational plagiocephaly. In *Annual Meeting of the Americal Cleft Palate Craniofacial Association (ACPA) (accepted)*, 2008 (abstract).

[123] S. Lanche, T.A. Darvann, H. Ólafsdóttir, N.V. Hermann, A.E. Van Pelt, D. Govier, M.J. Tenenbaum, S. Naidoo, P. Larsen, S. Kreiborg, R. Larsen, and A.A. Kane. Validation of a statistical model of head asymmetry in infants with deformational plagiocephaly. In *Mouth and Face Forum 2008 - in silico Dentistry, Osaka, Japan (accepted)*, 2008.

Chapter 11

[**166**] H. Ólafsdóttir, S. Lanche, T.A. Darvann, N.V. Hermann, K. Sjöstrand, E. Oubel, A.F. Frangi, P. Larsen, C.A. Perlyn, D. Govier, H.D. Hove, J. Hukki, A.A. Kane, G.M. Morriss-Kay, S. Kreiborg, B.K. Ersbøll, and R. Larsen. A volumetric quantification of asymmetry using non-rigid registration. *Transactions on Medical Imaging (submitted)*, 2008.

[164] H. Ólafsdóttir, S. Lanche, T.A. Darvann, N.V. Hermann, R. Larsen, B.K. Ersbøll, E. Oubel, A.F. Frangi, P. Larsen, C.A. Perlyn, G.M. Morriss-Kay, and S. Kreiborg. A point-wise quantification of asymmetry using deformation fields. application to the study of the Crouzon mouse model. In N. Ayache, S. Ourselin, and A. Maeder, editors, *Medical Image Computing and Computer-Assisted Intervention*, volume 4792 of *Lecture Notes in Computer Science*, pages 452–459, 2007.

[165] H. Ólafsdóttir, T.A. Darvann, N.V. Hermann, P. Larsen, Govier D., A.A. Kane, R. Larsen, B.K. Ersbøll, and S. Kreiborg. Non-rigid registration in craniofacial image analysis: Application to the study of unicoronal synostosis. In *Mouth and Face Forum 2008 - in silico Dentistry, Osaka, Japan (invited contribution)*, 2008.

[55] T.A. Darvann, H. Ólafsdóttir, N.V. Hermann, P. Larsen, S. Lanche, R. Larsen, B.K. Ersbøll, D. Govier, A.E. Van Pelt, A.A. Kane, and S. Kreiborg. On the measurement of craniofacial asymmetry. In *Mouth and Face Forum 2008 - in silico Dentistry, Osaka, Japan (invited contribution)*, 2008.

Other published papers outside the theme of this thesis are listed below.

Journal papers

[203] M.B. Stegmann, H. Ólafsdóttir, and H.B.W. Larsson. Unsupervised motion-compensation of multi-slice cardiac perfusion MRI. *Medical Image Analysis*, 9(4):394–410, 2005.

Conference papers

[4] R.J. Anderson, T.A. Darvann, H. Ólafsdóttir, D.W. Hansen, R. Larsen, N.V. Hermann, P. Larsen, A.E. Van Pelt, D. Govier, M.J. Tenenbaum, S. Naidoo, , S. Kreiborg, and A.A. Kane. Automated landmarking of 3d infant face surfaces using 2d active appearance models. In *Mouth and Face Forum 2008 - in silico Dentistry, Osaka, Japan (accepted)*, 2008.

[116] S. Kreiborg, P. Larsen, T.A. Darvann, H. Ólafsdóttir, N.V. Hermann, and H.H. Dahlgard. 3D craniofacial growth analysis. In *Mouth and Face Forum 2008 - in silico Dentistry, Osaka, Japan (invited contribution)*, 2008.

[92] M.S. Hansen, H. Ólafsdóttir, K. Sjöstrand, H.B. Larsson, M.B. Stegmann, and R. Larsen. Ischemic segment detection using the support vector domain description. In The International Society for Optical Engineering (SPIE), editor, *International Symposium on Medical Imaging*, 2007.

[93] M.S. Hansen, K. Sjostrand, H. Ólafsdóttir, H.B.W. Larsson, M.B. Stegmann, and R. Larsen. Robust pseudo-hierarchical support vector clustering. In *Scandinavian Conference on Image Analysis 2007*, volume 4522 of *Lecture Notes in Computer Science*, pages 808–17, 2007.

[155] H. Ólafsdóttir. Nonrigid registration of myocardial perfusion MRI. In *Proc. Svenska Symposium i Bildanalys, SSBA 2005, Malmø, Sweden*. SSBA, 2005.

[159] H. Ólafsdóttir, M.B. Stegmann, B.K. Ersbøll, and H.B. Larsson. A comparison of FFD-based nonrigid registration and AAMs applied to myocardial perfusion MRI. In *International Symposium on Medical Imaging 2006, San Diego, CA*, volume 6144. The International Society for Optical Engineering (SPIE), 2006.

[156] H. Ólafsdóttir, M.B. Stegmann, and H.B.W. Larsson. Automatic assessment of cardiac perfusion MRI. In *Medical image computing and computer assisted intervention*, LNCS, 2004.

[217] H.H. Thodberg and H. Ólafsdóttir. Adding curvature to minimum description length shape models. In *Proceedings of the British Machine Vision Conference*, volume 2, pages 251–260, 2003.

Conference abstracts

[161] H. Ólafsdóttir, T.A. Darvann, N.V. Hermann, B.K. Ersbøll, E. Oubel, R. Larsen, A.F. Frangi, P. Larsen, C.A. Perlyn, G.M. Morriss-Kay, and S. Kreiborg. Automatic detection of wild-type mouse cranial sutures. In *Image Analysis and In-Vivo Pharmacology*, 2007.

[197] K.V. Skoglund, M.B. Stegmann, C. Ryberg, H. Ólafsdóttir, and E. Rostrup. Estimation and perturbation of the mid-sagittal plane and its effects on corpus callosum morphometry. In *Proc. International Society of Magnetic Resonance In Medicine - ISMRM 2005, Miami, Florida, USA*. ISMRM, 2005.

Co-authors of the publications in Part II and their affiliations are listed below in alphabetical order.

- Tron A. Darvann
  3D Craniofacial Image Research Laboratory, (School of Dentistry, University of Copenhagen; Copenhagen University Hospital; DTU Informatics, Technical University of Denmark), Copenhagen Denmark.
- Bjarne K. Ersbøll
  DTU Informatics, Technical University of Denmark, DTU, Denmark.
- Alejandro F. Frangi
  Research group for Computational Imaging & Simulation Technologies in Biomedicine (CISTIB), Information & Communication Technologies Department, Universitat Pompeu Fabra, Barcelona, Spain.
  Networking Center on Biomedical Research - CIBER-BBN, Barcelona, Spain.
- Daniel Govier
  Division of Plastic and Reconstructive Surgery, Washington University School of Medicine, St. Louis, MO, USA.
- Michael Sass Hansen
  DTU Informatics, Technical University of Denmark, DTU, Denmark.
- Nuno V. Hermann
  3D Craniofacial Image Research Laboratory, (School of Dentistry, University of Copenhagen; Copenhagen University Hospital; DTU Informatics, Technical University of Denmark), Copenhagen Denmark.
  Department of Pediatric Dentistry and Clinical Genetics, School of Dentistry, Faculty of Health Sciences, University of Copenhagen, Copenhagen, Denmark.
- Hanne Dahlgaard Hove
  Department of Clinical Genetics, The Juliane Marie Centre, Copenhagen University Hospital, Copenhagen, Denmark.
- Jyri Hukki
  Cleft Palate and Craniofacial Center, Helsinki University Central Hospital, Helsinki, Finland.
- Alex A. Kane
  Division of Plastic and Reconstructive Surgery, Washington University School of Medicine, St. Louis, MO, USA.
- Sven Kreiborg
  3D Craniofacial Image Research Laboratory, (School of Dentistry, University of Copenhagen; Copenhagen University Hospital; DTU Informatics, Technical University of Denmark), Copenhagen Denmark.
  Department of Pediatric Dentistry and Clinical Genetics, School of Dentistry, Faculty of Health Sciences, University of Copenhagen, Copenhagen, Denmark.
  Department of Clinical Genetics, The Juliane Marie Centre, Copenhagen University Hospital, Copenhagen, Denmark.

- Stéphanie Lanche
  DTU Informatics, Technical University of Denmark, DTU, Denmark.
  3D Craniofacial Image Research Laboratory, (School of Dentistry, University of Copenhagen; Copenhagen University Hospital; DTU Informatics, Technical University of Denmark), Copenhagen Denmark.
  Ecole Supérieure de Chimie Physique Electronique de Lyon (ESCPE Lyon.), France.
- Per Larsen
  3D Craniofacial Image Research Laboratory, (School of Dentistry, University of Copenhagen; Copenhagen University Hospital; DTU Informatics, Technical University of Denmark), Copenhagen Denmark.
- Rasmus Larsen
  DTU Informatics, Technical University of Denmark, DTU, Denmark.
- Gillian M. Morriss-Kay
  Department of Physiology, Anatomy and Genetics, Oxford University, Oxford, UK
- Sybill Naidoo
  Division of Plastic and Reconstructive Surgery, Washington University School of Medicine, St. Louis, MO, USA.
- Estanislao Oubel
  Research group for Computational Imaging & Simulation Technologies in Biomedicine (CISTIB), Information & Communication Technologies Department, Universitat Pompeu Fabra, Barcelona, Spain.
  Networking Center on Biomedical Research - CIBER-BBN, Barcelona, Spain.
- Andrea E. Van Pelt
  Division of Plastic and Reconstructive Surgery, Washington University School of Medicine, St. Louis, MO, USA.
- Chad A. Perlyn
  Division of Plastic and Reconstructive Surgery, Washington University School of Medicine, St. Louis, MO, USA.
- Karl Sjöstrand
  EXINI Diagnostics AB, Lund, Sweden.
- Marissa J. Tenenbaum
  Division of Plastic Surgery, Washington University School of Medicine, St. Louis, MO, USA.

Chapter 2

Skull Anatomy and Craniofacial Anomalies

This chapter gives a brief introduction to the basic anatomy of the skull and introduces the craniofacial anomalies studied in this thesis.

2.1 Skull Anatomy

The skull of an infant is composed of five major bones, two *frontal bones*, two *parietal bones* and the *occipital bone*. The bones are separated by growth zones, also referred to as *cranial sutures* allowing the skull and brain to grow normally. The growth zones are gradually closing until adulthood. The major sutures are the *metopic suture*, which extends from the top of the head to the forehead and separates the frontal bones; the *coronal suture*, which extends from one ear to the other and separates the frontal bones from the parietal bones; the *sagittal suture*, which extends from the front of the head to the back of the head and separates the parietal bones; and finally the *lambdoid suture*, which extends across the back of the head and separates the parietal bones from the occipital bone.

The sutures meet at soft areas called *fontanelles*, made of strong membranes. The space where the parietal bones and the frontal bones meet is called the *anterior fontanelle*. This opening in the skull closes when the child is approximately two years old. The second soft area is named the *posterior fontanelle*. Here, the parietal bones and the occipital bone meet and this fontanelle closes earlier, typically when the child is only two months old. Figure 2.1 shows a drawing of the major bones and sutures of the skull.

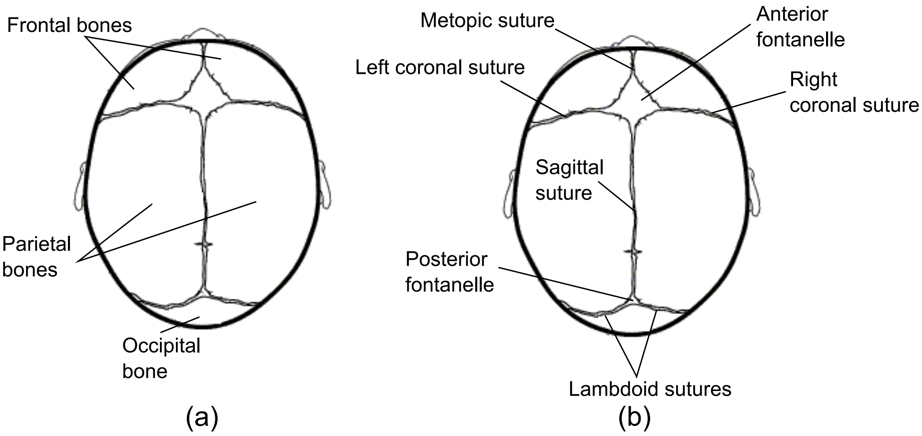

Figure 2.1: Schematic figure of a child´s skull, seen from above. (a) Bones labelled. (b) Sutures and fontanelles labelled.

All structures of the skull are of interest in this thesis, and the most important parts are labelled in Figure 2.2.

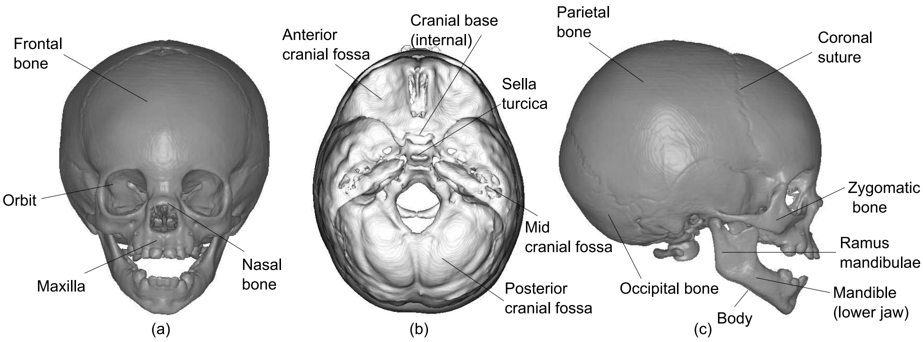

Figure 2.2: The human skull at approximately eighteen months of age. A surface representation of one of the CT scans used in this thesis. (a) Frontal view, (b) Cut, top view, (c) Right lateral view.

Since a large part of this thesis is devoted to the Crouzon mouse model, the mouse skull is shown for comparison in Figure 2.3.

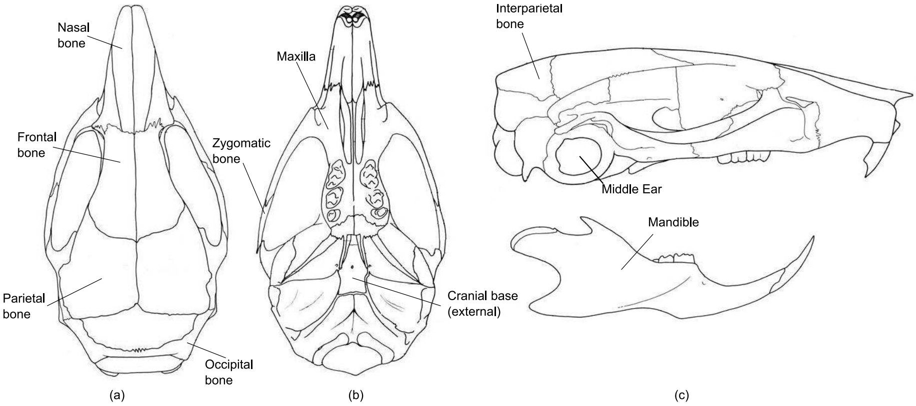

Figure 2.3: Schematic drawing of an adult mouse skull. (a) Top view, (b) Basal view, (c) Right lateral view. From [38]

2.2 Craniofacial Anomalies

As mentioned previously, the skull growth can be disturbed by several factors, leading to abnormal brain growth, dysmorphology, and in many cases an asymmetric head. Conditions associated with disturbed craniofacial development are referred to as craniofacial anomalies. The most common categories include:

- *Cleft lip and/or palate.* A congenital[1] condition characterised by an opening of the lip (cleft lip) or the palate (cleft palate).
- *Craniosynostosis.* A congenital condition where the growth zones close prematurely, leading to abnormalities in the growth of the brain and skull. Both syndromic (fusion of one or more sutures with additional physical deviations, e.g. Crouzon syndrome) and non-syndromic (fusion of one or more sutures only) craniosynostoses exist.
- *Deformational (Positional) Plagiocephaly.* Repeated pressure to the same area of the head leads to asymmetric head shape.
- *Hemifacial Microsomia.* Underdeveloped (smaller) tissues on one side of the face.

Three different craniofacial anomalies are studied in this thesis. These include *Crouzon syndrome* (in a mouse model) [43] (Chapter 7-9 and 11), *unicoronal synostosis plagiocephaly* (UCS) (Chapter 11), and *deformational plagiocephaly*

---

[1] A medical condition present at birth

(DP) (Chapter 10). The first two craniofacial anomalies involve craniosynostosis, i.e. one or more of the cranial sutures fuse too early, leading to disturbed brain and skull growth. In Crouzon syndrome, fusion usually occurs in several of the cranial sutures, while for UCS, only one of the coronal sutures (See Figure 2.1) fuses. DP, which is the least severe condition of the three, is a result of the infant repeatedly being positioned on the same side of the head, e.g. during sleep. DP, as well as UCS results in a plagiocephalic head, i.e. flattening on one side of the skull. However, in DP, the sutures remain normal. In accordance with this, UCS is an example of a craniofacial malformation while DP is an example of a craniofacial deformation.

The incidence of Crouzon syndrome is one in 20,000 births [37] and the incidence of UCS is one in 9,000 to one in 14,000 depending on the study [36]. Before 1992, the incidence of DP was estimated to be one in 300 [151]. However, while the incidence of sudden infant death syndrome (SIDS) has reduced remarkably during the past decade due to the "back to sleep" campaign [110], the incidence of DP is now estimated to occur in one in twelve infants [14].

All three conditions lead to abnormal and asymmetric head shapes. Figure 2.4 shows children with the three different types of craniofacial anomalies.


(a) (b) (c)

Figure 2.4: Children with (a) Crouzon syndrome (by courtesy of Sven Kreiborg), (b) Unicoronal synostosis (from [2]), (c) Deformational Plagiocephaly (from [1]).

The three types of craniofacial anomalies are treated differently. Crouzon syndrome and UCS are treated by one or more surgical procedures, involving acquisition of CT scans for surgery planning and evaluation. DP is normally treated by altering the child´s sleeping position. However, after the infant has reached six months of age, the skull is not as soft and for severe DP cases, an orthotic helmet is applied at some treatment centers. A CT scan of infants with DP is usually not acquired, unless the clinician suspects the infant to have craniosynostosis. In the DP study presented in this thesis (Chapter 10), a 3D surface imaging system is used for a detailed assessment of the shape of the head.

CHAPTER 3

Overview of Methods

This chapter provides a brief overview of the methods applied in this thesis. Where appropriate, references to in-depth material and alternative approaches are given.

3.1 Image Registration

An important problem in the field of image analysis is that of achieving voxel-wise correspondence between images (volumes). This problem occurs in various situations within medical image analysis, and *image registration* is often the key to the solution. The most common types of image registration applications are listed below.

- Registration of images acquired of the same individual at different time points by the same imaging modality. This can be applied for monitoring changes in a particular organ or a body part for e.g. screening or treatment evaluation.
- Registration of images acquired of the same individual by different modalities, which is useful when combining or fusing information from different modalities.

- Registration of images acquired of different individuals by the same modality. This is most often used for population studies or atlas building, i.e. creation of an average image from a population, or for segmentation.

In these situations, the subsequent analysis is either based on the corresponding voxel intensities (known as voxel-based morphometry), or the deformation fields required to map one image to another are analysed (known as deformation- or tensor-based morphometry).

In this short introduction the three main parts of an image registration algorithm will be highlighted. Affine and non-rigid (also referred to as non-linear or curved) transformations will be discussed but the overview will be limited to algorithms based on image information only, i.e. independent of landmark or segmentation information.

Formally, given two 3D images (volumes), *target* (or reference), A and a source (template), B:

DEFINITION 3.1 The goal of an image registration algorithm is to find a mapping, $\mathbf{T} : \mathbb{R}^3 \rightarrow \mathbb{R}^3$ such that the image similarity $\mathcal{D}(A, B(T))$ is maximised.

Here, $B(T)$ refers to the image B after transforming by $\mathbf{T}$ (see Section 3.1.1.2 for details). Three entities are required to solve the stated problem.

- A transformation model, $\mathbf{T}$.
- A measure of image similarity, $\mathcal{D}$.
- An optimisation method to maximise the similarity measure with respect to the parameters of the transformation model.

The three entities will be touched upon in the following sections. For the interested reader, extensive surveys on image registration have been made by Maintz and Viergever [140] and by Zitova and Flusser [240].

3.1.1 Transformation Models

Here, linear and non-rigid transformation models will be considered. A generalised description of a linear transformation is achieved by an affine transformation, which includes translation, rotation, scaling and shearing. Mathematically, it is denoted (in 3D)

$$\mathbf{T}_{affine}(x, y, z) = \mathbf{Ax} + \mathbf{t}, \tag{3.1}$$

where $\mathbf{x}$ is a vector holding the point (voxel) coordinates (x, y, z), $\mathbf{t}$ is a vector holding the translation parameters, (t_x, t_y, t_z) and $\mathbf{A}$ is a 3×3 matrix holding the remaining parameters (see e.g. [199] for details).

The non-linear models are more complicated, but necessary to adequately solve many medical registration problems. Affine transformations are not sufficient when matching local differences from image to image, such as those encountered when dealing with intersubject registration. Some of these transformation models are derived from physical or mechanical systems, such as demons [216] elastic [10] and fluid [29] registration.

Another way of describing non-linear transformations is provided by splines. Thin-plate splines [145] are popular for surface- or landmark-based registration [17] but have also been used for voxel-based image registration [146]. One drawback of this approach is that the thin-plate splines radial basis functions have infinite support, i.e. it becomes hard to match local deformations in detail. On the other hand, free-form deformations (FFDs) based on cubic B-splines [126] have local support. The use of FFDs for non-rigid image registration was presented by Rueckert et al. [185]. Due to its local support, robustness, and simple terminology the B-spline approach is used for all image registrations in this thesis.

The FFD is defined by an $p_x \times p_y \times p_z$ mesh of control points $\mathbf{c}$ with spacing $(\delta_x, \delta_y, \delta_z)$. The underlying image is then deformed by manipulating the mesh of control points. The FFD model can be written as the tensor product of the one-dimensional (1D) cubic B-splines:

$$\mathbf{T}_{local}(x, y, z) = \sum_{l=0}^{3} \sum_{m=0}^{3} \sum_{n=0}^{3} B_l(u) B_m(v) B_n(w) \mathbf{c}_{i+l, j+m, k+n} \tag{3.2}$$

where $i = \lfloor x/p_x \rfloor - 1, j = \lfloor y/p_y \rfloor - 1, k = \lfloor z/p_z \rfloor - 1, u = x/p_x - \lfloor x/p_x \rfloor$, $v = y/p_y - \lfloor y/p_y \rfloor$ and $w = z/p_z - \lfloor z/p_z \rfloor$. B_0 through B_3 represent the basis functions of the B-spline:

$$\begin{aligned}
B_0(u) &= (1-u)^3/6 \\
B_1(u) &= (3u^3 - 6u^2 + 4)/6 \\
B_2(u) &= (-3u^3 + 3u^2 + 3u + 1)/6 \\
B_3(u) &= u^3/6.
\end{aligned}$$

An example of a B-spline-based non-rigid image registration is given in Figure 3.1.

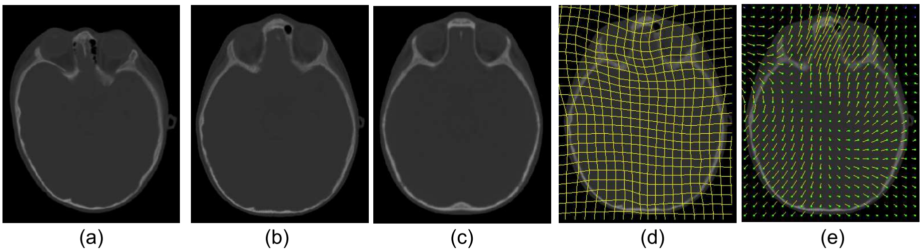

Figure 3.1: Example of a B-spline-based non-rigid registration. A 3D CT image of a child with UCS (source) is registered to a 3D CT image of a normal child (target). Single-slice axial views are presented. (a) Source image, (b) source image registered to target image, (c) target image. (d) Resulting deformation grid and (e) corresponding deformation vectors at control point positions.

3.1.1.1 Regularisation

The cost function of an image registration algorithm typically consists of the similarity measure. However, often a regularisation term is added to ensure proper interpretation of the deformation fields. As D´Arcy Thompson puts it,

> "We shall strictly limit ourselves to cases where the transformation necessary to effect a comparison shall be of a simple kind, and where the transformed, as well as the original coordinates shall constitute an harmonious and more or less symmetrical system." [219] (p. 1034).

Properties such as smoothness and volume preservation often act as regularisation terms. Examples of regularisation are the bending energy [15] to ensure smooth deformations, the Laplacian energy term [3, 214] and a term to preserve volume and prevent folding [184].

With respect to the B-spline-based approach, the properties of cubic B-splines already give considerable smoothing. A fast way to further regularise the deformation is to apply multi-level B-splines [188]; i.e. given control point resolutions $\Phi^1 \ldots \Phi^H$, at levels $1, \ldots, H$, the final local transformation is the sum of the transformations at each level,

$$T_{local} = \sum_{h=1}^{H} T_{local}^{h}$$

Each level is optimised separately after precomputing the previous spline at T_{local}^{h-1}. In the same paper, a framework to fix a fraction of the control points was introduced [188]. Keeping e.g. background control points (outside of the spline local support neighbourhood of the object boundaries) fixed, further adds to the regularisation. In this thesis, no penalty terms were added, the properties of the B-splines, the multi-level property and fixing control points were found sufficient to acquire convincing registrations and deformation fields.

3.1.1.2 Transforming images

While voxel coordinates are discrete, the range of a typical transformation model is continuous. This means that intensities cannot be transformed directly from source to target. The standard solution to this problem is to sample values from the source into the voxel locations of the target. The resampling is carried out by interpolation schemes, taking into account the voxels closest to the transformed point (e.g. nearest neighbour, bilinear, spline or sinc interpolation). This means, unless the inverse of the transformation model is used, that the opposite transformation is obtained, i.e. deforming the source image into the target image gives the deformation field from the coordinate system of the target to the coordinate system of the source. Hence, the notation $B(T(x_i))$, refers to the interpolated source intensity at position $T(x_i)$, where x_i is the original voxel position in image A.

3.1.2 Similarity Measures

A voxel similarity measure indicates how well the source image matches the target image. The choice of similarity measure is highly dependent on the relationship between the two images to be registered. A few types will be mentioned here.

When registering images acquired by the same imaging modality, a linear or an identity relationship can be assumed. The simplest similarity measure in this context is the difference in voxel-intensities, or sum of squared differences (SSD) [86].

$$\mathcal{D}_{SSD} = \frac{1}{M} \sum_{i} \left(A(\mathbf{x}_i) - B(T(\mathbf{x}_i)) \right)^2 , \tag{3.3}$$

where A is the target image and B is the source, x_i is the voxel position (x, y, z) and M is the total number of voxels. T denotes the transformation used to match the source to the target. A minimisation of the SSD expression leads to the best matching of the two images. Figure 3.2 shows the squared difference images from Figure 3.1 before and after registration.

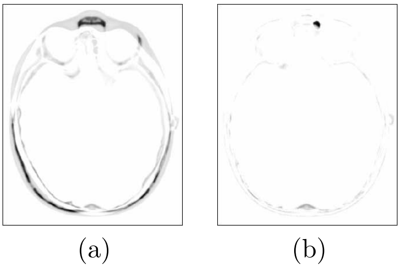
(a) (b)

Figure 3.2: Squared difference images (a) before and (b) after non-rigid registration of the images from Figure 3.1. The figures are inverted for better visualisation. Hence, white denotes no difference, black denotes largest difference.

Another popular measure is the correlation coefficient (equivalent to normalised cross correlation) [130].

$$\mathcal{D}_{CC} = \frac{\sum_i (A(\mathbf{x}_i) - \mu_A)(B(T(\mathbf{x}_i)) - \mu_B))}{\sqrt{(\sum_i (A(\mathbf{x}_i) - \mu_A)^2)\,(\sum_i (B(T(\mathbf{x}_i)) - \mu_B)^2)}} \tag{3.4}$$

When this expression is maximised, the two images are maximally correlated and hence, the best registration in this sense is obtained.

When the images to register are of different imaging modality or they highly differ in intensity (e.g. when a contrast agent is involved), information theoretic measures are useful. For image A with voxel intensities $a \in A$ the marginal entropy is defined as

$$H(A) = -\sum_{a \in A} p\{a\} log(p\{a\}), \tag{3.5}$$

where $p\{a\}$ is the marginal probability or the probability of finding intensity a in image A. The joint entropy is defined on the overlapping region between the two images A and B with voxel intensities $a \in A$ and $b \in B$,

$$H(A, B) = -\sum_{a \in A} \sum_{b \in B} p\{a, b\} log(p\{a, b\}), \tag{3.6}$$

[191], where $p\{a, b\}$ is the estimated joint probability or the probability of the occurrence of a particular pair of voxel intensities. Figure 3.3 shows the joint probability (2D histogram) before and after registration of the images in Figure 3.1.

The use of joint entropy as a similarity measure suffers from the fact that it is highly dependent on the overlap between the images favoring e.g. positions where

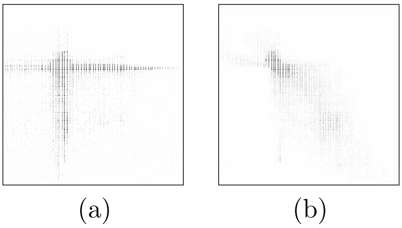
(a) (b)

Figure 3.3: Joint probabilities (a) before and (b) after non-rigid registration of the images from Figure 3.1. Note the larger spread of the signal before registration, indicating poor matching. After registration, the signal is more dense. The figures are inverted for better visualisation. Hence, black denotes high probability, while white denotes low probability.

large amount of background/noise is included in the overlap. This often leads to incorrect registrations. Mutual information (MI) [139, 233] partly overcomes this by incorporating the marginal entropy in the overlapping region of each of the images.

$$\mathcal{D}_{MI} = H(A) + H(B) - H(A, B). \tag{3.7}$$

This does not fully solve the overlapping problem and by dividing by the joint entropy, Studholme et al. introduced a normalised version of MI, normalised mutual information (NMI) [204]

$$\mathcal{D}_{NMI} = \frac{H(A) + H(B)}{H(A, B)}. \tag{3.8}$$

So far this is the most robust and widely used voxel similarity measure in the literature, especially for inter-modality registration. Nevertheless, some authors have made attempts to improve the NMI by incorporating spatial information, e.g. gradient information [177], feature maps [239] or higher-order features [167, 186]. An interesting survey of mutual information-based registration was made by Pluim et al. [178].

Other authors have replaced NMI by non-entropy-based similarity measures, which are easier to optimise. Such attempts include measures based on e.g. gradient information [72, 83, 84] and normal vectors [236].

3.1.3 Optimisation Methods

Finding the optimal non-rigid transformation to deform the source into the target is a difficult optimisation problem and several techniques have been evaluated. Gradient descent methods have been used with good results [185, 231] despite of slow convergence, in some cases. The Gauss-Newton algorithm utilises the second derivatives in an approximation of the Hessian. It gives a faster convergence and has been used by a few authors, [e.g. 7]. The properties of these two methods are combined in the Levenberg-Marquardt algorithm used for image registration in [e.g. 107, 215]. A few attempts have been made to speed up these algorithms, [e.g. 11, 67, 229]. For further discussion of numerical methods and acceleration techniques for image registration, refer to [147].

3.2 Computational Atlases

As mentioned before, image registration has many applications. One is the creation of a computational atlas. The term *atlas* has many meanings in the field of biomedical research. An experienced medical practitioner defines pathology by estimating the deviation from a typical normal subject in his/her mind. This reference frame could be referred to as a “mental atlas”. This type of atlas is obviously qualitative and highly subjective. Often, the anatomy of a single normal, healthy subject is referred to as an atlas and used as a reference frame when estimating deviations due to pathology. A less biased way of defining such a reference frame is to use the *average* of a set of normal subjects. This can for example be a set of points delineating an anatomical structure averaged over a set of subjects [e.g. 210]. Inclusion of more anatomical details results in shape- and intensity-based atlases constructed from a set of images in 2D, 3D [e.g. 18, 31, 34, 82, 106, 187] or even 4D [e.g. 174]. This type of atlas will be referred to as a *computational atlas*. The creation of such an atlas requires that a set of images from the group of interest are mapped into a common coordinate system. This is typically done by non-rigid image registration. The details of an atlas construction algorithm are listed in Section 7.2.3. Computational atlases have many applications. They can be used for automatic segmentation or landmarking or they can be used for population studies by analysing the deformation fields acquired to match subjects onto an atlas. This property will be discussed further in the following section.

3.3 Statistics on Deformation Fields

The result of an image registration algorithm is a deformed source image with voxel-wise correspondence to the target image. Additionally, a deformation field, required to establish correspondence, is obtained. The deformation field can be used to analyse the shape differences between anatomical structures in the two images. An example of such a deformation field is given in Figure 3.1.

One anatomical interpretation of the figure might be that the two scans differ mainly in the orbital and nasal region.

A structured way to analyse the deformation fields is to use prior knowledge from a set of registrations in combination with a statistical analysis. Among the pioneers in this relation were Grenander and Miller [80, 81] who used the term *computational anatomy*. They divided the process into three main steps (slightly rephrased here),

- Computation of deformation fields
- Computation of probability laws to determine anatomical variation
- Inference on population, clinical interpretations and classification

Here, the concept of computational anatomy will be divided into two categories, Statistical Deformation Models (SDMs) and Deformation Based Morphometry (DBM). SDMs are statistical models of the deformations created to extract and visualise the most important variations. The model can then be used to reconstruct the most important variations. In DBM, hypothesis testing is carried out, either directly on the deformation fields or on the principal scores obtained from SDMs. Basically, the two approaches differ in the way that SDMs provide statistical modes of variation, while DBM typically provides volumetric maps of p-values indicating significant deformations. The two approaches will be discussed in the following subsections.

3.3.1 Statistical Deformation Models

SDMs are closely related to statistical shape models. In both cases, the variability in anatomy of a population is of interest. This is typically modelled by principal components analysis (PCA). The key difference between the two approaches is that shape models require shapes represented by points which correspond over the set. This is highly dependent on manual labour, especially in 3D, although many authors have suggested approaches to overcome this [56, 70, 76, 226].

Statistical deformation models aim at capturing the anatomical variability by modelling of deformation fields. The deformation fields are typically acquired by a set of non-rigid registrations, each initiated in a common reference anatomy, ideally an atlas with normal, average anatomy. Apart from being fully automatic, this technique provides anatomical variability in the full volume, not only in a limited set of landmarks or predefined segmentations.

A couple of approaches exist for doing this. Bookstein´s principal warps are closely related to statistical deformation models. However, even though the modelling is carried out on the deformation fields, the thin-plate splines involved are landmark-dependent [15].

In some studies, the analysis is carried out directly on the deformation fields, e.g. in [106]. Other approaches, such as [187] and [41] model the parameters of the warps, which give a more compact representation of the deformation fields. A compact representation is also obtained in [60, 66], where deformation fields are established from sparse, manual delineations, and statistics are carried out in tangent space and extrapolated to the full volume.

In analogue with using shape models to constrain segmentation algorithms, [39], SDMs have been used in a few studies to constrain the search space of image registration algorithms [137, 235, 237].

In two chapters of this thesis (Chapters 8 and 9) the approach by Rueckert et al. [187] is applied. In this case, the parameters of the B-splines (the control points displacements, see (3.2)), which compactly represent the local deformation field between the atlas and the image of interest, are modelled. The control point displacements are then used as input to a PCA in order to model the deformations of the group of subjects defined in the domain of the atlas. Concatenating the 3D control point displacements for subject s into a row vector $\mathbf{C}_s = [c_1, ..., c_p]$, where $p = 3p_xp_yp_z$, gives the sth row of the $n \times p$ data matrix to analyse (n is the number of observations, $s = 1, \ldots, n$), the mean deformation is estimated by

$$\bar{\mathbf{C}} = \frac{1}{n}\sum_{s=1}^{n}\mathbf{C}_s$$

and the covariance matrix by

$$\frac{1}{n-1}\sum_{s=1}^{n}(\mathbf{C}_s - \bar{\mathbf{C}})(\mathbf{C}_s - \bar{\mathbf{C}})^T.$$

An eigenanalysis of the covariance matrix gives a matrix of eigenvectors $\mathbf{\Phi}$ and the corresponding eigenvalues λ. Now, a new spline parameter instance can be generated by the model,

$$\hat{\mathbf{C}} = \bar{\mathbf{C}} + \Phi\mathbf{b},$$

by varying the $\mathbf{b}$-parameter, typically within the limit of two standard deviations ($\pm 2\sqrt{\lambda}$). This spline parameter instance may now be applied to deform the atlas to represent an instance from the set of observations. In this thesis, experiment with alternative approaches to PCA have been carried out. PCA has the drawback of including each input point from the data matrix in the model providing results which may be hard to interpret. Independent component analysis

(ICA) was used in [91] to generate more localised modes of variation. Sparse PCA (SPCA) [242] shares these properties of ICA, while preserving much of the simplicity of PCA. This approach was taken in Chapter 9.

3.3.2 Deformation Based Morphometry

In order to infer whether the variations obtained by SDMs are significant, many authors have applied deformation based morphometry. The term was first introduced by Ashburner et al. [8]. This approach applies PCA to the parameters of deformation and analyses the new variables using multivariate statistics. This generates p-values indicating the significance of the findings. Similar approaches are applied in [45–47, 99]. Later, the expression tensor based morphometry has been used on equal terms with deformation based morphometry, indicating voxel-wise hypothesis testing on the deformation fields (further discussed in the following section).

In most of these studies, statistics are carried out on the determinant of the Jacobian, $\det(\mathbf{J})$, of the deformation field, which indicates whether a relative expansion ($\det(\mathbf{J})>1$) or contraction ($\det(\mathbf{J})<1$) of the volume has occurred [35, 73, 74, 132, 207, 213, 218, 221, 234]. Analysing the Jacobian is useful when exploring where volume changes occur. However, analysis of the full tensor gives more information on exactly how the anatomy is changing, as in the SDMs discussed above. Other approaches have argued that the information loss can be compensated for by analysing the strain matrix, $\mathbf{J}^T\mathbf{J}$ [133].

Another point of criticism of the Jacobian approach is that the information is too local and highly dependent on the type of transformation model [183, 206]. To overcome this, a regional approach has been suggested in [74] and smoothing of the Jacobian map in [206].

3.4 Large Scale Hypothesis Testing

An important issue of analysing multiple findings from image analysis algorithms is to test for the statistical significance of those findings. This is a non-trivial task since the findings from voxel to voxel are highly correlated. Hence, multiple comparisons need to be corrected for. This is e.g. highly important in deformation-based morphometry discussed in the previous section.

Many authors have studied this topic in relation to image analysis applications. The approaches include e.g. general linear models [8, 71], modelling by Gaussian random fields [21, 212] and permutation testing [150, 168].

In general, the problem is to simultaneously test several correlated hypotheses. This was addressed by Efron [62] with application to the analysis of DNA microarrays. In [51] this was adapted to the statistical analysis of deformation fields. In Chapter 11 of this thesis, this approach is used to estimate the significance of point-wise asymmetry. The remainder of this chapter discusses the details of this approach.

Efron's approach aims at improving the estimation of false discovery rate (fdr) [12] by replacing the theoretical null-hypothesis by an estimated empirical null-hypothesis.

The methodology requires that the statistical distribution (theoretical or empirical) of the input values is estimated. A p-value, p_i in each point i, is then estimated and the corresponding z-value is estimated,

$$z_i = \psi^{-1}(p_i), \qquad i = 1, \dots M \tag{3.9}$$

where ψ is the standard normal cumulative distribution function and M is the number of points under consideration (e.g. all vertices of a surface or all voxels in an image). The theoretical null-hypothesis states that $z_i \sim N(0,1)$.

Now, it can be assumed that the z-values fall into two classes, "uninteresting" and "interesting" and z_i has density $f_0(z)$ or $f_1(z)$ with prior probabilities p_0 and $p_1 = 1 - p_0$ depending on the class. Fitting a smooth curve to the z-histograms gives an estimate of the mixture density, f(z),

$$f(z) = p_0 f_0(z) + p_1 f_1(z). \tag{3.10}$$

Following Bayes theorem, the a posteriori probability that z_i falls into the uninteresting class is

$$P\{\text{Uninteresting}|z\} = \frac{p_0 f_0(z)}{f(z)} \tag{3.11}$$

Now, Efron defines local false discovery rate by

$$fdr(z) = \frac{f_0(z)}{f(z)} \tag{3.12}$$

providing an upper bound to $P\{\text{Uninteresting}|z\}$ (since p_0 is ignored). Instead of using the theoretical null-hypothesis for $f_0(z)$, Efron proposed to use the empirical null-hypothesis, obtained by estimating the mean and standard deviation from $f(z)$. Now, the input values can be classified as interesting or uninteresting, assigning a certain threshold to the fdr (Efron suggests that $fdr(z_i) \leq 0.10$ gives an interesting finding).

3.4.1 Example: Comparing Displacements

To give an example of the use of local false discovery rate, we compare pointwise deformations from the surface of a wild-type mouse atlas to 10 wild-type mice and 10 Crouzon mice (the data from Chapter 7-9 and 11). The analysis is based on the magnitude of the displacement vectors as in [51]. It is assumed that each component of the three-dimensional deformation vector follows a normal distribution. Hence, the squared magnitude will follow a χ^2 distribution with three degrees of freedom. The significance of the differences between groups may be estimated by an F-test, since the ratio of two χ^2 distributions follows an F-distribution. Now, the χ^2 distribution for each group is a sum of $\chi^2(3)$ distributions for each observation and the degrees of freedom is equal to the sum of degrees of freedom for the individual distributions. Given the squared magnitude of the deformation vector, D_i, the F-statistic becomes,

$$\frac{|\bar{D}_i^{\,G1}|/(2N_{G1})}{|\bar{D}_i^{\,G2}|/(2N_{G2})} \sim F(2N_{G1}, 2N_{G2}), i = 1 \ldots M$$

where

$$\bar{D}_i^{\,G1} = \frac{1}{N_{G1}} \sum_{j \in G1} D_i^j$$

is the mean squared magnitude in point i across subjects j in group $G1$ and N_{G1} is the number of observations (subjects) in group $G1$. By evaluating the F-statistic in each point of the surface, p-values may be obtained and inserted into (3.9) and (3.12). Figure 3.4 shows the z-value histogram of this experiment, labelling the components of the fdr.

For a discussion of this result, refer to Chapter 6.

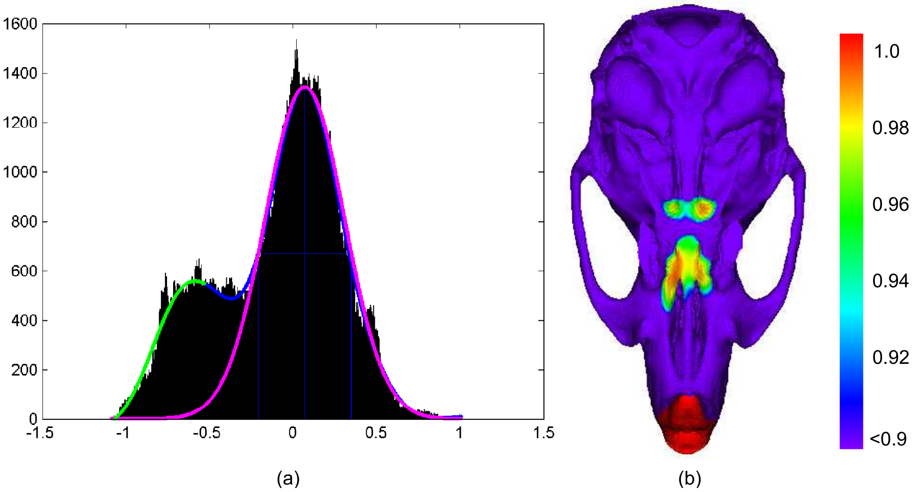

Figure 3.4: Example of local fdr-analysis. A group-wise comparison of deformation vector magnitudes in each point of a wild-type mouse atlas. (a) Example of a z-value histogram. The blue curve denotes the fitting spline, $f(z)$, the pink curve denotes the empirical null-hypothesis, $f_0(z)$ and the green curve denotes the observations with $fdr(z) \leq 0.10$. (b) 1-fdr displayed on the atlas surface. The positions where $1 - fdr > 0.9$ correspond to the bins under the green curve in (a).

Chapter 4

Images of Craniofacial Anomalies. From Manual to Automated Analysis

The aim of this chapter is to describe the developments in the field of craniofacial image analysis with respect to automation and detail of the analysis. The following review will focus on the topics of this thesis, namely morphometry and asymmetry.

4.1 Morphometry

Roentgencephalometry, first introduced by Broadbent in 1931 [19], is a widely used technique for investigating craniofacial malformations. The Broadbent technique refers to quantitative measurements based on a set of reference points. The reference points are set by annotating X-rays (cephalograms), most often acquired in lateral view and the measurements are used to assess craniofacial growth and development and to evaluate the effect of treatment. [e.g. 117]. A more advanced version of roentgencephalometry is a three-dimensional reconstruction from X-rays in three projections, [e.g. 20].

The reference points used for Roentgencephalometry are typically defined manually. Several authors, however, have attempted to automate the tedious process of manual landmarking (see reviews in [57, 131]). The cephalometric measurements (manual or automatic) are typically analysed by a statistical comparison of measurements for a group of affected subjects to a control group. This was e.g. done in [96] and [97], where several hundred landmarks were annotated in three projections and t-tests comparing distances and angles were carried out to study cleft lip and palate (CLP). A more complete analysis of reference points is done by finite element scaling analysis (FESA) [182] or Euclidean Distance Matrix Analysis (EDMA) taking into account all inter-landmark distances [129]. This approach was applied in [195] to study craniofacial growth in children with CLP. To further assess local shape changes, some authors have applied statistical shape modelling [58] (also referred to as geometrical morphometry in the literature) to the landmarks. This includes studies of children with CLP [53], studies of children with malocclusions [9, 87, 194] and analysis of mandibular growth [69].

Although roentgen cephalometry has its advantages due to low radiation doses, CT provides a complete representation of the anatomy and is preferred for diagnosis and surgery planning in many situations. In addition to this, 3D techniques include laser scans and photogrammetry, which provide 3D facial surface reconstructions. Within the field of anthropology and evolution, 3D landmarks are placed on dry skulls, digitised and analysed, typically using shape modelling or EDMA [e.g. 94, 111, 154]. Keeping the focus on craniofacial malformations, the maxillary arch of children with CLP was analysed in [53], the craniofacial morphology of mice with CLP was assessed in [88] using shape modelling and EDMA and a similar study for various mouse mutants was presented in [89]. Shape models of the mandible from MR images were created to investigate the effect of surgery in [25].

A few approaches have assessed 3D shape variation with dense point-correspondence (as opposed to the sparse landmark representations mentioned above). This includes the work of Hammond et al. which applied shape modelling to facial 3D photogrammetry data for the classification of different groups of children with congenital craniofacial malformations [90]. In [102] 3D growth models of facial surface data were constructed and in [79], shape models of soft-tissue surfaces from CLP children were created. A method for 3D surface registration of mandibles was developed in [5] and applied to growth modelling in [6, 98]. An atlas of the human ear from laser surface scans using level sets was created in [68] and different types of shape models of the human ear from similar scans were presented in [51, 170].

All of the above mentioned approaches are solely based on landmark- or surface-data. Very little attention has been paid to utilising the full volumetric information stored in CT images. Among the pioneers in non-rigid image registration were Christensen et al. and one of their first applications was the creation of a computational cranial atlas [31]. Later, non-rigid image registration was applied to create point-correspondence on the surface of mandibles [119]. Deformation fields in the maxilla and mandible for evaluating the effect of surgery were investigated in [26]. This thesis further adds to these types of applications by including the creation of a craniofacial computational mouse atlas [162] and the statistical modelling of deformation fields to analyse shape differences between Crouzon mice and wild-type mice [91, 160, 163].

4.2 Asymmetry

The simplest methods for determining craniofacial asymmetry are direct anthropometry of the head using a caliper [e.g. 113, 200], measurement systems using a head ring [27] or a thermoplastic strip molding the head shape [228].

Another way of measuring cranial asymmetry is from reference points on cephalograms. Methods for determining asymmetry by comparison of left and right side landmarks were developed early [28, 190, 211, 227, 230], some of which are still in use today [e.g. 108, 124, 224]. Similar methods have been adopted to 2D photographs, [e.g. 61, 78].

Van Valen, one of the pioneers with respect to measuring craniofacial asymmetry, discussed the terms directional and fluctuating asymmetry [227]. These terms were revisited by Bookstein [16] and Mardia et al. [141]. They defined asymmetry using Procrustes shape distance after aligning landmarks from original and reflected shapes. They defined the directional asymmetry as the squared mean Procrustes distance between two configurations (original/mirrored shape) while the fluctuating asymmetry resembled its standard deviation. Further, they developed elaborate statistical tests for their measure and evaluated its performance on several data sets, including craniofacial data. These methods have been used in a few other craniofacial studies, e.g. to study craniofacial asymmetry in schizophrenia patients with direct anthropometric measurements [95] and (with some extensions) to study the asymmetry of the jaw of cichlid fishes [112]. Lele and Richtsmeier defined asymmetry and tested for significance using EDMA [128]. Their approach was applied in [144] to study asymmetry in parents of children with orofacial clefting using direct anthropometric landmarks.

Measurements on 3D scans, generated by either 3D photogrammetry systems, laser scanners or CT, obviously give more possibilities. Laser scans were analysed in [176], manual measurements on CT scans were used to determine asymmetry in [22, 103]. Based on landmark data a 3D asymmetry vector indicating angle and size of facial asymmetry was applied in [64, 65]. Another landmark-based asymmetry measure was introduced and applied to 3D photogrammetry data in [85]. Facial asymmetry in infants with CLP was assessed using landmarks on 3D photogrammetry surfaces [100]. Several different methods for asymmetry assessment from 3D laser scans were discussed in [153], e.g. landmark-based approaches, volume measurements and closest point differences. The conclusion was that different applications required different methods of asymmetry assessment. Craniofacial morphology and asymmetry were studied in [118] comparing patients with dentofacial deformity.

All of the above approaches represent a sparse way of analysing craniofacial asymmetry except maybe the closest point difference approach discussed in [153]. A few 3D continuous approaches exist. 3D asymmetry was estimated in mandibles using spherical harmonics coefficients in [77]. Craniofacial asymmetry was defined as the deviation of a midsagittal surface from a midsagittal plane in [32]. This thesis further adds to these applications by two different approaches: Point-wise asymmetry in infants with deformational plagiocephaly was measured in [121] by comparing left and right distances of a deformed symmetric surface to midpoint. Moreover, volumetric asymmetry in Crouzon mice and UCS children was assessed in [164, 166] by comparing the displacement vectors on the left and right side resulting from an image registration to a symmetric volume.

4.3 Concluding Remarks

From the previous sections, it is evident that there is high interest in the analysis of craniofacial images. However, most of the methods rely on a qualitative assessment or a quantitative manual analysis using a sparse set of landmarks. Even though cephalometry is still valid due to the low dose of radiation, compared to CT, the tendency is clearly a shift towards 3D analysis. In this relation, going from a sparse set of reference points to utilising the full 3D volume or surface data in an automatic framework provides much greater detail and higher reproducibility. This may lead to more knowledge about different craniofacial anomalies, in addition to providing powerful tools for treatment planning and evaluation.

CHAPTER 5

Contributions

The main contribution of this thesis is to demonstrate the feasibility, accuracy and efficiency of applying non-rigid image registration to study craniofacial anomalies. In particular, the thesis has focused on the study of deformation fields resulting from non-rigid image registration. This involves atlas building, visual examination of deformation fields, statistical modelling, and the extraction of geometrical information, such as asymmetry. Furthermore, the statistical significance of findings from deformation fields, has been investigated. Non-rigid image registration based on B-splines [185, 188] has been the basis for most of the contributions, i.e. Chapters 7-9 and 11 while thin-plate spline surface registration has been used in Chapter 10. Figure 5.1 gives example results from the different papers presented.

Chapter 7 describes the creation of computational mouse atlases and provides interpretations of group differences from automatically obtained linear measurements and deformation fields. The contribution here is mainly clinical. Compared to other approaches investigating Crouzon syndrome this is by far the most automated and detailed study. Previous findings are confirmed and a new trait concerning an angulation in the cranial base of Crouzon mice is observed.

Chapters 8 and 9 are based on the theory of statistical deformation models (SDMs) [187]. Chapter 8 applies SDMs to the analysis of shape variability within and between groups. It confirms the findings from Chapter 7 and concludes that the shape of the Crouzon mouse skull varies more and is more asymmetric than the shape of the wild-type mouse skull. The main contribution of Chapter 9 is the use of sparse principal components analysis (SPCA) for the modelling of deformation fields. Due to the ability of SPCA to localise the largest variability in many modes of the model, it reveals more aspects of the between-group variation, including angulation in cranial base, nose bending and deformation in the middle ear and the back of the head. Further, it is concluded that SPCA outperforms both principal components analysis (PCA) and independent component analysis (ICA) with respect to discriminating between the groups of mice.

Chapters 10 and 11 introduce two different approaches to quantify bilateral asymmetry. In addition to presenting novel asymmetry measures, both of these chapters contribute to the understanding of the craniofacial malformations studied with respect to locating the most important areas of asymmetry. In Chapter 10, a thin-plate spline procedure is applied for registering a symmetric surface to each subject surface. The ratio of left/right distances to a midpoint in each point of the surface is then defined as the asymmetry. Furthermore, a statistical model of asymmetry in children with deformational plagiocephaly is created, revealing the first two modes of asymmetry variation to be located in the posterior and anterior head, respectively. Chapter 11 directly uses the deformation vectors from a B-spline-based image registration of a symmetric template volume to a patient volume, resulting in a voxel-wise measure of asymmetry. This is applied to studying asymmetry in the Crouzon mouse skull and in children with unicoronal synostosis. With respect to Crouzon syndrome, the most important findings are the asymmetry in the nose, zygoma and posterior skull region. For children with unicoronal synostosis, previous studies on the condition are confirmed since asymmetry is detected in the mid-face, posterior skull and anterior cranial fossa. However, the proposed approach provides higher spatial resolution than previous studies. The findings are verified by point-wise statistical hypothesis testing with correction for multiple comparisons.

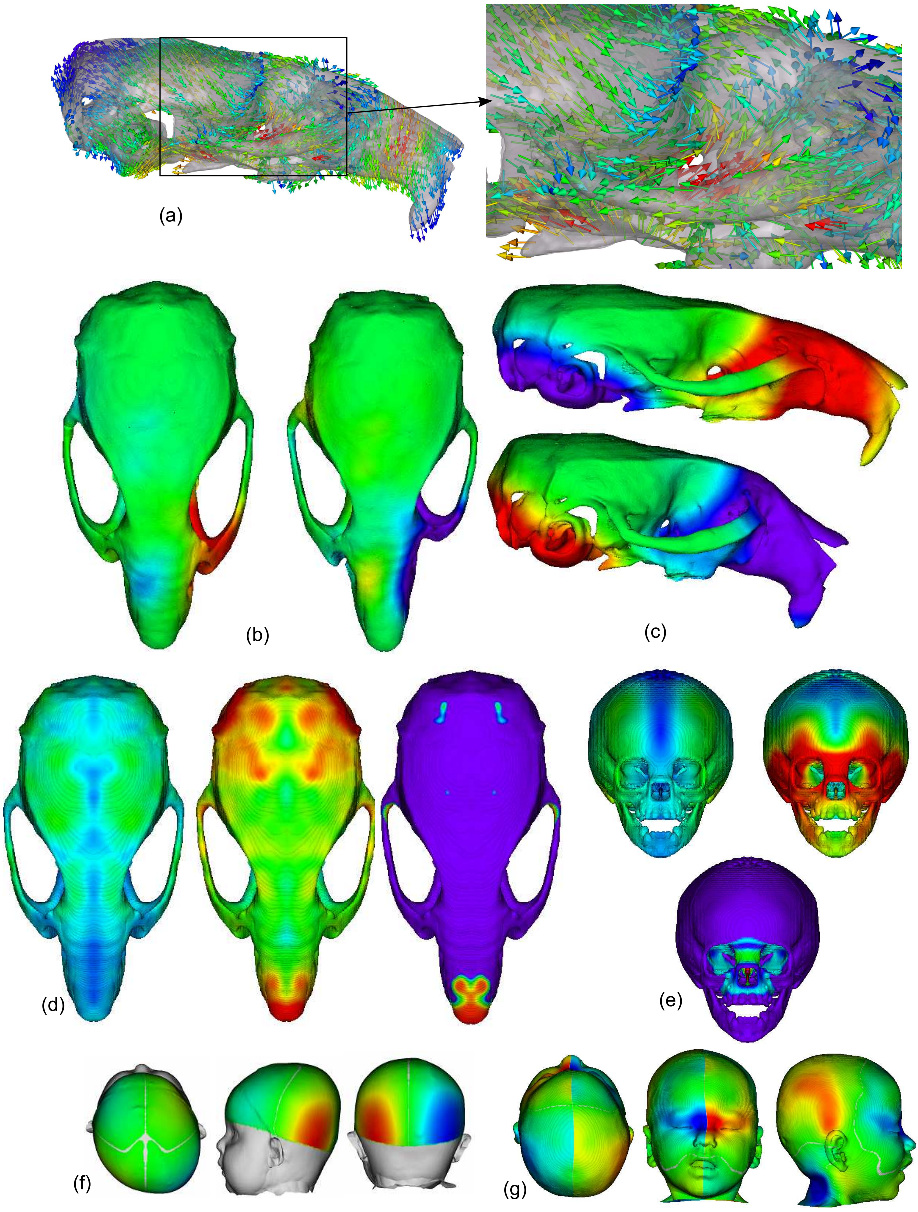

Figure 5.1: Example results from the thesis. (a) Visual inspection of deformation fields to explore differences between wild-type and Crouzon mice (Chapter 7). (b-c) Two modes of a sparse statistical deformation model for the two groups of mice (Chapter 9). (d) Mean cranial asymmetry from the group of normal and Crouzon mice, displayed on the symmetric skull along with the statistical significance of the group difference (Chapter 11). (e) Mean cranial asymmetry of a normal skull and a UCS skull along with the statistical significance of the group difference. (f) Point-wise asymmetry quantification in an infant with deformational plagiocephaly (Chapter 10). (g) Point-wise asymmetry quantification in a child with unicoronal synostosis (Chapter 11).

Chapter 6

Discussion and Conclusion

This thesis has focused on the use of non-rigid image registration for the study of craniofacial anomalies. This involves the concept of a computational atlas as well as the analysis of deformation fields to estimate anatomical variability and craniofacial asymmetry.

The analysis of such deformation fields is obviously highly dependent on the accuracy of the image registrations. The findings presented in this thesis are based on the belief that as long as the registrations are equally accurate as manual annotations by a human observer, the analyses are reliable. Given the registration accuracy with respect to two (or more) manual observers as in Chapter 7, findings larger than the error should be dependable. However, comparison to manually annotated landmarks is always limited to the sparse distribution of the landmarks. Even though a large number of landmarks is employed, they will never be directly comparable to a voxel-wise correspondence as obtained from the non-rigid registration. A way to get a higher detail in the error analysis is to check the point to surface distance, given that one or more segmented surfaces from the volume exist. This is done in Chapter 11. Even though such an approach does not measure point-correspondences, it gives a good spatial distribution of the registration errors and a lower bound for the point-to-point (correspondence) error. Although both validation approaches give convincing assessment of the registration errors, alternative validation methods exist. Validation of non-rigid image registration algorithms is, in fact, an active area of research and many different approaches have been suggested, [e.g. 44, 189].

Additionally, an interesting benchmarking study, including several validation criteria, is being carried out [33]. In conclusion, it may be argued that there is room for improvement regarding the validation aspects of this thesis.

One issue with non-rigid registration is its high computational cost. Even though computing power has increased, advanced imaging techniques acquire images of increasingly higher resolution demanding more computation time. Acceleration of non-rigid registration algorithms is of great interest to the image analysis community. Different approaches focusing on the optimisation techniques have been suggested [11, 107, 147]. Another group of methods includes model-based approaches, such as active appearance models [40]. They provide extremely fast registration, but the drawback is obviously the need for creation of a training set of corresponding landmarks, which, especially in 3D, is cumbersome. Recent approaches have aimed at unifying the two different groups of methods [42, 225, 237], i.e. applying image registration to the model building and register by the model parameters. These studies are very promising and given sufficient training data, this is clearly one way towards fast image registration.

The issue of the data set size takes us to the statistical models constructed in this thesis. Unfortunately the mouse data is limited to ten specimens from each group, which limits the variability of the statistical deformation models. However, since the two groups are strikingly different in shape, we are, despite the small data set, confident that the findings from the inter-group models in Chapters 8 and 9 are reliable. The within-group models in Chapter 8 would probably show more types of variation given more observations. The statistical asymmetry model from Chapter 10 includes 38 patients with deformational plagiocephaly (DP). This number should be sufficient to describe the asymmetry variation. However, more data exist and the plan is to extend this study to include more observations.

Chapters 10 and 11 introduce two approaches for a point-wise quantification of asymmetry of the head. The approach from Chapter 10 measures asymmetry in each point by the ratio of the corresponding left and right distances to a midpoint. This gives convincing results but the main drawback of this approach is that the use of ratios assigns higher asymmetry to points far away from the mid-point. Detected asymmetry in regions close to the center, such as the nose, is minimal. Applying the approach from Chapter 11 to the same data revealed asymmetry in regions not detected by the ratio-approach. In the case of DP the posterior and anterior asymmetry are most important and in that sense, the ratio-measure is still valid. However, for the general application, the measure from Chapter 11 should be used. The asymmetry-measures are being integrated for clinical use at St. Louis Children's Hospital for the treatment planning and evaluation of infants with DP.

Multiple hypothesis testing is of great interest in modern image analysis. Currently, the largest field herein is probably brain image analysis, including fMRI analysis [e.g. 50, 71, 179, 193] and deformation based morphometry [e.g. 35, 74, 207, 234]. However, in many other applications, voxel- or point-wise metrics are derived introducing the need for estimating the statistical significance. An ideal example is the analysis performed in Chapter 11, where the significance of point-wise asymmetry across groups is estimated using local false discovery rate. This approach was originally introduced in relation to DNA micro-arrays [62]. This application shares many properties with image data and the advantage of the method is that it is simple and gives easily interpretable results. In addition to the analysis in Chapter 11, an example of this approach was given in Chapter 3.4.1. The preliminary results in Figure 3.4 do to a great extent confirm the main findings of Chapter 7, that Crouzon mice differ from wild-type mice in the cranial base and nose. However, the conclusions about differences in the zygomatic bone are not confirmed. Perhaps this has to do with the limited size of the dataset or possibly, an analysis of the Jacobians may give more significant regions. Based on the experiments carried out in this thesis, it is concluded that the local fdr approach should be applicable to many other image analysis tasks.

Chapter 4 revealed that the use of non-rigid registration within the field of craniofacial image analysis is rare. One of the reasons is perhaps that, as opposed to e.g. the brain or the heart, the skull is rigid by nature. However, skull growth and differences in skull shape across individuals are highly non-rigid, motivating the approach. Another factor is the amount of existing data. To image the skull in 3D, typically CT images are required, which due to the radiation, does not allow for large control groups. On the other hand, the use of mouse models to analyse different craniofacial anomalies is steadily growing [223]. This allows for larger data sets, including a set of controls and highly detailed images, since the amount of radiation is not an issue when the animal has already been sacrificed.

6.1 Conclusion

This thesis has demonstrated the feasibility, accuracy and efficiency of applying non-rigid image registration to study craniofacial anomalies. Through the adaption of non-rigid registration to the particular field of craniofacial anomalies, a new framework for automated craniofacial image analysis has been created. The presented framework has to a great extent provided answers to the questions stated in Chapter 1. The severity of a particular craniofacial anomaly is provided by quantification of the abnormality, using e.g. the statistical deformation models or one of the asymmetry approaches, convincingly demonstrated on three different applications. The same may be stated about the second question about treatment progress. The DP data includes infants imaged before and after helmet treatment and the asymmetry measure is of great assistance in evaluating the progress. The third question about typical features of a population has been answered with respect to the shape of a Crouzon skull and the typical differences of a Crouzon and a wild-type mouse skull. Moreover, it has been involved in the statistical model of DP asymmetry.

In conclusion, this thesis has contributed through scientific results regarding craniofacial anomalies. In addition, it has provided tools of high relevance with respect to treatment planning and evaluation of children with craniofacial anomalies.

Part II

Contributions

Chapter 7

Computational Mouse Atlases and their Application to Automatic Assessment of Craniofacial Dysmorphology caused by the Crouzon Mutation Fgfr2^{C342Y}

Hildur Ólafsdóttir, Tron A. Darvann, Nuno V. Hermann, Estanislao Oubel, Bjarne K. Ersbøll, Alejandro F. Frangi, Per Larsen, Chad A. Perlyn, Gillian M. Morriss-Kay, Sven Kreiborg

Abstract

Crouzon syndrome is characterised by premature fusion of sutures and synchondroses. Recently the first mouse model of the syndrome was generated, having the mutation Cys342Tyr in Fgfr2c, equivalent to the most common human Crouzon/Pfeiffer syndrome mutation. In this study, a set of micro-computed tomography (CT) scans of the skulls of wild-type mice and Crouzon mice were analysed with respect to the dysmorphology

caused by Crouzon syndrome. A computational craniofacial atlas was built automatically from the set of wild-type mouse micro-CT volumes using (i) affine and (ii) non-rigid image registration. Subsequently, the atlas was deformed to match each subject from the two groups of mice. The accuracy of these registrations was measured by a comparison of manually placed landmarks from two different observers and automatically assessed landmarks. Both of the automatic approaches were within the inter-observer accuracy for normal specimens, and the non-rigid approach was within the inter-observer accuracy for the Crouzon specimens. Four linear measurements, skull length, height and width and interorbital distance, were carried out automatically using the two different approaches. Both automatic approaches assessed the skull length, width and height accurately for both groups of mice. The non-rigid approach measured the interorbital distance accurately for both groups while the affine approach failed to assess this parameter for both groups. Using the full capability of the non-rigid approach, local displacements obtained when registering the non-rigid wild-type atlas to a non-rigid Crouzon mouse atlas were determined on the surface of the wild-type atlas. This revealed a 0.6 mm bending in the nasal region and a 0.8 mm shortening of the zygoma, which are similar to characteristics previously reported in humans. The most striking finding of this analysis was an angulation of approximately 0.6 mm of the cranial base, which has not been reported in humans. Comparing the two different methodologies, it is concluded that the non-rigid approach is the best way to automatically assess linear skull parameters. Furthermore, the non-rigid approach is essential when it comes to analysing local, non-linear shape differences.

7.1 Introduction

Crouzon syndrome was first described nearly a century ago when calvarial deformities, facial anomalies, and abnormal protrusion of the eyeballs were reported in a mother and her son [43]. Later, the condition was characterised as a combination of a few traits: premature fusion of the cranial sutures (craniosynostosis), orbital deformity, maxillary hypoplasia, beaked nose, crowding of teeth, and high arched or cleft palate.

Shape deviations due to Crouzon syndrome in humans have been addressed in a few studies. The methods used for the analyses include roentgencephalometric measurements [117], finite element scaling analysis [182], Euclidean distance matrix analysis (EDMA) [129] smooth surface curvature measures [49], and basic cephalometry [23]. The major findings from these studies with respect to malformations in Crouzon patients are reported in Table 7.1.

Genetic alteration of the murine genome has become a standard tool in the field of craniofacial developmental biology. Numerous mouse models for craniofacial anomalies now exist, each with a unique phenotype [223]. The use of 3D micro-CT is becoming an increasingly popular technique for anatomic analyses of these models, with comparison to unaffected mice and other mutant mice being performed [171, 181, 198].

Heterozygous mutations in the gene encoding *fibroblast growth factor receptor type 2* (*FGFR2*) have been found responsible for Crouzon syndrome [180]. Recently a mouse model was created to study one of those mutations ($FGFR2^{Cys342Tyr}$) [63]. This model was analysed in a recent study using micro-CT head scans of a group of (unaffected) wild-type mice and a group of Crouzon mice. The study proved the mouse model applicable to reflect the craniofacial deviations occurring in humans with Crouzon syndrome confirming many of the morphological traits seen in previous studies on humans (see Table 7.1). This was achieved by a comparison of linear measurements obtained manually on the surfaces and by applying EDMA to a set of landmarks on the surfaces [173].

To further and automatically assess local deviations of mutant mice from normal, this study adopts the concept of a *computational atlas*. The term *atlas* has many meanings in the field of biomedical research. An experienced medical practitioner defines pathology by estimating the deviation from a typical normal subject in his/her mind. This reference frame could be referred to as a “mental atlas”. This type of atlas is obviously only qualitative and very subjective. Traditional anatomical atlases can be found in textbooks [e.g. 201] but they provide only a two-dimensional schematic representation of the anatomy and can be interpreted in different ways depending on the user. Often, the anatomy of a single normal, healthy subject is referred to as an atlas and used as a

Table 7.1: Overview of malformations due to Crouzon syndrome in humans (first six studies) and in mice (Perlyn 2006))

Region	Kreiborg et al. 1981	Richtsmeier 1987	Lele and Richtsmeier 1991	Kreiborg et al. 1993	Carinci et al. 1994	Cutting et al. 1995	Perlyn et al. 2006
Calvaria	Short Calvarial contour flattened in the lateral parietal regions						Short Wide High
Maxilla	Short and narrow Reduced Posterior maxillary height Maxilla retrognathic in relation to the anterior cranial base and backward inclined Short zygoma				Short		Short Posterior palate shifted relatively to cranial base
Nasal Region	Reduced height and depth of nasopharynx				Reduced size of cavities and height, reduced volume and height of rhinopharynx		Short nasal bones Short cavity
Sphenoid bone							Reduced Anterioposterior length
Cranial base	Short and narrow short clivus		Narrow floor				Short anteriorly

Table 7.1: continued. Overview of malformations due to Crouzon syndrome in humans (first six studies) and in mice (Perlyn 2006))

Region	Kreiborg et al. 1981	Richtsmeier 1987	Lele and Richtsmeier 1991	Kreiborg et al. 1993	Carinci et al. 1994	Cutting et al. 1995	Perlyn et al. 2006
Midface						Concave and wide Piriform aperture in center more recessed than the perifery of midface	
Sella turcica	High	Large pituitary fossa		Enlarged			
Forehead	Steep					Recessed above a frontal sinus bulge	
Occiput	Flattened	Small					
Anterior fontanelle	Protrusion						
Orbital region	high orbital opening Lateral and inferior orbital margins retruded Floor of orbit short, closer to nasal cavity than normal High interorbital distance					Shallow and concave orbits, tilted inferiorly Wide orbits	High Intercanthal distance

reference frame when estimating deviations due to pathology. A more correct way of defining such a reference frame is to use the average of a set of normal subjects. This can for example be a set of points delineating an anatomical structure averaged over a set of subjects [e.g. 210]. Inclusion of more anatomical details results in shape- and intensity-based atlases constructed from a set of images in 2D, 3D [e.g. 18, 31, 106] or even 4D [e.g. 174]. This type of atlas will be referred to as a *computational atlas* in the remainder of this paper.

Computational atlases have many applications. In most cases, they are deformable, meaning that it is possible to deform them into the corresponding anatomy of any subject within a population. These properties allow automatic linear or volumetric measurements and segmentation of different structures and organs [e.g. 48, 59, 138, 169, 238]. By creating probabilistic atlases, deviations from normal can be assessed in a statistical manner [e.g. 125, 143, 220].

The primary goal of the present study was to build automatically a computational atlas from the set of wild-type mice and apply it to study craniofacial malformations. Using recent techniques from image analysis, this paper presents the automatic construction of two types of craniofacial wild-type mouse atlases directly from the micro-CT data. The deformable nature of the atlases allows for automatic assessment of linear parameters of the skull and in this paper, four parameters are studied and analysed with respect to Crouzon dysmorphology. In order to assess the local malformations, the amount of deviations when deforming a wild-type mouse atlas into a Crouzon mouse atlas is determined and analysed.

The paper is organised as follows. The methods section covers data acquisition followed by an introduction to the image analysis methods and atlas construction. This section is concluded by stating how these factors are combined into a method allowing for automatic assessment of 3D landmarks and local shape deviations. The results section provides experimental results by a qualitative and a quantitative validation of the automatic assessments and an analysis of the global and local deviation of Crouzon mice from wild-type mice.

7.2 Materials and Methods

7.2.1 Data Material

Micro-CT scans of a control group of ten wild-type mice and ten Crouzon ($Fgfr2^{\mathrm{C342Y}/+}$) mice were studied.

The production of the $Fgfr2^{C342Y/+}$ and $Fgfr2^{C342Y/C342Y}$ mutant mouse (Crouzon mouse) was carried out as described by [63]. All procedures were in agreement with the United Kingdom Animals (Scientific Procedures) Act, guidelines of the Home Office, and regulations of the University of Oxford. Mutant mice of breeding age were determined by phenotype. Female $Fgfr2^{C342Y/+}$ mice were bred with males heterozygous for the same mutation. Since the $Fgfr2^{C342Y/C342Y}$ mice have too severe symptoms to survive the first post-natal day, the heterozygotes ($Fgfr2^{C342Y/+}$) were used as phenotypes for the study of Crouzon syndrome. Figure 7.1(a) shows two of the mice used in this study.

For micro-CT scanning, ten wild-type and ten $Fgfr2^{\mathrm{C342Y/+}}$ specimens at six weeks of age (42 days) were killed via CO_2 asphyxiation and whole mount skeletal preparations were made. They were sealed in conical tubes and shipped to the micro-CT imaging facility at the University of Utah, USA. Three-dimensional (3D) volumes of the skull of size 720×480×480 voxels were obtained at approximately 46μm × 46μm × 46μm resolution per voxel using a General Electric Medical Systems EVS-RS9 micro-CT scanner. Prior to processing the images, the neck part was removed from all 20 images since the mice were decapitated at different positions prior to scanning. The hyoid bone was also removed due to its random position and scanning artifacts. Additionally, due to different jaw positions and the fact that the deviation in mandible shape is a secondary effect of the syndrome, the mandible was also masked out for all 20 specimens. Figure 7.1(b,c) gives an example of the imaging data appearance, after extracting surfaces from the micro-CT images.

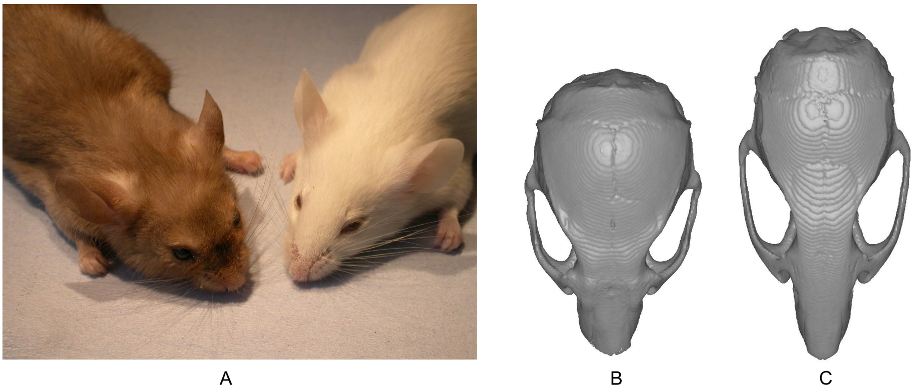

Figure 7.1: (A) Photograph of a Crouzon mouse (left) and a wild-type mouse (right). Skulls extracted from micro-CT images of a Crouzon mouse (B), wild-type mouse (C).

7.2.2 Image Registration

In order to build a computational atlas from the micro-CT images, the corresponding regions across subjects must be averaged. However, the original images are not defined in a common coordinate system so the different regions do not correspond. Therefore, image registration is needed. The goal of image registration is to warp one image, the *source*, into the coordinate system of another image, the *target*, using an optimal transformation $\mathbf{T}$. A basic image registration algorithm requires the following:

- A transformation model, $\mathbf{T}$.
- A measure of image similarity.
- An optimisation method to optimise the similarity measure with respect to the transformation parameters.

In this study, two different transformation types are used, an affine transformation and non-rigid deformations based on B-splines [185, 188]. The first captures *global, linear* differences between the images while the latter covers *local, non-linear* differences. In both cases, normalised mutual information [204] (NMI) is used as a similarity measure and gradient descent optimisation is applied. These terms will be covered in the following.

7.2.2.1 Affine Registration

Affine registration applies an affine transformation to map the source image into the target. Affine transformation is a linear transformation, defined by

$$\mathbf{T}_{affine}(x, y, z) = \mathbf{Ax} + \mathbf{t}, \tag{7.1}$$

where, in 3D, $\mathbf{x}$ is a vector holding the 3D point coordinates (x,y,z), t is a vector holding the three translation parameters and A is a 3×3 matrix of parameters, including rotation, scaling and shearing [199]. In this study, the affine transformation is restricted to 9 transformation parameters. These represent translation and rotation in addition to anisotropic scaling. An anisotropic scaling model was chosen, since the largest differences between the two groups of mice are length, width and height of the skull. Due to the small number of parameters being optimised, the registration is fast but the drawback is that only global differences between the images are taken into account while local differences are ignored.

7.2.2.2 Nonrigid Registration based on B-splines

To obtain more accurate registration focusing on local differences, non-linear transformations are required. A widely used method for this purpose is the non-rigid registration algorithm using B-spline-based free-form deformations (FFDs) [185]. In this case, a composition of a global and a local transformation,

$$\mathbf{T}(x, y, z) = \mathbf{T}_{global}(x, y, z) + \mathbf{T}_{local}(x, y, z), \tag{7.2}$$

is applied. The global model has already been described by the affine transformation. In 3D, the local transformation model, the FFD is defined by an $n_x \times n_y \times n_z$ mesh of control points $\mathbf{\Phi}$ with spacing $(\delta_x, \delta_y, \delta_z)$. The underlying image is then deformed by manipulating the mesh of control points. The FFD model can be written as the tensor product of the one-dimensional (1D) cubic B-splines:

$$\mathbf{T}_{local}(x, y, z) = \sum_{l=0}^{3} \sum_{m=0}^{3} \sum_{n=0}^{3} B_l(u) B_m(v) B_n(w) \boldsymbol{\phi}_{i+l, j+m, k+n} \tag{7.3}$$

where $i = \lfloor x/n_x \rfloor - 1, j = \lfloor y/n_y \rfloor - 1, k = \lfloor z/n_z \rfloor - 1, u = x/n_x - \lfloor x/n_x \rfloor$, $v = y/n_y - \lfloor y/n_y \rfloor$ and $w = z/n_z - \lfloor z/n_z \rfloor$. B_0 through B_3 represent the basis functions of the B-spline:

$$\begin{aligned} B_0(u) &= (1-u)^3/6 \\ B_1(u) &= (3u^3 - 6u^2 + 4)/6 \\ B_2(u) &= (-3u^3 + 3u^2 + 3u + 1)/6 \\ B_3(u) &= u^3/6. \end{aligned}$$

The transformation creates a dense deformation vector field which can be assessed at any point in the image.

7.2.2.3 Normalised Mutual Information as a Similarity Measure

In order to bring images into correspondence by image registration, the degree of similarity between the two images needs to be defined. The NMI is based on entropy measures in the two images. The marginal entropy in an image relates to the information content, or more intuitively it measures the uncertainty of guessing a voxel intensity. In image A with voxel intensities $a \in A$ the marginal entropy is defined as

$$H(A) = -\sum_{a \in A} p\{a\} log(p\{a\}) \quad , \tag{7.4}$$

where $p\{a\}$ is the marginal probability. The joint entropy is defined on the overlapping region between the two images A and B with voxel intensities $a \in A$ and $b \in b$,

$$H(A, B) = -\sum_{a \in A} \sum_{b \in B} p\{a, b\} log(p\{a, b\}) \quad , \tag{7.5}$$

where $p\{a, b\}$ is the joint probability. This corresponds to the information content of the combined scene or the probability of guessing a pair of voxel intensities. Mutual information describes the difference between the sum of the marginal entropies and the joint entropy and by dividing by the joint entropy, NMI is defined as

$$NMI(A, B) = \frac{H(A) + H(B)}{H(A, B)} \quad . \tag{7.6}$$

The strength of entropy measures, such as NMI, is their ability to cope with two different modalities [e.g. 205, 233] but they have been widely used with good results in intramodality applications as well [e.g. 175, 187, 192].

7.2.3 Atlas Construction

Two types of computational, deformable atlases were constructed from the set of wild-type mice in an iterative manner using (i) affine registration only, (ii) non-rigid registration (a composition of an affine registration and B-spline-based non-rigid registration). From this point on the atlases will be referred to as the *affine atlas* and the *non-rigid atlas*. Additionally, a non-rigid Crouzon atlas was built for average shape comparison purposes. All three atlases were built according to the procedure listed in Algorithm 7.1.

Algorithm 7.1 Atlas construction

```
1: atlas = a selected reference mouse from the group (wild-type or Crouzon)
2: repeat
3:    Register all mice from the given group to atlas
4:    atlas = Intensity average of all registered mice
5: until atlas stops changing
6: Register atlas to all mice from the given group
7: Transform atlas by $\bar{\mathbf{T}}$ = the average transformation obtained in step 6
```

Lines 3 and 6 in the algorithm are carried out using either affine or non-rigid registration depending on the type of atlas being constructed. In line 5, the root-mean-square (rms) error between the voxel intensities of the current atlas and the previous atlas is calculated and an appropriate threshold value chosen to define the state where the atlas stops changing. Lines 6 and 7 from Algorithm 7.1 are intended to reduce the bias in shape towards the choice of reference subject as previously done with good results [82, 187]. The affine and the non-rigid atlas are shown in Figure 7.2 and the non-rigid Crouzon atlas is shown in Figure 7.3(a-c). Finally, Figure 7.3(d,e) shows the non-rigid wild-type atlas and the non-rigid Crouzon atlas as surfaces extracted from the volumes.

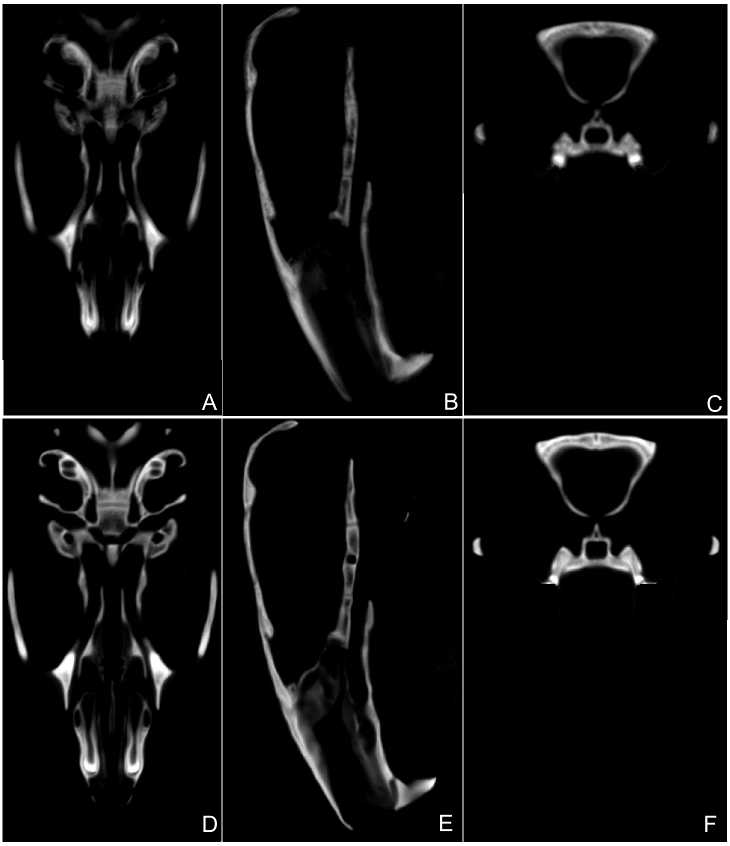

Figure 7.2: Comparison of affine (A-C) and non-rigid (D-F) wild-type mouse atlas. Three slices, an axial (A,D), sagittal (B,E) and coronal (C,F), through each atlas are shown.

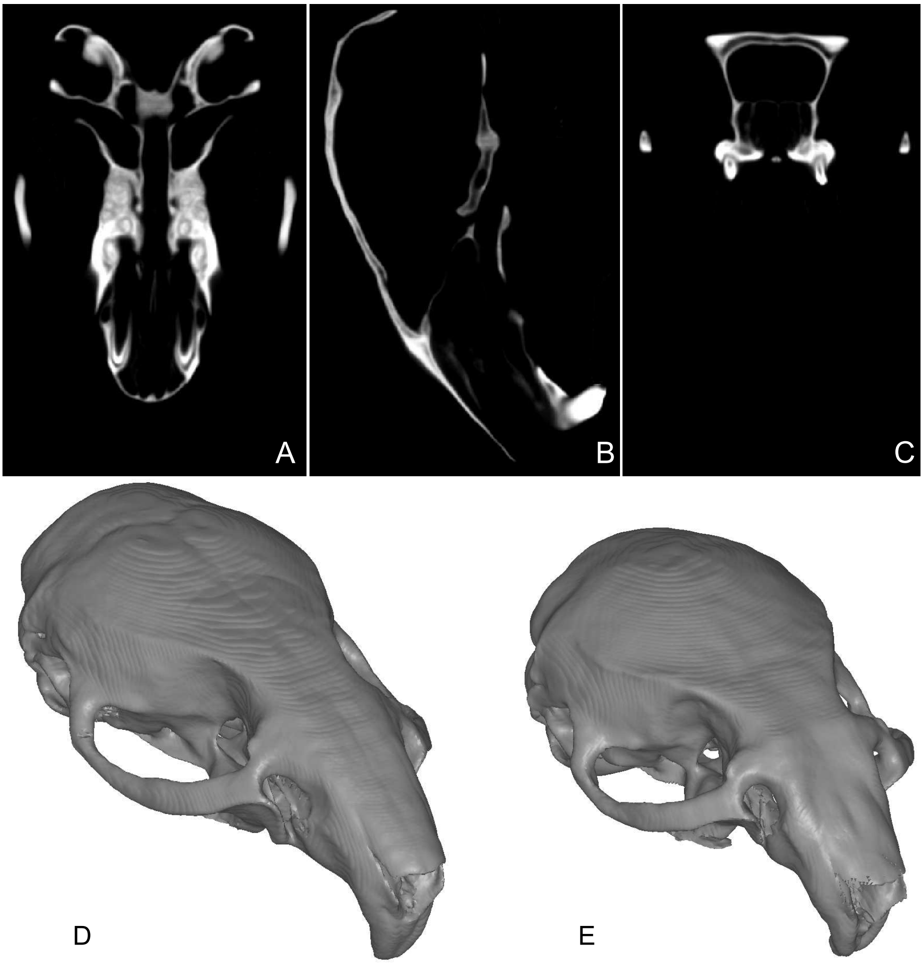

Figure 7.3: Nonrigid Crouzon atlas. Three volume slices, an axial (A), sagittal (B), and coronal (C), through the atlas are shown. A comparison of the non-rigid wild-type mouse atlas (D), and the non-rigid Crouzon atlas (E) shown in surface representation.

7.2.4 Assessment of Global Linear Parameters

Having constructed a computational atlas, it was then possible to carry out various measurements on it. Subsequently, corresponding measurements for any subject can be determined automatically. This is done by propagating the measurements on the atlas onto the subject according to the transformation, $\mathbf{T}$, required to register the subject image to the atlas image. For the affine atlas, affine transformations (T_{global}) are used to estimate the measurements and similarly for the non-rigid atlas, non-rigid deformations ($T_{global}+T_{local}$) are used.

To give an example of the capability of the automatic registrations, a few linear measurements of the skull are examined. In practice any linear measurement can be carried out on the atlas and measured automatically in any of the subjects. The parameters studied here are:

- L = Skull length
- W = Skull width
- H = Skull height
- IOD = Inter-orbital distance

The skull parameters were defined on the mouse skull following as closely as possible the definitions in humans. Figure 7.4 gives a graphical illustration of the parameters. Additionally, it shows 36 anatomical landmarks which are used for a quantitative validation of the registration accuracy. In this study, only 26 of the landmarks were used, since 10 landmarks were located on the mandible which has been removed from the images.

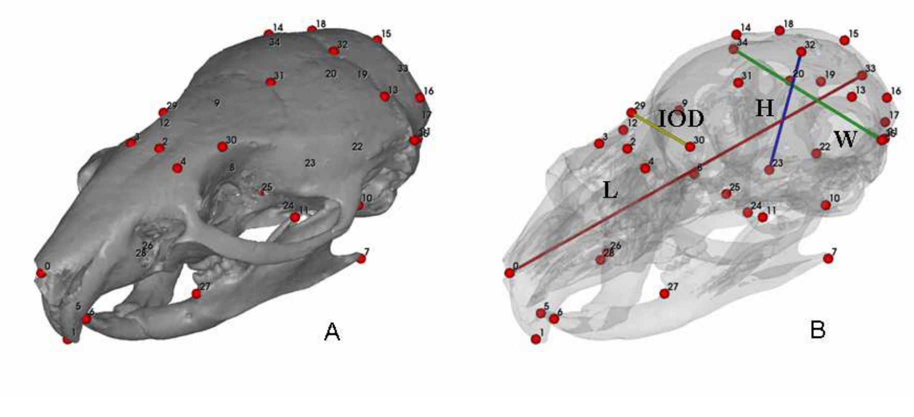

Figure 7.4: A: Landmarks shown on a mouse skull. B: Landmarks shown on a transparent mouse skull along with skull parameter definitions: L = skull length – distance between nasion (31) and most distant point on occipital bone (33), W = skull width – distance between the left (35) and right (34) most lateral points on the skull. H = skull height – distance between intersection of sutura coronalis and sutura sagittalis (32) and skull base point (23), IOD = intraorbital distance.

7.2.5 Assessment of Local Deviations

Utilising the full capability of the non-rigid approach, the deformation field from a given registration can be used to calculate the displacement in mm in each point on the target skull and in that way assess local differences between the source and the target.

7.3 Experimental Results

All 20 cases were registered (i) to the affine wild-type atlas by affine transformations and (ii) to the non-rigid wild-type atlas by non-rigid transformations. Each affine registration took 99 seconds on average while each non-rigid registration took 5230 seconds (87 minutes and 10 seconds) on average[1]. Secondly, the Crouzon atlas was registered to the wild-type atlas in order to assess the average local shape differences between the two groups. For the non-rigid registrations, control point spacings of 3, 1.5 and 0.75 mm were used. In all cases, four landmarks were used to roughly align the mice with respect to their mid-sagittal planes (MSPs) and standard horizontal planes prior to registration. This was done to intitialise the registration close to the region of capture for NMI.

The registration accuracy was estimated both qualitatively in terms of difference images and quantitatively in terms of anatomical landmarks (as displayed in Figure 7.4). The automatic assessment of the four linear parameters was evaluated directly with focus on the accuracy and with respect to global differences between the groups. Finally, the local differences obtained from the Crouzon atlas to wild-type atlas registration were quantified and visualised on the surface of the wild-type atlas.

7.3.1 Qualitative Validation of Registration Accuracy

A visual impression of the accuracy when registering the affine atlas to a Crouzon mouse is provided by difference images in Figure 7.5. Similar visualisation is shown for the non-rigid atlas in Figure 7.6.

---

[1] Using a Silicon Graphics Altix 350 with 16 Intel Itanium (1.5 GHz) true 64 bits processors with 32 GB of shared memory

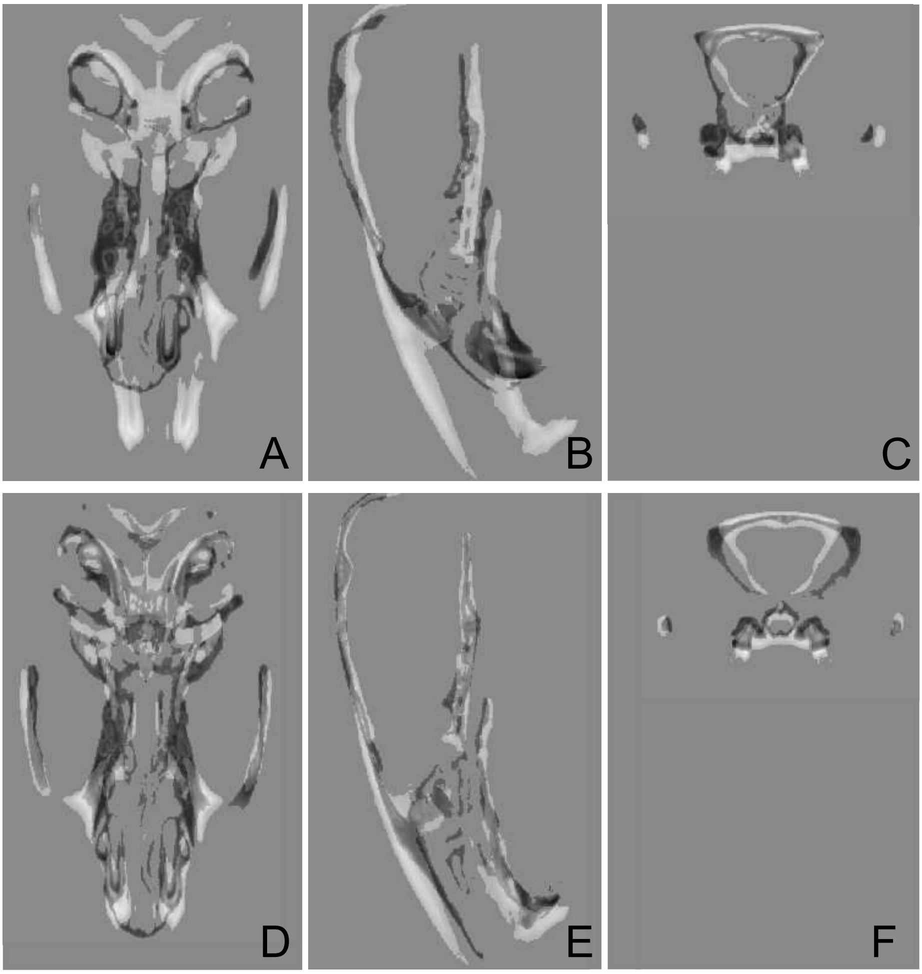

Figure 7.5: Affine registration of a Crouzon mouse to the affine atlas. Difference between the affine atlas and a Crouzon mouse is shown before (A-C) and after (D-F) registration in axial (A,D), sagittal (B,E) and coronal (C,F) slices.

7.3.2 Quantitative Validation of Registration Accuracy

The registration accuracy was further examined in a quantitative manner. For this purpose, 26 of the anatomical landmarks from Figure 7.4 were applied. Two independent observers annotated the set of images according to Figure 7.4. The average of the two annotations was used as gold-standard (GS). The GS landmarks on the atlas were then propagated automatically to all subjects using the

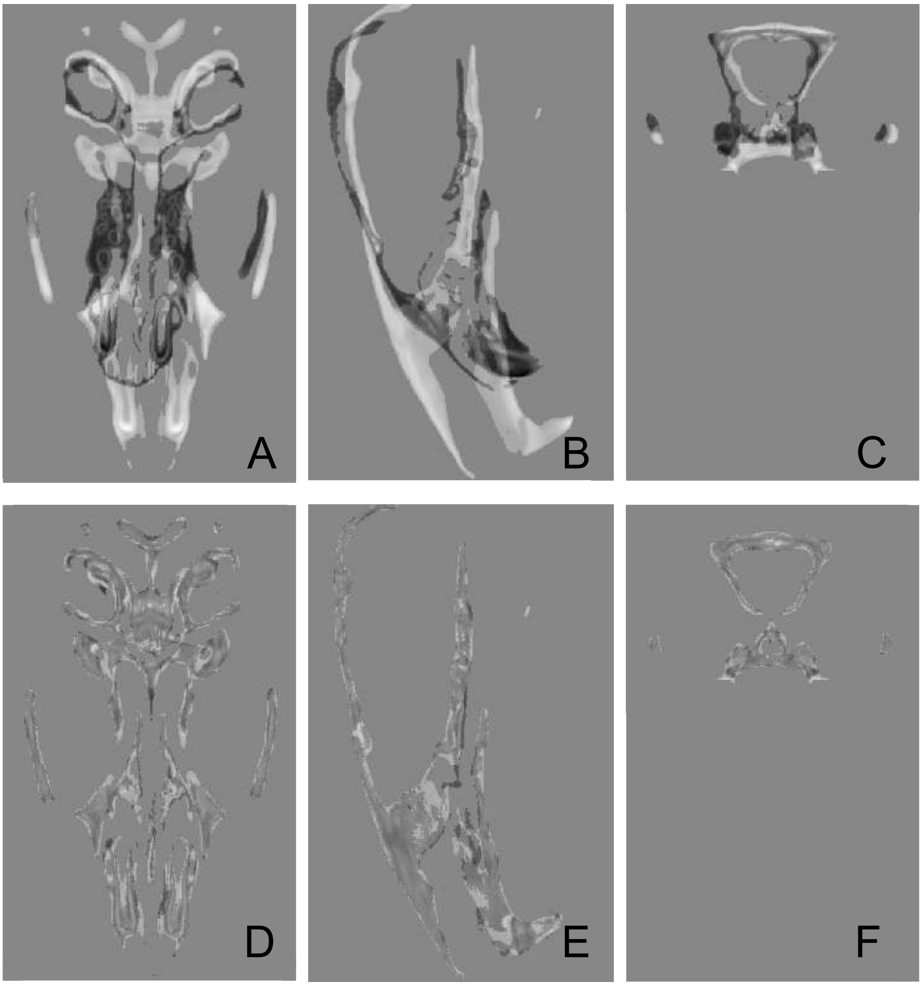

Figure 7.6: Nonrigid registration of a Crouzon mouse to the non-rigid atlas. Difference between the non-rigid atlas and a Crouzon mouse is shown before (A-C) and after (D-F) registration in axial (A,D), sagittal (B,E) and coronal (C,F) slices.

previously obtained optimal transformations for each approach. Subsequently, landmark errors were estimated. These are defined by the point-to-point error, i.e. the Euclidean distance from an automatically obtained landmark to the corresponding GS landmark. A statistical analysis of the landmark errors as described in the Appendix section was performed. The analysis revealed that both automatic approaches performed on equal terms with the observers for the wild-type mice and both had lower variance. For the Crouzon mice, landmark

#31 was defined as an outlier (see Section 7.4) and excluded from the analysis. The statistical tests concluded that the affine approach performed significantly worse than the observers while the non-rigid was as accurate as the observers. The landmark errors were scaled to provide a reasonable comparison as described in Appendix 7.A. The scaled errors are shown in Figure 7.7 using box and whisker plots[2].

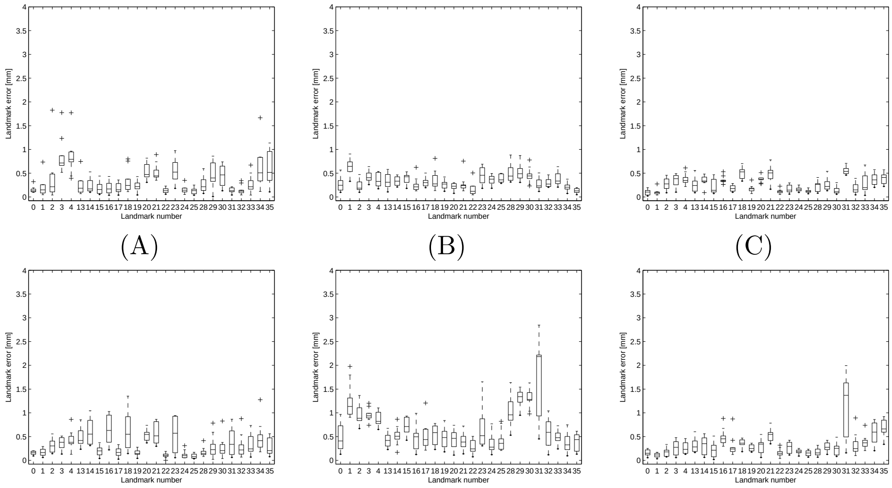

(A) (B) (C)

(D) (E) (F)

Figure 7.7: Landmark errors for wild-type mice (A-C) and Crouzon mice (D-F). Inter-observer errors (scaled by $1/\sqrt{2}$) (A,D). Landmark errors between gold standard and automatic landmarks (scaled by $\sqrt{2/3}$) using the affine approach (B,E) and the non-rigid approach (C,F). The scaling factors are applied to obtain reasonable comparisons as explained in the Appendix.

7.3.3 Automatic Assessment of Linear Skull Parameters

The skull parameters listed in Section 7.2.4 were assessed automatically using (i) affine and (ii) non-rigid registration. Figure 7.8 shows boxplots demonstrating the deviation of each of the methods from GS for each group of mice (scaled as suggested in Appendix 7.A).

Having assessed the accuracy of the automatic measurements, it is interesting

---

[2] The following definition of a box- and whisker plot is used here. The box surrounds measurements between the upper and the lower quartile of the data. The line inside the box denotes the median of the data. The maximum length of the whiskers is 1.5 times the interquartile range (IQR). Outliers (those lying outside the limits of the whiskers) are marked by a "+".

to know the true values of the parameters and see how they deviate between the two groups of mice. This is illustrated in Figure 7.9 for the GS as well as the two automatic assessments. Additionally, the group means and percentage increase or decrease are given for each of the three approaches in Table 7.2.

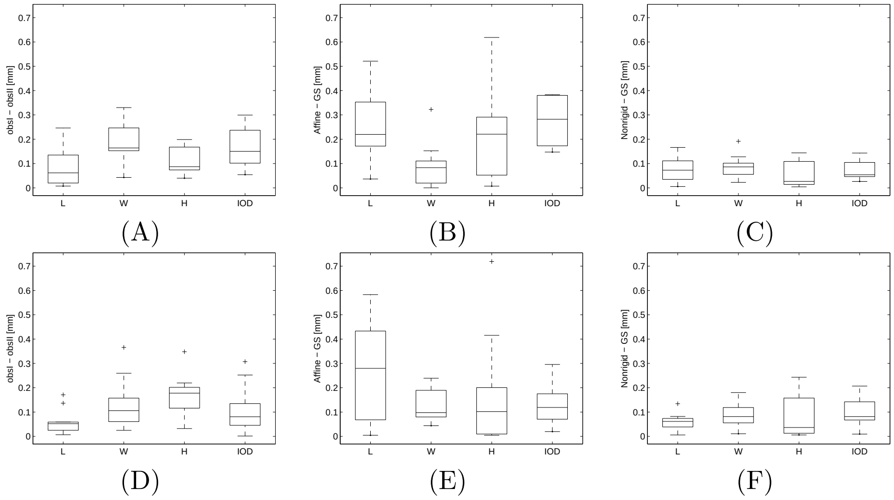

(A) (B) (C)

(D) (E) (F)

Figure 7.8: Automatic assessment of skull parameters. Absolute differences between the two different observers annotating wild-type mice (A), gold standard and affine approach on wild-type mice (B); gold standard and non-rigid approach on wild-type mice (C); the two different observers annotating Crouzon mice (D); gold standard and affine approach on Crouzon mice (E); gold standard and non-rigid approach on Crouzon mice (F). The plots are scaled as suggested in the Appendix section.

Table 7.2: Average skull parameter values for the wild-type (WT) mice and Crouzon mice assessed by the three different approaches. Additionally, percentage difference (% diff.) between the group means is given.

	Gold standard			Affine approach			Non-rigid approach		
	WT	Crouzon	% diff.	WT	Crouzon	% diff.	WT	Crouzon	% diff.
L [mm]	24.37	20.41	-16.25	24.70	20.36	-17.55	24.39	20.39	-16.40
W [mm]	10.13	10.87	7.31	10.15	10.80	6.37	10.10	10.84	7.28
H [mm]	6.83	7.53	10.28	6.94	7.44	7.16	6.72	7.44	10.81
IOD [mm]	4.04	4.51	11.64	4.38	4.66	6.37	4.08	4.57	11.77

7.3.4 Automatic Assessment of Local Deformations Between Wild-type Atlas and Crouzon atlas

In order to estimate the local deformations between the wild-type and Crouzon groups, the deformation field from the non-rigid wild-type atlas to the non-rigid Crouzon atlas was established. The obtained vector field was used to estimate displacement (in mm) at each point of the surface of the wild-type

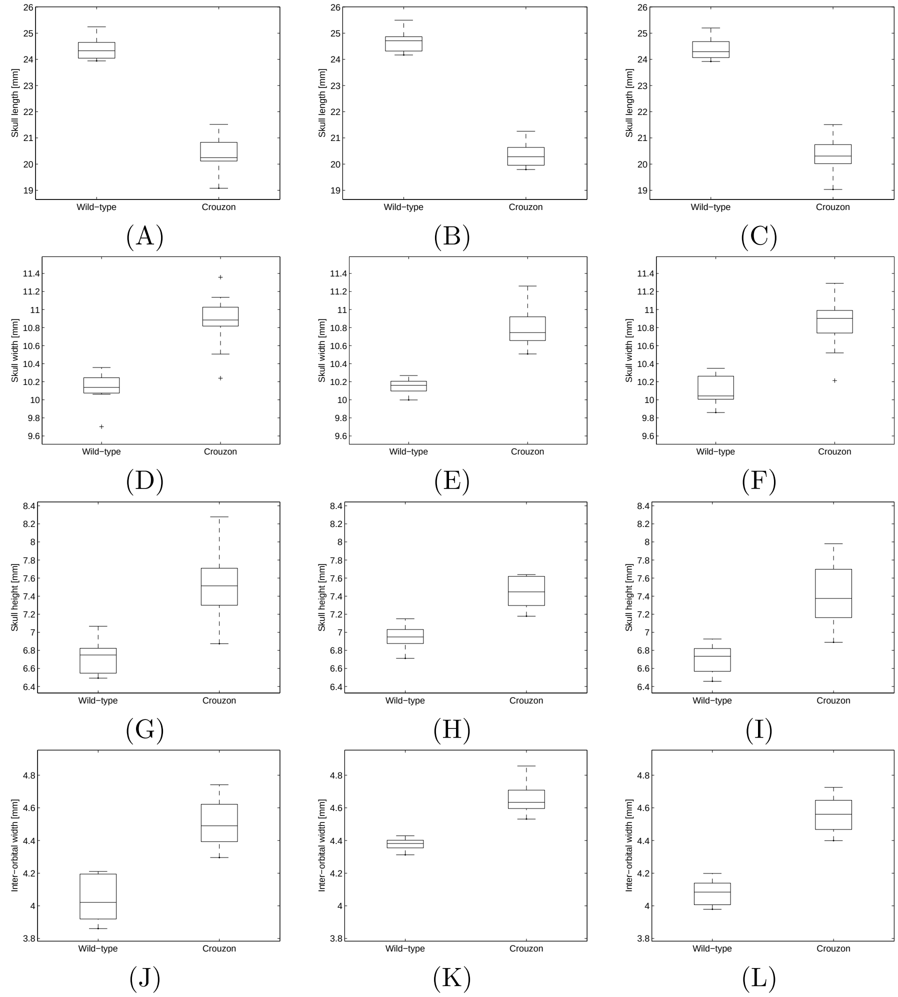

Figure 7.9: Skull length (A-C), skull width (D-F), skull height (G-I) and interorbital distance (J-L) estimated using gold standard landmarks (A,D,G,J), the affine approach (B,E,H,K) and the non-rigid approach (C,F,I,L).

atlas. Figure 7.10 shows the effect of the scaling component from T_{global} while Figure 7.11 shows the local displacements from T_{local}.

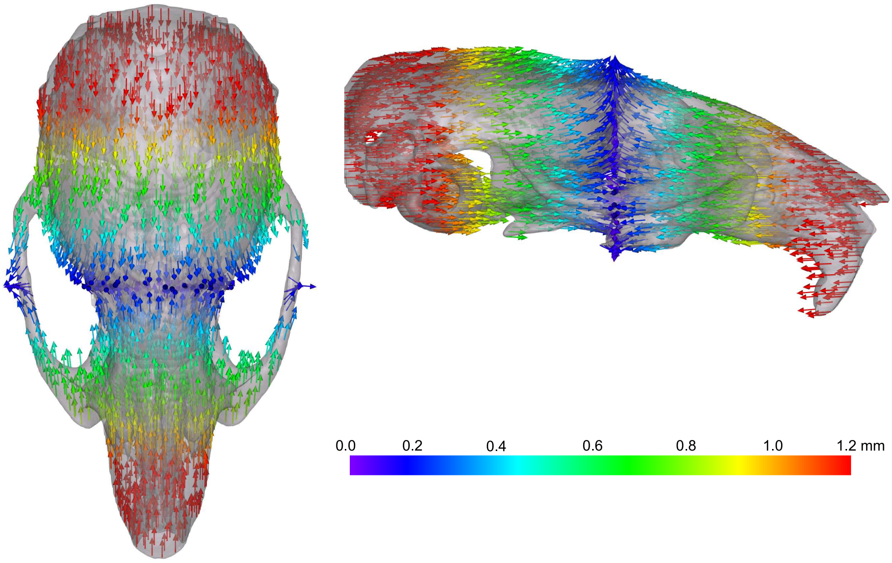

Figure 7.10: The vector field illustrating the displacement due to anisotropic scaling component of the affine registration (T_{global}) of the wild-type atlas to the Crouzon atlas visualised on the surface of the wild-type atlas. Colors denote displacements (in mm) according to color scale bars at the bottom.

7.4 Discussion

Judged from Figure 7.2 the non-rigid atlas is more accurate than the affine atlas, i.e. all structures are sharper than in the more blurry affine atlas. However, the affine atlas is much simpler to deal with considering the small number of parameters and the low computation time. The appropriate type of atlas should be selected carefully with respect to the application in question. Figures 7.5 and 7.6 imply that the non-rigid registration increases the accuracy from affine registration considerably. The post-affine-registration difference images indicate that local differences around the zygoma, the maxillary molars and at the most anterior part of the internal cranial base have not been matched accurately. In the post-non-rigid-registration difference image, however, all local structures appear to have been matched accurately during the registration.

The quantitative assessment of registration accuracy in Figure 7.7(a-c) indicates that for wild-type cases, both of the automatic methods are more consistent than the human observers. This was confirmed in the statistical analysis of the variances. In the inter-observer plot in Figure 7.7(a) there are even large outlier errors in some of the landmarks (2,3,4 and 34). This is often the risk when us-

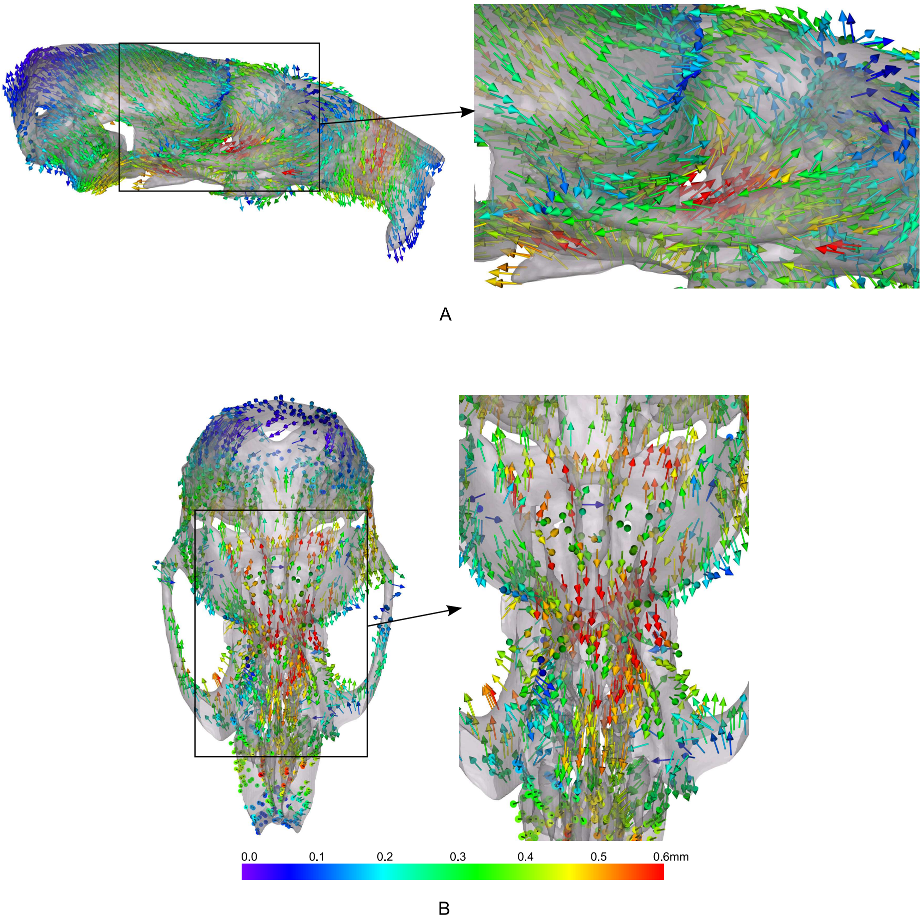

Figure 7.11: The vector field obtained from non-rigid registration (T_{local}) of the wild-type atlas to the Crouzon atlas visualised on the surface of the wild-type atlas. Colors denote displacements (in mm) according to color scale bar at the bottom. A right side view of the skull zoomed in at the region around the forehead and maxilla (A). A top view of the skull zoomed in at the cranial base (B).

ing manual assessments, since human errors cannot be prevented entirely. For both of the automatic methods (see Figure 7.7(b,c)), all errors are below 1 mm. Figure 7.7(d-e) implies that for the Crouzon cases, the non-rigid approach outperforms both the affine approach and the inter-observer errors. As confirmed in the statistical analysis, the non-rigid approach is both more robust and gives lower errors, apart from landmark #31 which seems to be problematic for both of the automatic approaches. According to Figure 7.4 this landmark is placed at nasion, e.g. at the intersection of the sutura sagittalis and the sutura frontonasalis. The fact that these sutures are not visible in some of the Crouzon cases, depending on the severity of the symptoms, makes it hard to match the region automatically, no matter which similarity measure is chosen. Experienced human observers seem to be better at guessing the position of this particular landmark. In practice this single cumbersome landmark could be assessed by a human observer after applying the non-rigid approach to automatically estimate all other landmark positions.

Figure 7.8 shows that all the absolute differences in skull parameters between observers are around 0.3 mm or lower for both groups of mice (Figure 7.8(a,d)). The absolute errors between the affine approach and the GS are slightly higher for both groups of mice (Figure 7.8(b,e)). For the non-rigid approach, the errors are around 0.1 mm and the variance of errors is very low for all parameters and both groups implying that the non-rigid approach is the most consistent (Figure 7.8(c,f)).

Testing the automatic assessments versus the GS in a t-test (5% level of significance) revealed equal means for the non-rigid approach and GS. The affine approach differed from the GS when assessing the IOD for both groups but was equally good when assessing the remaining three parameters. This might indicate that the affine approach is not adequate when assessing parameters other than those directly related to the anisotropic scaling involved in the affine registration.

Figure 7.9 implies that all three approaches (GS, affine, non-rigid) show the two groups to be different in terms of all four parameters. This was confirmed by a t-test revealing highly significant differences in the group means. Note, however, that because the affine approach failed to assess the IOD accurately, the group differences in IOD due to the affine approach are not relevant. The values from the GS and the non-rigid approach from Table 7.2 indicate that for Crouzon mice, the skull is approximately 16% shorter, 7% wider and 10-11% higher. The IOD is 11-12% higher for Crouzon cases. These findings are in good agreement with earlier studies on humans and mice, as seen in Table 7.1 (calvaria, orbital region) [117, 173].

Figure 7.10 indicates that the scaling differences between the two groups occur mainly in the sagittal axis, as expected due to the large difference in skull length between the two groups. Judged from Figure 7.11(a), the zygoma is approximately 0.8 mm shorter in the Crouzon cases (since it is decreased by 0.4 mm at both“ends”). Furthermore, Figure 7.11(b) reveals that the largest local differences (0.6 mm and larger deviation) occur at the cranial base and in the nasal region. The average Crouzon case has an angulation in the cranial base and a bending in the nasal region. As seen in Table 7.1, shortening of nasal bone and cavities have previously been reported for humans and mice [23, 117, 173].

Moreover, the shortening of the zygoma has been reported in humans [117]. However, the angulation of the cranial base is a new finding and it is believed that it is worth a further study with respect to humans.

With respect to the methodology, it is concluded that the non-rigid approach outperforms the affine approach, with respect to both landmark accuracy and the automatic linear measurements on the skull. When examining local, non-linear deviations, a non-rigid approach becomes essential. Future work includes a further analysis of the local deformations, incorporating statistical tests on the deformation field to estimate the significance of the findings.

7.5 Acknowledgements

H. Ólafsdóttir is supported by a PhD-grant from the Technical University of Denmark. E. Oubel is supported by an FPU Scholarship and Dr. Frangi is supported by a Ramon y Cajal Research Fellowship and by Grant TEC2006-03617 all from the Spanish Ministry of Education and Science, a Grant CENIT-CDTEAM from the Spanish Ministry of Industry (CDTI). This work was also partially supported by Grants CB06/01/0061, FIS2004/40676, and FIS 04/040676 from the Spanish Ministry of Health. Chad A. Perlyn is supported by a Plastic Surgery Educational Foundation (PSEF) Grant.

For all image registrations, the Image Registration Toolkit was used under Licence from Ixico Ltd.

7.A Comparing the Error of an Automatic Method with the Error of an Observer in the Absence of a Gold Standard.

It is often desirable to be able to compare an automatic or semi-automatic method with the human error. In many cases this is complicated by the fact that one does not know the truth, i.e. one does not have a so-called gold standard. Probably the most commonly cited reference for this and similar kinds of situation is that of Bland & Altman [13].

Here we will specialise to the present case where two human observers placed points on a 3D structure. This is to be compared to the placement of the same points by an automatic method. In such a setting it is possible to estimate the observer error (variance) and the error (variance) of the automatic method.

For simplicity assume the one-dimensional case where we ask each of the observers to mark the position of a point x. We assume the correct - but unknown - position is μ. We further assume that each human observer has his own bias and error variance and that they are independent of each other. Similarly the automatic method is assumed to have it's own bias and error variance. We also assume independence between the automatic method and the observers.[3] Finally, the assumption of normality is useful in order to set up formal statistical tests. The above can be written

$$X_1 \in N\left(\mu_1, \sigma_1^2\right), \qquad X_2 \in N\left(\mu_2, \sigma_2^2\right), \qquad X_A \in N\left(\mu_A, \sigma_A^2\right), \tag{7.7}$$

where X_1, X_2 and X_A are independent. At least the following two quantities are considered important:

1. comparison of the two observers shown as the difference between them: $D_{1,2} = X_1 - X_2$
2. comparison of the automatic method with the average of the observers: $D_{A,12} = X_A - (X_1 + X_2)/2$

It can easily be shown that these quantities are distributed as:

$$\begin{aligned} D_{1,2} &\in N\left(\mu_1 - \mu_2, \sigma_1^2 + \sigma_2^2\right), \\ D_{A,12} &\in N\left(\mu_A - \frac{\mu_1 + \mu_2}{2}, \sigma_A^2 + \frac{\sigma_1^2 + \sigma_2^2}{4}\right), \end{aligned} \tag{7.8}$$

---

[3] In many cases the latter assumption is questionable, since the automatic method is often "trained" using the data from the observers with whom we wish to compare. However, we assume it is valid if we use cross-validation. Alternatively, the automatic method could be trained against a third observer.

where $D_{1,2}$ and $D_{A,12}$ are independent. From the above we note that it is possible to test the differences in bias ($\mathrm{H}_{01} : \mu_1 = \mu_2$ and $\mathrm{H}_{02} : \mu_A = (\mu_1 + \mu_2)/2$) using t-tests.

Furthermore, if we introduce the average observer variance as $\sigma^2 = (\sigma_1^2 + \sigma_2^2)/2$ we get:

$$\begin{aligned} D_{1,2} &\in N\left(\mu_1 - \mu_2, 2\sigma^2\right) \\ D_{A,12} &\in N\left(\mu_A - \frac{\mu_1 + \mu_2}{2}, \sigma_A^2 + \frac{\sigma^2}{2}\right), \end{aligned} \tag{7.9}$$

where $D_{1,2}$ and $D_{A,12}$ are independent. From this we see that with no knowledge of the correct position (no gold standard), the average observer variance can be estimated as half the variance of the differences between the observer positions. Furthermore, the automatic method variance can be estimated by subtracting off the estimated observer variance from the empirical variance of the differences between the automatic method and the average of the two observers. Finally, we note that the two types of differences are independent and thus uncorrelated.

A formal F-test of the hypothesis that e.g. the variance of the automatic method is equal to that of an observer ($\mathrm{H}_0 : \sigma_A^2 = \sigma^2$) can now be performed by adjusting the respective empirical variances by factors 1/2 and 2/3.

The adjustment can also be performed directly on the differences using the factors $1/\sqrt{2}$ and $\sqrt{2/3}$ respectively. This is useful for plotting purposes since plots of the two types of differences can be compared more easily - especially when we can assume no bias (or at least that they are equal).

The above was derived for 1D. Similar derivations can be done for 3D. However, if positioning-error in the x, y, and z-dimension can be assumed independent of each other and with the same variance, then the variance estimates can be pooled. This is equivalent to having three times the number of observations.

Chapter 8

Craniofacial Statistical Deformation Models of Wild-type Mice and Crouzon Mice

Hildur Ólafsdóttir, Tron A. Darvann, Bjarne K. Ersbøll, Nuno V. Hermann, Estanislao Oubel, Rasmus Larsen, Alejandro F. Frangi, Per Larsen, Chad A. Perlyn, Gillian M. Morriss-Kay, Sven Kreiborg

Abstract

Crouzon syndrome is characterised by premature fusion of cranial sutures and synchondroses leading to craniofacial growth disturbances. The gene causing the syndrome was discovered approximately a decade ago and recently the first mouse model of the syndrome was generated. In this study, a set of micro-CT scans of the heads of wild-type (normal) mice and Crouzon mice were investigated. Statistical deformation models were built to assess the anatomical differences between the groups, as well as the within-group anatomical variation. Following the approach by Rueckert et al. we built an atlas using B-spline-based non-rigid registration and subsequently, all cases were non-rigidly registered to the atlas. The parameters of these registrations were then used as input to a PCA. Using different sets of registration parameters, different models were constructed to describe (i) the difference between the two groups in anatomical variation and (ii) the within-group variation. These models confirmed many known traits in the wild-type and Crouzon mouse craniofacial anatomy. However, they also showed some new traits.

8.1 Introduction

Crouzon syndrome was first described nearly a century ago when calvarial deformities, facial anomalies, and abnormal protrusion of the eyeballs were reported in a mother and her son [43]. Later, the condition was characterised as a constellation of premature fusion of the cranial sutures (craniosynostosis), orbital deformity, maxillary hypoplasia, beaked nose, crowding of teeth, and high arched or cleft palate. Heterozygous mutations in the gene encoding *fibroblast growth factor receptor type 2* (*FGFR2*) have been found responsible for Crouzon syndrome [180]. Recently a mouse model was created to study one of these mutations ($FGFR2^{Cys342Tyr}$)[63]. Incorporating advanced small animal imaging techniques such as micro-CT, allows for detailed examination of the craniofacial growth disturbances. Studying the craniofacial shape differences in detail contributes to the understanding of the syndrome, surgery planning and diagnosis in humans. A recent study, performing linear measurements on micro-CT scans, proved the mouse model applicable to reflect the craniofacial deviations occurring in humans with Crouzon syndrome [173]. Previously, we have extended this study to assess the local deformations between the groups by constructing a deformable shape- and intensity-based atlas of representing each group of mice. The deformation field between the two atlases was then examined [162].

In order to analyse and interpret deformation fields in a meaningful way, it is desirable to reduce the large number of dimensions and at the same time localise the deviations with respect to the atlas. This leads us to Statistical Deformation Models (SDMs). These are closely related to statistical shape models but the fact that the whole correspondence field is modelled makes them more powerful.

The focus of this paper will be to use the SDMs to (i) describe the anatomical variability between the two groups, i.e. extract the differences, and (ii) describe the anatomical variability within each of the two groups.

8.2 Data Material

Production of the $Fgfr2^{C342Y/+}$ and $Fgfr2^{C342Y/C342Y}$ mutant mouse (Crouzon mouse) has been previously described [63]. All procedures were carried out in agreement with the United Kingdom Animals (Scientific Procedures) Act, guidelines of the Home Office, and regulations of the University of Oxford.

For three-dimensional (3D) CT scanning, 10 wild-type and 10 $Fgfr2^{C342Y/+}$ specimens at six weeks of age (42 days) were sacrificed using Schedule I methods and fixed in 95% ethanol. They were sealed in conical tubes and shipped to the micro-CT imaging facility at the University of Utah. Images of the skull were obtained at approximately $46\mu m \times 46\mu m \times 46\mu m$ resolution using a General Electric Medical Systems EVS-RS9 micro-CT scanner. Prior to analysis of the images the mandible was masked out for all 20 specimens. This was due to different jaw positions and the fact that the deviation in mandible shape is a secondary effect of the syndrome. Figure 8.1 shows an example of the living mice and the imaging data appearance.

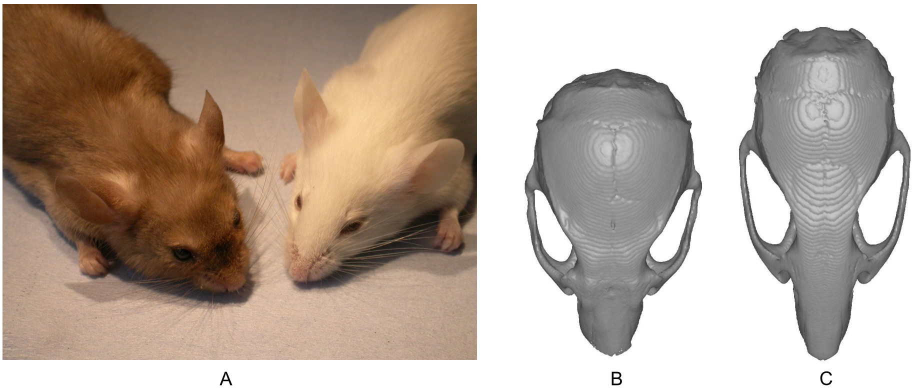

Figure 8.1: (a) Photo of a Crouzon mouse (left) and a wild-type mouse (right). Skulls extracted from CT images of (b) a Crouzon mouse, (c) a wild-type mouse.

8.3 Methods

The steps taken to automatically build a SDM are the following.

1. Build an atlas from a set of images using non-rigid image registration.
2. Match the anatomy of the atlas to the corresponding anatomies of the cases to be included in the model using non-rigid image registration.

3. Build a Statistical Deformation Model applying a PCA to the resulting deformation fields.

8.3.1 Registration and Atlas Building

For steps 1 and 2 above, the non-rigid registration algorithm based on B-splines [185, 188] was applied. This algorithm uses a transformation model which is a combination of a global and a local transformation model,

$$\mathbf{T}(\mathbf{x}) = \mathbf{T}_{\text{global}}(\mathbf{x}) + \mathbf{T}_{\text{local}}(\mathbf{x}). \tag{8.1}$$

The global transformation model consists of an affine transformation matrix. The local transformation model describing the non-rigid part of the model is written by the tensor product of 1D cubic B-splines,

$$\mathbf{T}_{local}(x, y, z) = \sum_{l=0}^{3}\sum_{m=0}^{3}\sum_{n=0}^{3} B_l(u)B_m(v)B_n(w)\mathbf{c}_{i+l,j+m,k+n} \tag{8.2}$$

where $\mathbf{c}$ are the parameters (control points) of the B-splines ordered in a $p_x \times p_y \times p_y$ lattice. i, j and k are the control point positions and u, v and w are the (x, y, z) image coordinates transformed into the lattice coordinates.

8.3.2 Statistical Deformation Model

Statistical deformation models are closely related to statistical shape models. The key difference is that shape models require shapes represented by points which correspond over the set. This is dependent on manual labour although many authors have suggested approaches to reduce this.[56, 70, 76] Statistical deformation models aim at modelling the deformation fields acquired by the set of non-rigid registrations, each initiated in the common reference (atlas image or a selected image from the set to be modelled). In this way, anatomical variability in the full volume is obtained, not only in a segmented shape.

In this paper, we follow the approach by Rueckert et al. [187]. They take advantage of the fact that the parameters of the B-splines (the control points displacements) compactly represent the correspondence field between the image of interest and the target. Now the control points displacements can be used as input to PCA in order to model the deformations of the group of subjects defined in the domain of the atlas. Concatenating the 3D control points for subject s into a row vector $\mathbf{C}_s = [c_1, ..., c_p]$, where $p = 3p_xp_yp_z$, gives the sth row of the $n \times p$ data matrix to analyse, where n is the number of observations.

We define the mean deformation

$$\bar{\mathbf{C}} = \frac{1}{n}\sum_{s=1}^{n}\mathbf{C}_s$$

and the covariance matrix

$$\frac{1}{n-1}\sum_{s=1}^{n}(\mathbf{C}_s - \bar{\mathbf{C}})(\mathbf{C}_s - \bar{\mathbf{C}})^T.$$

An eigenanalysis on the covariance matrix gives the matrix of eigenvectors $\mathbf{\Phi}$ and the corresponding eigenvalues, λ. Now, a new control point instance can be generated by the model,

$$\hat{\mathbf{C}} = \bar{\mathbf{C}} + \Phi\mathbf{b}.$$

Typically, the number of eigenvectors, t, included in the model is chosen so that they explain at least 95% of the variance in the model. Now $\mathbf{b}$ is the t-dimensional vector of model parameters.

8.3.3 Modelling Approaches

In order to describe as compactly and descriptively as possible the different types of variations of interest, the types of atlases and transformation models in the registrations need to be considered.

To model the differences between groups, we use a wild-type mouse atlas, built from the group of wild-type mice. Depending on the kind of variation we are interested in modelling, we use different global transformation models (T_{global}) in the registrations. In our previous study, we used nine degrees of freedom (rotation, translation and anisotropic scaling), noting that the largest differences between the groups occur in skull length, width and height [162]. The local model in this case provides the local differences between the groups left, when height, width and length have been removed. This gives us an interesting view of the group differences, but is perhaps not very intuitive. Including height, width and length differences in the local model gives a more intuitive model. Hence, the registrations were repeated using a global model with six degrees of freedom (rotation and translation) and a local model covering the height, width and length differences. We will refer to the two different combined local models as model A and model B, with height, width and length differences excluded and included, respectively.

In order to describe the within-group variation compactly, an atlas descriptive of the group in question was used as a reference for the registrations (the wild-type atlas for the wild-type mouse model and a Crouzon atlas for the Crouzon mouse model). Seven degrees of freedom were used in the global model, i.e. translation, rotation and an isotropic scaling. Hence, the effect of pose and size was removed from the local model. We could possibly have used the deformations of model A, but this was not considered appropriate since there is no hypothesis stating that within-group variation systematically involves anisotropic scaling differences. Table 8.1 summarises the different modelling approaches.

Table 8.1: Modelling approaches

Model	Reference anatomy	DOF in T_{global}	Covered by local model
A	Wild-type atlas	9	Local deformations
B	Wild-type atlas	6	Height, length, width, local deformations
Wild-type	Wild-type atlas	7	Local deformations
Crouzon	Crouzon atlas	7	Local deformations

8.4 Experimental Results

Each type of registration from Table 8.1 was carried out hierarchically, using local models with control point spacing of 3, 1.5 and 0.75 mm for model A and the within-group models. For model B, control point spacing of 6, 3, 1.5 and 0.75 mm for model B was applied since the length differences required more than 3mm spacing to be covered by the local transformation only.

8.4.1 Registration Accuracy

Sufficient accuracy of the image registration algorithm is essential for the deformation model to be valid. In our previous work, manual annotations from two observers were used to assess the registration accuracy of model A. Using the optimal transformations from the image registrations, landmarks were obtained automatically. The landmark positions were statistically compared to those annotated by the human observers. This showed that the automatic method provided as good accuracy as the human observers and moreover, it was more precise, judged from the significantly lower standard deviation. [162] Following the same approach for model B, Figure 8.2 shows the landmark errors for 26 landmarks set by the two observers as compared to the automatically obtained landmarks. We show this for Crouzon cases only since it is considered a more challenging task. For the wild-type cases even better results are obtained. The plots are scaled to obtain reasonable comparisons as suggested in our previous work [162]. Statistical comparison of the landmark position revealed the same main conclusions as the ones from the previous study on model A. Additionally, similar results were obtained for the within-group models. In conclusion, we have established a good basis for reliable deformation models.

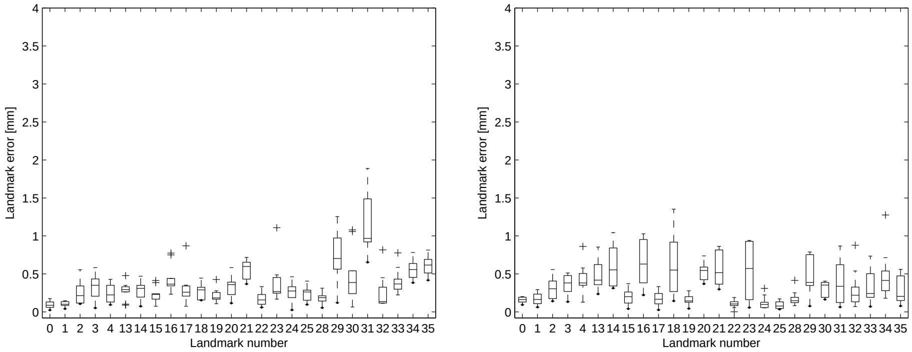

(a)

(b)

Figure 8.2: (a) Landmark errors for Crouzon mice between (a) automatic approach using model B and gold standard; (b) observer I and observer II.

8.4.2 SDM of Crouzon and Wild-type Mice

A SDM was built for both types of local transformation, i.e. without and with (anisotropic) scaling differences (model A and model B). In each case, a PCA was applied to the matrix of control points with $n = 20$ observations. For model A, $p = 15525$ and for model B, $p = 21675$. For model A, 15 principal modes were required to retain 95% of the variation in local deformation from average anatomy. For model B, on the other hand, 10 principal modes were required. A plot of the cumulative variance across modes for each model is shown in Figure 8.3. The observations, projected into the space of the first six modes of variation, are shown in Figure 8.4 for models A, and B.

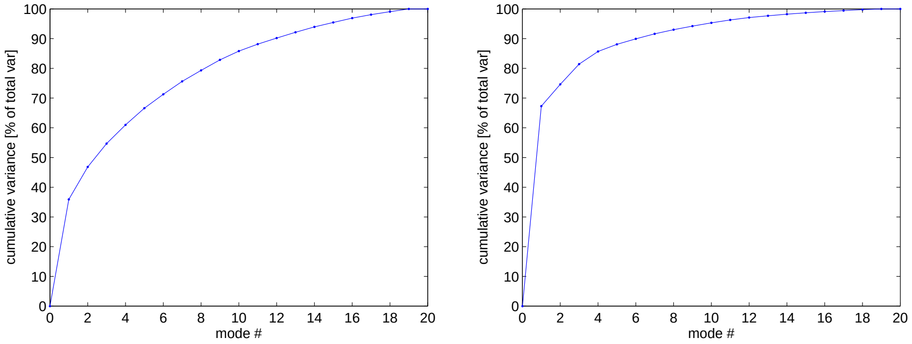

(a)

(b)

Figure 8.3: Cumulative variance across the modes of the statistical deformation model. (a) Model A (b) Model B .

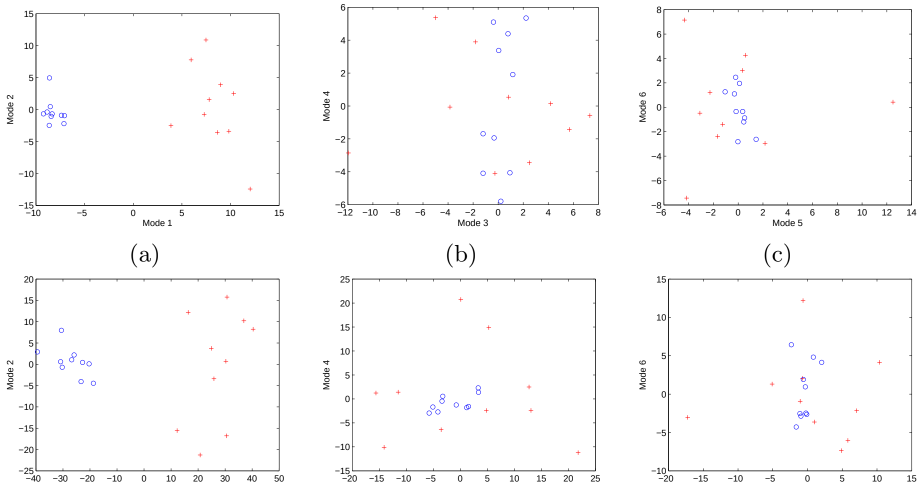

(a) (b) (c)

(d) (e) (f)

Figure 8.4: Projection of observations into the space of the first six principal components for model A (a-c) and model B (d-f). Crosses denote Crouzon cases while circles denote wild-type cases. (a,d) Mode 2 vs. mode 1; (b,e) Mode 4 vs. mode 3; (c,f) Mode 6 vs. mode 5.

Figures 8.5 and 8.6 show the first mode of variation for models A and B, respectively shown by extracting the skull surface from the atlas and deforming it by the model. This mode is discriminating for the two groups.

8.4.3 Within-group SDMs

A SDM of the wild-type mouse anatomy was built using the control point vectors from the wild-type local model, which form a data matrix with $n = 10$ and $p = 15525$. Eight modes of variation were required to capture 95% of the total variance. Figure 8.7 shows the first and second mode of variation in the wild-type mouse craniofacial SDM.

A similar data matrix was obtained from the Crouzon local model. The craniofacial Crouzon SDM required eight modes of variation to capture 95% of the total variance.

Figure 8.5: First mode of deformation variation, after removing height, length and width differences (model A). (a,c,e) Atlas deformed towards the most extreme wild-type case, (b,d,f) Atlas deformed towards the most extreme Crouzon case. (a,b): top view; (c,d): side view; (e,f): front view.

8.5 Discussion

Figure 8.3 shows that the main difference between model A and B is the proportion of variance explained by the first mode. As expected, the first mode of model B explains a large proportion of variance, since the length, width and height differences are considerable. Figure 8.4 shows that for both of the com-

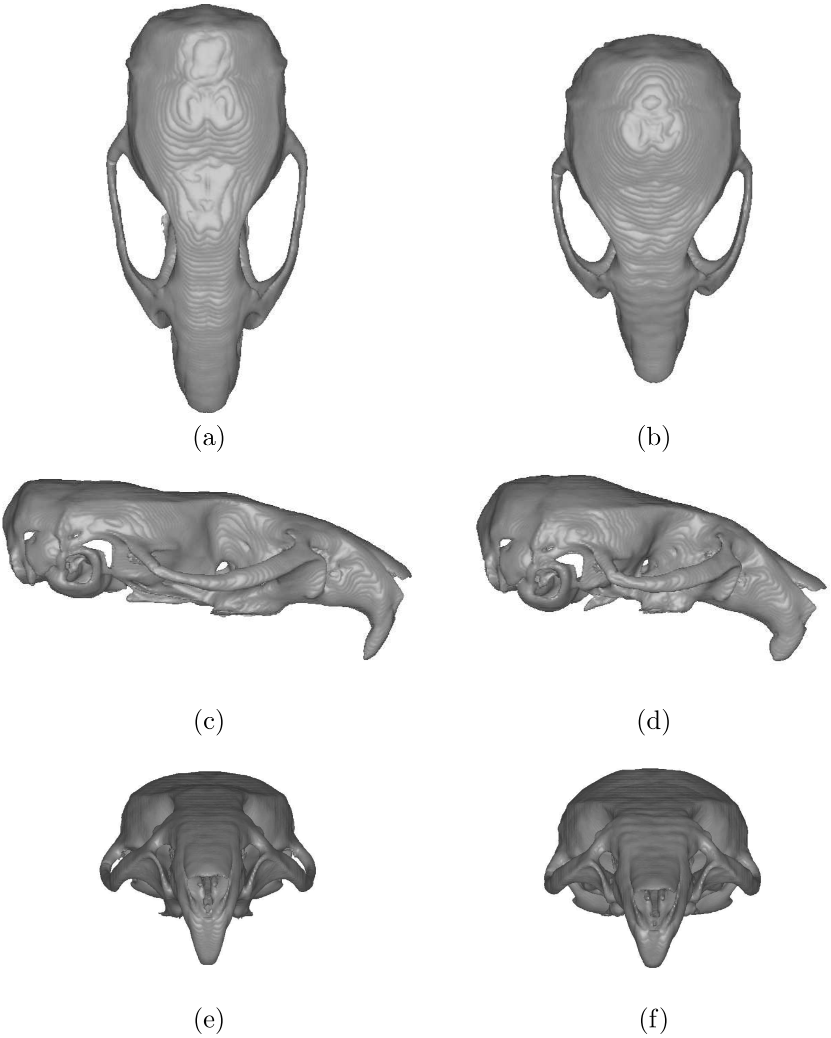
(a) (b)
(c) (d)
(e) (f)

Figure 8.6: First mode of deformation variation, with height, width and length included in the local model (model B) (a,c,e) Atlas deformed towards the most extreme wild-type case, (b,d,f) Atlas deformed towards the most extreme Crouzon case. (a,b): top view; (c,d): side view; (e,f): front view.

bined models (A and B), only the first mode of variation is discriminating for the two groups. The remaining modes describe other types of variation than the one related to group differences. It is also noted from this figure that the variability in the Crouzon mouse group is for most modes considerably larger than for wild-type cases. This is often the case when comparing a control group

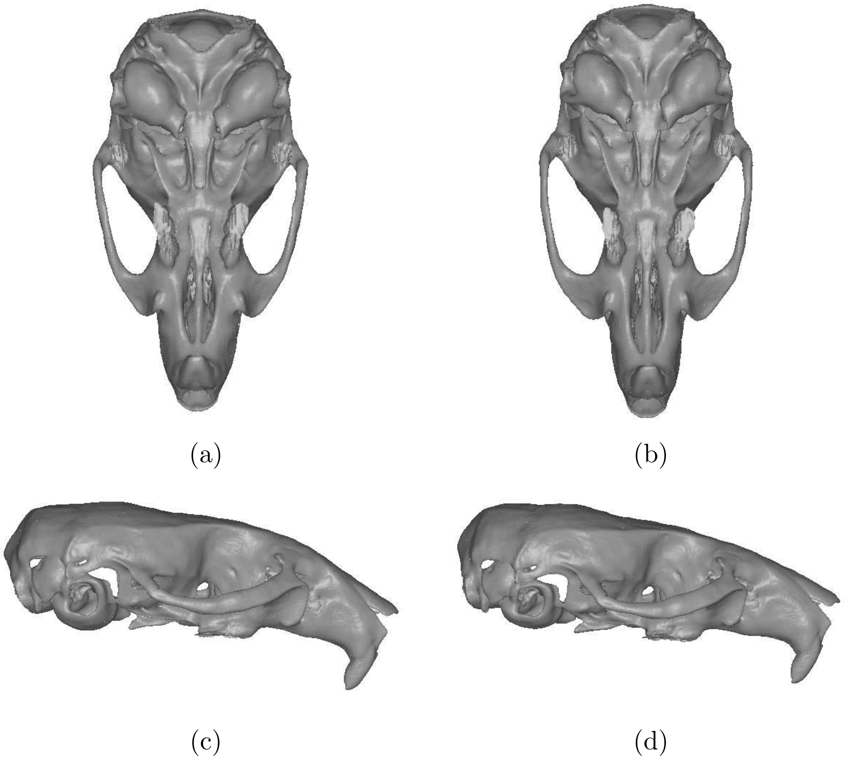

Figure 8.7: Second and fifth mode of variation for wild-type mouse SDM. Atlas deformed (a) -2 std. dev. (b) +2 std. dev. along the second principal component. Atlas deformed (c) -2 std. dev. (d) +2 std. dev. along the fifth principal component. Note the different shape of the zygoma in (a,b), the curved form of the calvaria and bending of nose in (c,d).

to a diseased group.

For model A, it is noted that in the Crouzon case, the maxillary molar teeth are located posteriorly relative to the wild-type (see Figure 8.5, (c,d) causing a malocclusion. Additionally, the Crouzon mice have a shorter cranial base (see Figure 8.5, (c,d)), a shorter nose (as measured from sutura frontonasalis, see Figure 8.5, (a,b)). These three traits have earlier been observed in human subjects [117]. Furthermore, this model describes a constriction of the cranial base, meaning that while the calvaria becomes higher, the cranial base becomes shorter and over bent (see Figure 8.5, (c-f)). This confirms a result from our previous study where the deformation field between a Crouzon mouse atlas to the wild-type mouse atlas was inspected. [162] This interesting effect has not been reported before, and calls for a further investigation. As expected, the

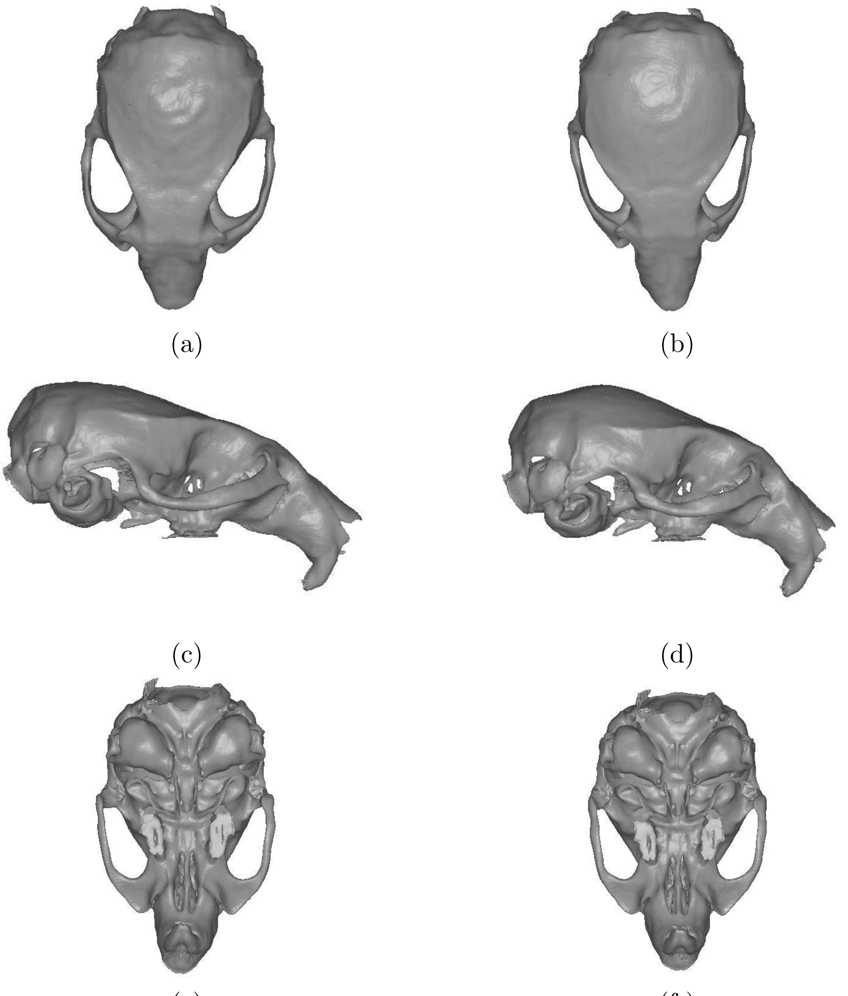

(a) (b) (c) (d) (e) (f)

Figure 8.8: Second, third and sixth mode of variation for Crouzon mouse SDM. Crouzon atlas deformed (a) -2 std. dev. (b) +2 std. dev. along the second principal component, top view. Crouzon atlas deformed (c) -2 std. dev. (d) +2 std. dev. along the third principal component, side view. Crouzon atlas deformed (e) -2 std. dev. (f) +2 std. dev. along the sixth principal component, bottom view. Note the different shape and symmetry of zygoma in (a,b), different curving of calvaria and nose bending in (c,d) and nose orientation in (e,f)

largest variation in model B is due to differences in length, height and width.

The fact that only the first mode of variation differentiates between the groups makes the model more difficult to interpret and probably some differences between the groups are not represented in this mode. Ongoing and future work is therefore to use more powerful techniques than PCA to distribute the variation across modes.

The wild-type mouse SDM in Figure 8.7 indicates that wild-type mice vary in shape of the zygoma (Figure 8.7(a,b)) and the curvature of the calvaria and nose bending (Figure 8.7(c,d)).

The Crouzon SDM in Figure 8.8 shows that Crouzon mice vary in shape and asymmetry of zygoma (Figure 8.8 (a,b)). Judged from the third mode, Crouzon mice have different degree of curved calvaria and bending of the nose (Figure 8.8 (c,d)). The sixth mode mainly describes the orientation and asymmetry of the nose (Figure 8.8 (e,f)). The asymmetric behavior noted in the second and sixth mode (and more not shown here) is understandable due to the syndrome´s nature of full or partial cranial suture fusing, at different sides of the skull. The fact that both wild-type mice and Crouzon mice vary in shape of zygoma and curving of calvaria indicates that this is a normal, biological variation. However, the Crouzon variation is more extreme, which is in agreement with the previous observation of large variability in the Crouzon group.

8.6 Conclusion

The combined SDMs confirmed many known traits in the craniofacial anatomy, which already had been reported with respect to human Crouzon subjects. Model A revealed more detailed anatomical differences, while model B gave the most obvious differences, and in that sense was more intuitive, while the actual local differences were hardly visible. The within-group models showed similar variation, but the Crouzon model had more extreme variation. Some of the Crouzon modes were asymmetric, which is probably due to asymmetric fusion of sutures, both in terms of the location of sutures and the timing of fusion.

In conclusion, we have built reliable SDMs using the appropriate registration models, which confirm known traits in the Crouzon mouse anatomy. Additionally, traits, which have not, yet, been reported in humans, were discovered and should be further investigated in the future.

8.7 Acknowledgements

For all image registrations, the Image Registration Toolkit was used under Licence from Ixico Ltd.

CHAPTER 9

Sparse Statistical Deformation Model for the Analysis of Craniofacial Malformations in the Crouzon Mouse

---

Hildur Ólafsdóttir, Michael Sass Hansen, Karl Sjöstrand, Tron A. Darvann, Nuno V. Hermann, Estanislao Oubel, Bjarne K. Ersbøll, Rasmus Larsen, Alejandro F. Frangi, Per Larsen, Chad A. Perlyn, Gillian M. Morriss-Kay and Sven Kreiborg.

Abstract

Crouzon syndrome is characterised by the premature fusion of cranial sutures. Recently the first genetic Crouzon mouse model was generated. In this study, Micro CT skull scans of wild-type mice and Crouzon mice were investigated. Using non-rigid registration, a wild-type craniofacial mouse atlas was built. All subjects were registered to this reference atlas providing parameters controlling the deformations for each subject. Our previous PCA-based statistical deformation model on these parameters revealed only one discriminating mode of variation. Aiming at distributing the discriminating variation over more modes we built a different model using Independent Component Analysis (ICA). Here, we focus on a third method, sparse PCA (SPCA), which aims at approximating the properties of a standard PCA while introducing sparse modes of variation. The results show that SPCA outperforms both ICA and PCA with respect to the Fisher discriminant, although many similarities are found with respect to ICA.

9.1 Introduction

Crouzon syndrome was first described nearly a century ago when calvarial deformities, facial anomalies, and abnormal protrusion of the eyeball were reported in a mother and her son [43]. Later, the condition was characterised as a constellation of premature fusion of the cranial sutures (craniosynostosis), orbital deformity, maxillary hypoplasia, beaked nose, crowding of teeth, and high arched or cleft palate. Heterozygous mutations in the gene encoding *fibroblast growth factor receptor type 2* (*FGFR2*) have been found responsible for Crouzon syndrome [180]. Recently a mouse model was created to study one of these mutations ($FGFR2^{Cys342Tyr}$)[63]. Incorporating advanced small animal imaging techniques such as Micro CT, allows for detailed examination of the craniofacial growth disturbances. Studying the craniofacial shape differences in detail contributes to the understanding of the syndrome, surgery planning and diagnosis in humans. A recent study, performing linear measurements on Micro CT scans, proved the mouse model applicable to reflect the craniofacial deviations occurring in humans with Crouzon syndrome [173]. Previously, we have extended this study to assess the local deformations between the groups by constructing a deformable shape and intensity-based atlas of wild-type (normal) mouse skulls [162]. Deforming the anatomy of this atlas to all mice, the craniofacial shape differences may be analyzed.

To analyse and interpret these deformations in a meaningful way, it is desirable to reduce the large number of dimensions and at the same time localise the growth deviations with respect to the atlas. This leads us to statistical deformation models (SDMs). These are closely related to statistical shape models but the fact that the whole correspondence field is modelled makes them more powerful. A standard PCA has been a popular approach to build SDMs [e.g. 137, 148, 187] but recently different techniques have been applied, e.g. wavelet-based PCA [237].

With respect to the mouse study, PCA was previously performed [160]. This analysis revealed only one discriminating mode of variation, mainly reflecting global differences between the groups. This kind of variation can be hard to interpret and in a recent study, we showed that applying Independent Component Analysis (ICA) to the deformation fields resulted in several discriminating modes, revealing the local differences between the groups. Sparse Principal Components Analysis (SPCA) [242] has proven successful when applied in classical shape modelling [196]. In this paper we introduce the use of SPCA to build a Sparse Statistical Deformation Model and provide a comparison to a standard

PCA and ICA with focus on the discriminative ability. We believe this is the first time SPCA is applied to statistically model deformation fields.

9.2 Data Material

Production of the $Fgfr2^{C342Y/+}$ and $Fgfr2^{C342Y/C342Y}$ mutant mouse (Crouzon mouse) has been previously described [63]. All procedures were carried out in agreement with the United Kingdom Animals (Scientific Procedures) Act, guidelines of the Home Office, and regulations of the University of Oxford.

For three-dimensional (3D) CT scanning, 10 wild-type and 10 $Fgfr2^{C342Y/+}$ specimens at six weeks of age (42 days) were sacrificed using Schedule I methods and fixed in 95% ethanol. They were sealed in conical tubes and shipped to the Micro CT imaging facility at the University of Utah. Images of the skull were obtained at approximately $46\mu\text{m} \times 46\mu\text{m} \times 46\mu\text{m}$ resolution using a General Electric Medical Systems EVS-RS9 Micro CT scanner. Figure 9.1 shows an example of the living mice and the imaging data appearance.

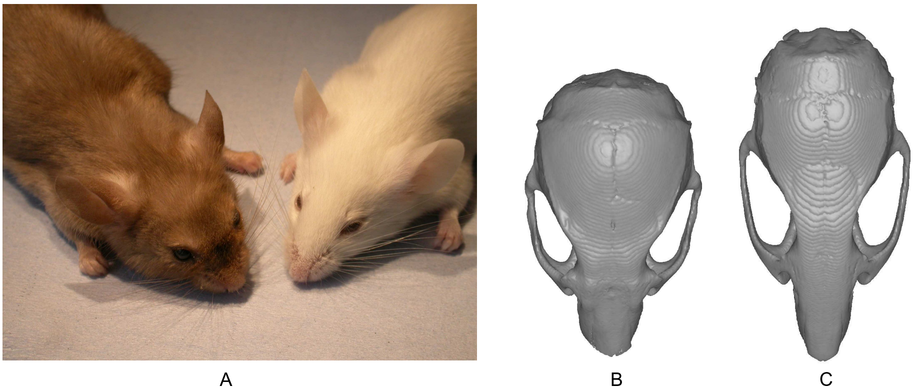

Figure 9.1: (a) Photo of a Crouzon mouse (left) and a wild-type mouse (right). Skulls Extracted from CT images of (b) a Crouzon mouse, (c) wild-type mouse.

9.3 Methods

The steps taken to automatically assess the local shape deviations between groups, statistically, from the Micro CT images are the following.

1. Build a craniofacial wild-type mouse atlas from the Micro CT images using non-rigid image registration

2. Match the anatomy of the atlas to all 20 cases (wild-type and Crouzon mice) using non-rigid image registration

3. Use the resulting deformation parameters as input to a SPCA

9.3.1 Atlas Building and Registration

The first two steps of the procedure were presented in [162]. The non-rigid registration algorithm based on B-splines [185, 188] was applied. This algorithm uses a transformation model which is a combination of a global and a local transformation model, $\mathbf{T}(\mathbf{x}) = \mathbf{T}_{\text{global}}(\mathbf{x}) + \mathbf{T}_{\text{local}}(\mathbf{x})$. The global transformation model consists in our case of a rigid transformation matrix (with 6 degrees of freedom). The local transformation model describing the non-rigid part of the model is written by the tensor product of the 1D cubic B-splines,

$$\mathbf{T}_{local}(x, y, z) = \sum_{l=0}^{3} \sum_{m=0}^{3} \sum_{n=0}^{3} B_l(u) B_m(v) B_n(w) \mathbf{c}_{i+l,j+m,k+n} \tag{9.1}$$

where $\mathbf{c}$ are the parameters of the B-splines ordered in a $p_x \times p_y \times p_y$ lattice. u, v and w are the (x, y, z) image coordinates translated into the lattice coordinates.

9.3.2 A Sparse Statistical Deformation Model

The third step of the procedure listed above is the main focus of this paper. The control points (parameters) of the B-splines in Equation 9.1 provide a compact representation of the correspondence fields. As shown in [187] it is sufficient to perform a statistical analysis on these control points to obtain a compact description of the deformations. Using a common reference frame, e.g. an atlas, as the reference in the registrations, the control points for a subject reflect its local deviation from this reference frame. Concatenating the 3D control points for subject i into a row vector $\mathbf{C}_i = [c_1, ..., c_p]$, where $p = 3p_x p_y p_z$, gives the ith row of the $n \times p$ data matrix to analyse (n is the number of observations).

SPCA approximates the properties of a standard PCA while introducing sparsity in the modes of variation. Zou et al. [242] take advantage of formulating PCA as a regression problem leading to the *SPCA criterion*

$$(\hat{\mathbf{A}}, \hat{\mathbf{B}}) = argmin_{\mathbf{A},\mathbf{B}} \sum_{i=1}^{n} ||\mathbf{x}_i - \mathbf{A}\mathbf{B}^T\mathbf{x}_i||^2 + \lambda \sum_{j=1}^{k} ||\mathbf{b}_j||^2 + \sum_{j=1}^{k} \delta_j ||\mathbf{b}_j||_1 \\ s.t.\ \mathbf{A}^T\mathbf{A} = \mathbf{I} \tag{9.2}$$

Here $\mathbf{x}_i$ denotes the ith column of $\mathbf{X}^T$. This formulation assumes k modes to be retained in the model. The columns of $\mathbf{B}$ represent the principal axes (loading vectors $\mathbf{b}_j$, $j = 1, ..., k$) and $\mathbf{B}$ projects observation i onto those axes. The matrix $\mathbf{A}$ takes the observation back to the original space. Hence, the first term measures the reconstruction error of the model. The second term, the L2 penalty is included to ensure a unique solution, also in cases where $p > n$, and the third term, L1 penalty, introduces sparsity. These two latter terms are adopted from Elastic Net regression [241]. The constraint weight, λ, must be chosen beforehand, and has the same value for all PCs, while δ may be set to different values for each PC, providing good flexibility.

The problem in Equation 9.2 is usually solved iteratively by fixing $\mathbf{A}$ in each iteration, solving for $\mathbf{B}$ using the LARS-EN algorithm [241] and recalculating $\mathbf{A}$. However, when we have $p \gg n$ as in our case, Zou et al. [242] have shown that by letting $\lambda \rightarrow \infty$, $\mathbf{B}$ can be determined by soft thresholding[1]

$$\mathbf{b}_j = (|\mathbf{a}_j^T\mathbf{X}^T\mathbf{X}| - \frac{\delta_j}{2})_+ \cdot \mathrm{sign}(\mathbf{a}_j^T\mathbf{X}^T\mathbf{X}), \qquad j = 1, 2, ..., k \tag{9.3}$$

where k is the number of modes and $\mathbf{a}_j$ is the jth column of $\mathbf{A}$. This approach was taken here enforcing the same fixed level of sparsity in each loading vector by dynamically changing (δ_j) in each iteration. To maximise the total adjusted variance [242] explained by the SPCA, the modes were ordered allowing for perturbations as suggested in [196].

Since the aim of our sparse deformation model is to discriminate between the two groups of mice the final ordering of modes was defined with respect to the Fisher discriminant. That is, the observations were projected onto the principal directions, the Fisher discriminant between the groups calculated for each mode and the principal directions ordered with respect to decreasing Fisher discriminant score. In general, for class 1 and 2, the Fisher discriminant is defined as

$$F = \frac{(\mu_1 - \mu_2)^2}{\sigma_1^2 + \sigma_2^2}, \tag{9.4}$$

where μ_i is the mean of class i and σ_i^2 is the variance of class i.

---

[1] $(z)_+$ denotes that if $z < 0$, z is set to 0 and if $z >= 0$, z is kept unchanged. The term is denoted hinge-loss.

9.4 Experimental Results

The accuracy of the image registration algorithm is essential for the deformation model to be valid. In [162], the manual annotations from two observers were used to assess the registration accuracy. Using the optimal transformations from the image registrations, landmarks were obtained automatically. The landmark positions were statistically compared to those annotated by the human observers. This showed that the automatic method provided as good accuracy as the human observers and, moreover, it was more precise, judged from the significantly lower standard deviation.

The SPCA was applied to the matrix of control points ($p = 21675$). A threshold of 2000 points was used to obtain equal sparsity in each mode of variation. Figure 9.2 (a-c) shows the observations projected onto the first six sparse principal directions (ordered by Fisher discriminant score). To evaluate the ability of the sparse SDM to assess the local group differences, it was compared to a standard PCA and our previous approach [91] using ICA [104]. Figure 9.2(d-i) shows scatter plots of the first six modes for ICA and PCA, sorted with respect to the Fisher discriminant.

The score plots already give an idea about the discrimination ability of the different approaches. To give a more quantitative measure, the Fisher discriminant was assessed in a leave-one-out fashion for all three approaches. This is plotted with error bars for each of the approaches in Figure 9.3.

With emphasis on the group differences, each mode of the sparse model was visualised by selecting the extremes from each group in model space (Figure 9.2) and project back into the space of control points. This set of control points generated from the model was then applied to the atlas surface to obtain the shapes of the two extremes. Subsequently the surfaces were extracted for visualisation. Figure 9.4 shows mode 1,3,4 and 6. Mode 2 was excluded from this visualisation due to an overlap in variation with mode 1.

Deforming the atlas along the discriminating modes of the ICA model reveals many similarities between ICA and SPCA. To give an example, Figure 9.5 shows IC 5 which is closely related to SPC 4.

9.5 Discussion and Conclusions

The score plots in Figure 9.2 indicate that both SPCA and ICA are capable of discriminating between the two groups in up to six deformation modes. The standard PCA only discriminates between the groups in the first mode. Fig-

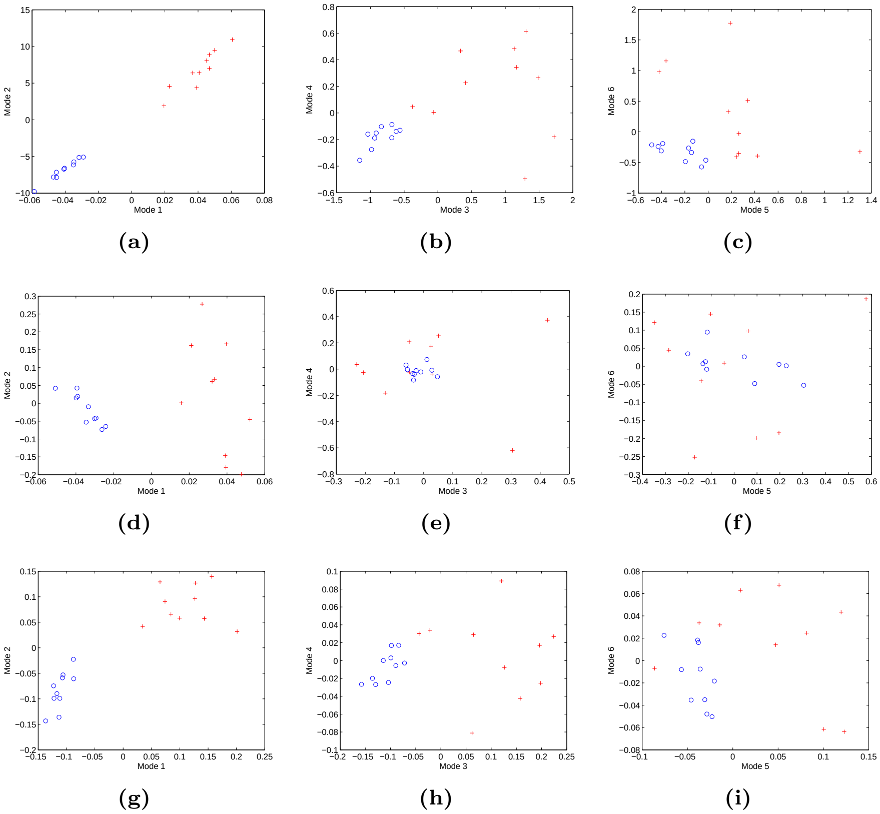

(a) **(b)** **(c)**

(d) **(e)** **(f)**

(g) **(h)** **(i)**

Figure 9.2: Projection of observations into the space of the first six components (ordered by Fisher discriminant) using (a-c) SPCA, (d-f) PCA and (g-i) ICA. Crosses denote Crouzon cases while circles denote wild-type cases. (a,d,g) Mode 2 vs. mode 1; (b,e,h) Mode 4 vs. mode 3; (c,f,i) Mode 6 vs. mode 5.

ure 9.3 confirms these speculations. It is evident that PCA is only capable of discriminating between the groups in one mode of variation. SPCA performs slightly better than the ICA, but the ICA seems to be more robust judged from the error bars. Considering the low number of points in the sparse model, this is understandable.

Visualising the sparse deformation modes in Figure 9.4 indicates that compared to wild-type mice, the skulls of Crouzon mice are higher and longer (SPC 1), they are asymmetric with respect to zygoma and nose (SPC 3), they have different shape of the middle ear and back of the head (SPC 4), and they have an angulated cranial base (SPC 6). These observations correspond up to some

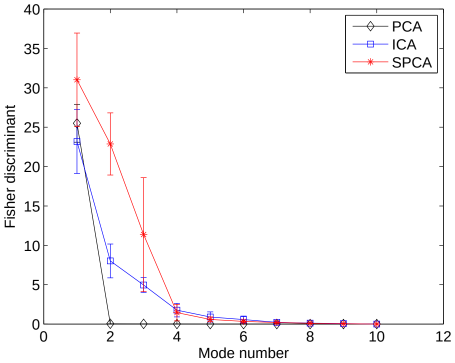

Figure 9.3: The Fisher discriminant plotted vs. deformation mode number for PCA, ICA and SPCA. The values are obtained in a leave-one-out experiment providing the error bars (one standard deviation).

degree with what has previously been seen in humans using manual measurements [e.g. 117]. The asymmetric behaviour seen in SPC 3 can be explained by the full or partial fusion of cranial sutures at different sides and different times. The different shape of the middle ear and the increased angulation of the cranial base has not been reported in humans to our knowledge and may therefore be an important contribution to the understanding of the growth disturbances. The angulation was found in mice both using ICA [91] and PCA (with global transformation model extended to 9 DOFs) [160]. The difference in shape of the middle ear and back of the head was also captured by the ICA approach as seen in Figure 9.5. In fact SPC 4 and IC 5 are extremely similar, but SPCA seems to create slightly stronger evidence for the group difference. In general, the ICA modes introduce more noise than sparse PCA, since many elements are close to 0, while in SPCA, the sparsity property avoids this. Another advantage of SPCA is that it is solely based on second order statistics making it less committed than ICA, which uses higher order statistics.

In conclusion, with respect to discriminative ability, SPCA and ICA give similar results when applied to model deformations. Both of the approaches outperform a standard PCA. However, due to the simplicity and flexibility of SPCA, it should be the preferred method for this type of analysis.

Acknowledgements

For all image registrations, the Image Registration Toolkit was used under Licence from Ixico Ltd.

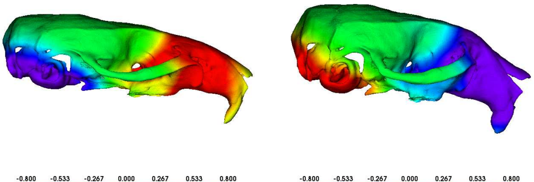

(a) SPC 1, Wild-type **(b)** SPC 1, Crouzon

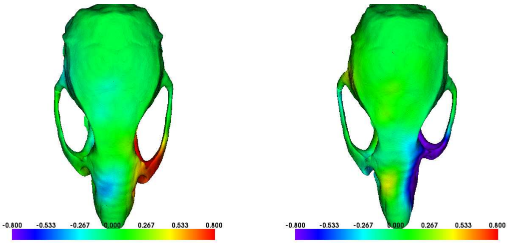

(c) SPC 3, Wild-type **(d)** SPC 3, Crouzon

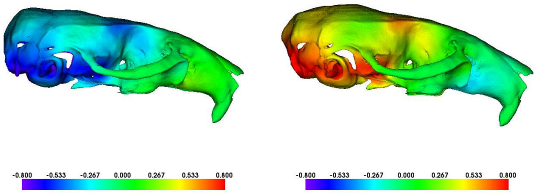

(e) SPC 4, Wild-type **(f)** SPC 4, Crouzon

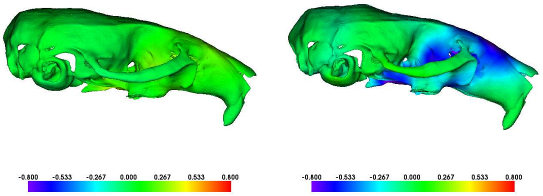

(g) SPC 6, Wild-type **(h)** SPC 6, Crouzon

Figure 9.4: Sparse Principal Deformation modes 1,3,4 and 6, visualised on surfaces after deforming to the extremes of each mode. The colors are intended to enhance the regions where changes have occurred in the deformed surfaces. The colors denote displacement with respect to atlas (in mm), with positive values (red) pointing outwards.

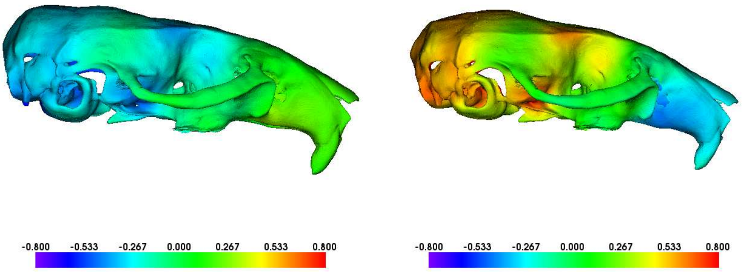

(a) IC 5, Wild-type **(b)** IC 5, Crouzon

Figure 9.5: Independent Deformation mode 5 visualised on surfaces after deforming to the extremes of the mode. The colors are intended to enhance the regions where changes have occurred in the deformed surfaces. The colors denote displacement with respect to atlas (in mm), with positive values (red) pointing outwards.

CHAPTER 10

A Statistical Model of Head Asymmetry in Infants with Deformational Plagiocephaly

Stéphanie Lanche, Tron A. Darvann, Hildur Ólafsdóttir, Nuno V. Hermann, Andrea E. Van Pelt, Daniel Govier, Marissa J. Tenenbaum, Sybill Naidoo, Per Larsen, Sven Kreiborg, Rasmus Larsen, Alex A. Kane

Abstract

Deformational plagiocephaly is a term describing cranial asymmetry and deformation commonly seen in infants. The purpose of this work was to develop a methodology for assessment and modelling of head asymmetry. The clinical population consisted of 38 infants for whom 3-dimensional surface scans of the head had been obtained both before and after their helmet orthotic treatment. Non-rigid registration of a symmetric template to each of the scans provided detailed point correspondence between scans. A new asymmetry measure was defined and was used in order to quantify and localize the asymmetry of each infant's head, and again employed to estimate the improvement of asymmetry after the helmet therapy. A statistical model of head asymmetry was developed (PCA). The main modes of variation were in good agreement with clinical observations, and the model provided an excellent and instructive quantitative description of the asymmetry present in the dataset.

10.1 Introduction

Deformational Plagiocephaly (DP) is a term describing cranial asymmetry and deformation commonly seen in infants. Its incidence has been estimated to be as high as 15% in the USA [134]. The deformity is thought to result from protracted external intrauterine pressure to the skull, followed by continued postnatal molding due to infant positioning. The incidence has increased exponentially due to the ”back to sleep” campaign to promote supine infant positioning to reduce sudden infant death syndrome. DP is manifested most commonly as either left-right asymmetry or brachycephaly (foreshortening of the head). Both are treated non-surgically. Treatments include parental education on how to prevent further deformation (e.g., alternating sleep positions [101]) and orthotic molding helmet therapy [e.g. 127, 152]. It is widely held that correction is best accomplished in infancy due to the sequence of skull mineralization, however little is known concerning the outcomes from different treatment regimens. DP affects the occiput at the back of the head and, to a lesser extent, the forehead contour. Ear position is often skewed so that the ear is anteriorly positioned on the same side as the occipital flattening. When viewed from above, the head shape can be inscribed within a parallelogram. The purposes of this work were to develop a new methodology for head asymmetry assessment and to develop a statistical model of the asymmetry (using Principal Components Analysis) in order to quantify and localize the asymmetry of each infant’s head before and after the helmet therapy and to determine the effect of helmet treatment.

10.2 Material

3D full-head surfaces of 38 patients with DP were captured at two stages, before and after treatment utilizing a 3dMD cranial$^{\mathrm{TM}}$ system (www.3dMD.com) at the Division of Plastic & Reconstructive Surgery, Washington University School of Medicine, St. Louis, MO, USA. All infants commenced their helmet treatments before 6 months of age, and were treated for a maximum of 6 months. Figure 10.1 presents examples of these scans.

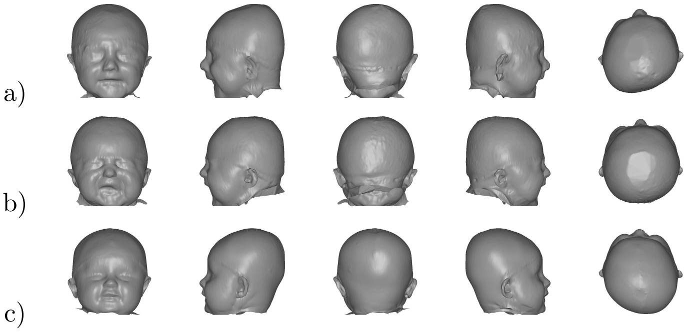

Figure 10.1: Five different views of three of the captured 3D full head surfaces. a) Right-sided flattening posteriorly and left-sided flattening anteriorly. b) Brachycephaly. c) Left-sided flattening posteriorly and right-sided flattening anteriorly.

10.3 Methods

10.3.1 Template Matching

The method used for computation and modelling of asymmetry (described in the forthcoming sections) requires establishment of detailed point correspondence between surface points on the left and right sides of the head, respectively. This is achieved through a process of template matching, whereby a symmetric "ideal" head surface (template) is oriented and deformed to assume the shape of the patient's head surface [54]. The process consists of three steps:
1. Non-isotropic scaling of the template to the patient surface.
2. Rigid orientation of the patient surface to the scaled template surface, using ear-landmarks and nasion.
3. Non-rigid deformation of the scaled template surface to the oriented patient surface using a Thin Plate Spline (TPS) controlled by 22 manually placed facial and ear landmarks, and 40 constructed landmarks on the top of the head. The latter landmarks are determined by intersecting the surfaces with 40 radial lines (equidistant in terms of angle) originating from the midpoint between the ears. They are necessary in order to control the deformation at the top and back of the head where there are no visible anatomical landmarks.

10.3.2 Asymmetry Computation

The definition of the asymmetry A_P of a point P involves the computation of the ratio between two distances: 1) the distance d from the origin (midpoint between the ear landmarks) to the surface point P on one side of the midsagittal

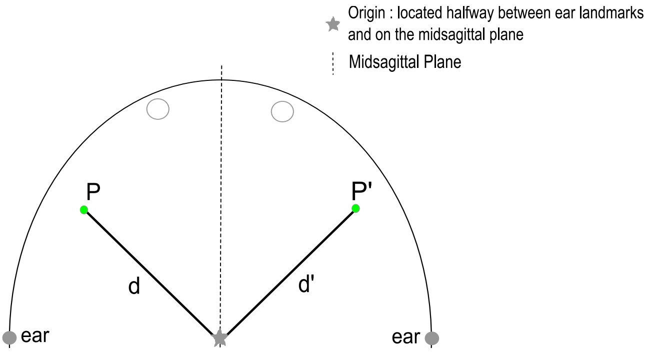

Figure 10.2: Computation of the asymmetry: Illustration of the distances d and d' between the origin and the points P and P', respectively, in an axial view.

plane, and 2) the distance d' from the origin to the corresponding point P' on the other side of the midsagittal plane (Figure 10.2).

Since, intuitively, the amount of asymmetry at P and P' should be equal, except for a sign introduced in order to distinguish a point in a "bulged" area from a point in a "flattened" area, A_P and $A_{P'}$ are defined by:

$$\text{if } d > d' \text{ then } A_P = 1 - (\frac{d'}{d}) \text{ and } A_{P'} = -A_P \tag{10.1}$$

$$\text{if } d' > d \text{ then } A_{P'} = 1 - (\frac{d}{d'}) \text{ and } A_P = -A_{P'} \tag{10.2}$$

The change in head asymmetry is calculated as the difference between the asymmetry absolute values at the two stages (before and after treatment):

$$\text{Change} = |A_{P,\text{stage1}}| - |A_{P,\text{stage2}}| \tag{10.3}$$

Hence, a positive change (improvement) implies that $A_{P,\text{stage2}}$ is closer to 0 than $A_{P,\text{stage1}}$ (i.e., closer to perfect symmetry).

10.3.3 Modelling Asymmetry using Principal Components Analysis

PCA is a popular method for shape modelling (an excellent description is found in [202]). The PCA is performed as an eigenanalysis of the covariance matrix of the (aligned) asymmetry measures.

The asymmetry values for each scan are ordered according to the mesh points of the template scan (cf. section 3.1.) and stored in a vector of size M:

$$\mathbf{a} = [|A_{P1}|\,,\, |A_{P2}|\,,\, \dots\,,\, |A_{PM/2}|\,,\, |A_{P'1}|\,,\, |A_{P'2}|\,,\, \dots\,,\, |A_{P'M/2}|] \tag{10.4}$$

Here the first and last $M/2$ elements are asymmetry values for the points on the right and left sides of the midsagittal plane, respectively. The maximum-likelihood estimate of the covariance matrix can be written as:

$$\mathbf{\Sigma}_a \;=\; \frac{1}{N}\sum_{i=1}^{N}(\mathbf{a}_i - \bar{\mathbf{a}}_i)\,(\mathbf{a}_i - \bar{\mathbf{a}}_i)^{\mathrm{T}} \;=\; \frac{1}{N}\,\mathbf{A}\,\mathbf{A}^{\mathrm{T}} \tag{10.5}$$

where $\bar{\mathbf{a}}$ is the maximum-likelihood estimate of the mean asymmetry of the N data-vectors. The principal axes of the M-dimensional point cloud of asymmetry are now given as eigenvectors, $\mathbf{\Phi}_a$, of the covariance matrix:

$$\mathbf{\Sigma}_a\,\mathbf{\Phi}_a = \mathbf{\Phi}_a\,\mathbf{\Lambda}_a \tag{10.6}$$

where $\mathbf{\Lambda}_a$ is a diagonal matrix containing the eigenvalues of the covariance matrix, and the columns of $\mathbf{\Phi}_a$ contain its eigenvectors. An asymmetry instance can be generated by modifying the mean asymmetry by adding a linear combination of eigenvectors:

$$\mathbf{a} = \bar{\mathbf{a}} + \mathbf{\Phi}_a\,\mathbf{b}_a \tag{10.7}$$

where $\mathbf{b}_a$ is a matrix containing the asymmetry model parameters.

As the number of observations ($N = 76$ scans) is much smaller than the number of surface points ($M = 190076$), the eigenanalysis is carried out using a reduced covariance matrix:

$$\mathbf{\Sigma}_{reduc} = \frac{1}{N}\,\mathbf{A}^{\mathrm{T}}\mathbf{A} \tag{10.8}$$

The eigenanalysis of this matrix gives the eigenvalues and eigenvectors of the covariance matrix. The eigenvalues and the eigenvectors may then be computed by:

$$\mathbf{\Lambda}_a = \mathbf{\Lambda}_{reduc} \tag{10.9}$$

$$\mathbf{\Phi}_a = \mathbf{A}\,\mathbf{\Phi}_{reduc} \tag{10.10}$$

In practice, the eigenanalysis may be carried out by Singular Value Decomposition (SVD).

10.3.4 Projection of 3D Surfaces into 2D Flat Maps

A more compact means of presentation is to construct a flat map (Figure 10.3b) by a simple transformation from rectangular to spherical coordinates. The flat

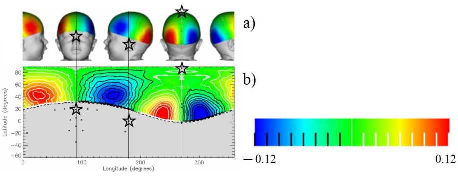

Figure 10.3: Flat map construction. a) Asymmetry values in an example subject shown as color coding. b) Corresponding flat map with contours (black: negative, white: positive). Some landmarks are shown as star symbols. Lower limit of helmet region is shown as dashed curve.

map has right ear landmark at longitude = 0 degrees, midface at 90 degrees, left ear landmark at 180 degrees and center of the back of the head at 270 degrees. Regions below the helmet area are shown in light gray, below the dashed curve. Levels of asymmetry are indicated by contours in the flatmap. There are 16 contour intervals, spanning the range of asymmetry as indicated by the color bar. The contours are equidistant in terms of asymmetry and are drawn in black for negative values, and in white for positive values. Hence, black contours show "bulged" areas (negative), white contours "flattened" areas (positive), and areas exhibiting no asymmetry are displayed in light gray.

10.4 Results

10.4.1 Asymmetry

Figure 10.4 presents the results of the asymmetry computations in three example subjects. Top views of the head before (a) and after (b) treatment are shown together with corresponding asymmetry flat maps. In addition, a map of change (c) is shown.
Figure 10.4.1. shows an asymmetric DP patient with right-sided flattening posteriorly, as well as a left-sided flattening anteriorly (a). The typical parallelogram shape is also reflected in the asymmetry flat map. Note the improvement in asymmetry after treatment (b,c).
Figure 10.4.2. shows a typical brachycephalic patient (a). Brachycephalic patients are generally not very asymmetric, as their deformation mainly causes a foreshortening of the skull. Note improved shape after treatment (b,c).
The third patient, Figure 10.4.3, has left-sided flattening posteriorly as well as a right-sided flattening anteriorly (a). Note the improvement after treatment (b,c).

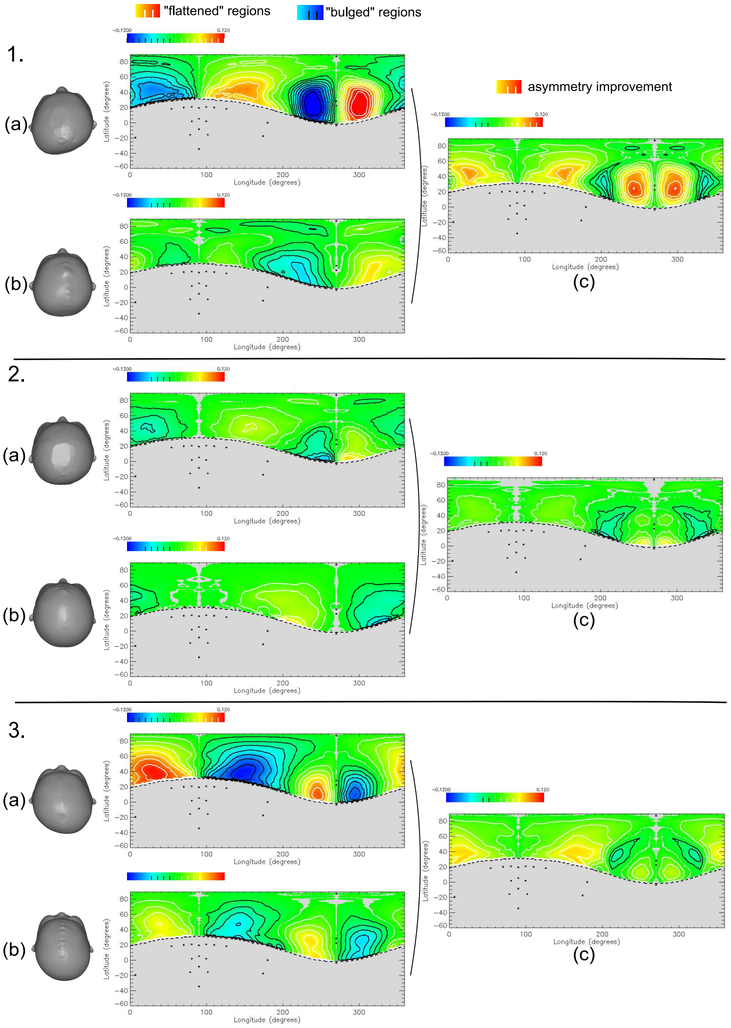

Figure 10.4: Results of the asymmetry computation and changes for: 1. Right-sided flattening posteriorly and left-sided flattening anteriorly. 2. Brachycephaly. 3. Left-sided flattening posteriorly and right-sided flattening anteriorly. (a) Scans at stage 1. (b) Scans at stage 2. (c) Changes between the two stages. In the flat maps showing asymmetry (middle column), positive and negative values denote ”flattening” and ”bulging” respectively. In the flat maps of change, positive values denote improvement.

10.4.2 Statistical Model

A statistical model was created by performing PCA on the 76 scans. The input of the PCA was the vector of asymmetry measures at each point in the helmet region. The decay of eigenvalues (Figure 10.5a) indicates that 96 % of the asymmetry variation can be modelled using the first eight parameters. The mean asymmetry (Figure 10.5b) emphasizes posterior and anterior regions with high asymmetry, while the anterior parts exhibit smaller magnitude.

Figure 10.5(c-j) displays the first eight modes showing only $\mathbf{\Phi b}_a$ (cf. Equation 10.7) with $\mathbf{b}_a = -3$ standard deviations. As the images corresponding to $\mathbf{b}_a = +3$ standard deviations are exactly the same as $\mathbf{b}_a = -3$ standard deviations but with opposite colors, they are not displayed. The first mode (c) localized the main asymmetry variation to the posterior region of the head. The second mode (d) represents variations occurring in the anterior region of the head, but spatially more spread out than the posterior region. The variations of the third mode occurred above the ears, also seen in Figure 10.4c. Modes four (f) and five (g) revealed variability mainly in the posterior area of the head, probably the result of variation in the location of the affected area posteriorly. In general, higher modes represented higher spatial frequencies of variation.

The scores of the three first modes (Figure 10.6) demonstrate the direction and amount of asymmetry progress for each individual. In Figure 10.6a, the scores for PC2 are plotted against the scores for PC1. The amount of posterior and anterior asymmetry may be read off the x- and y-axes, respectively. The least amount of asymmetry is found in the upper-left corner of this figure. This is the region where good treatment outcomes are located, as well as the brachycephalic heads. Individuals that improve in terms of posterior asymmetry move leftwards in the diagram, whereas individuals that improve in terms of anterior asymmetry move upward. Analogously, in Figure 10.6b, individuals that improve in terms of asymmetry above the ear move downward.

10.4.3 Validation of the Asymmetry Model

The usefulness of the asymmetry model depends on its ability to capture and describe clinically relevant information in a compact way. Two of the most important parameters describing head asymmetry in DP could be stated as “magnitude of posterior asymmetry” and “magnitude of anterior asymmetry”. In the previous section there was strong evidence that the first two modes were related to these particular clinical parameters. To check the strength of the relation between the model modes and the clinical parameters, a search for local extrema of asymmetry was conducted in the asymmetry flat maps. Figure 10.7 shows the correlation between scores and local minima.

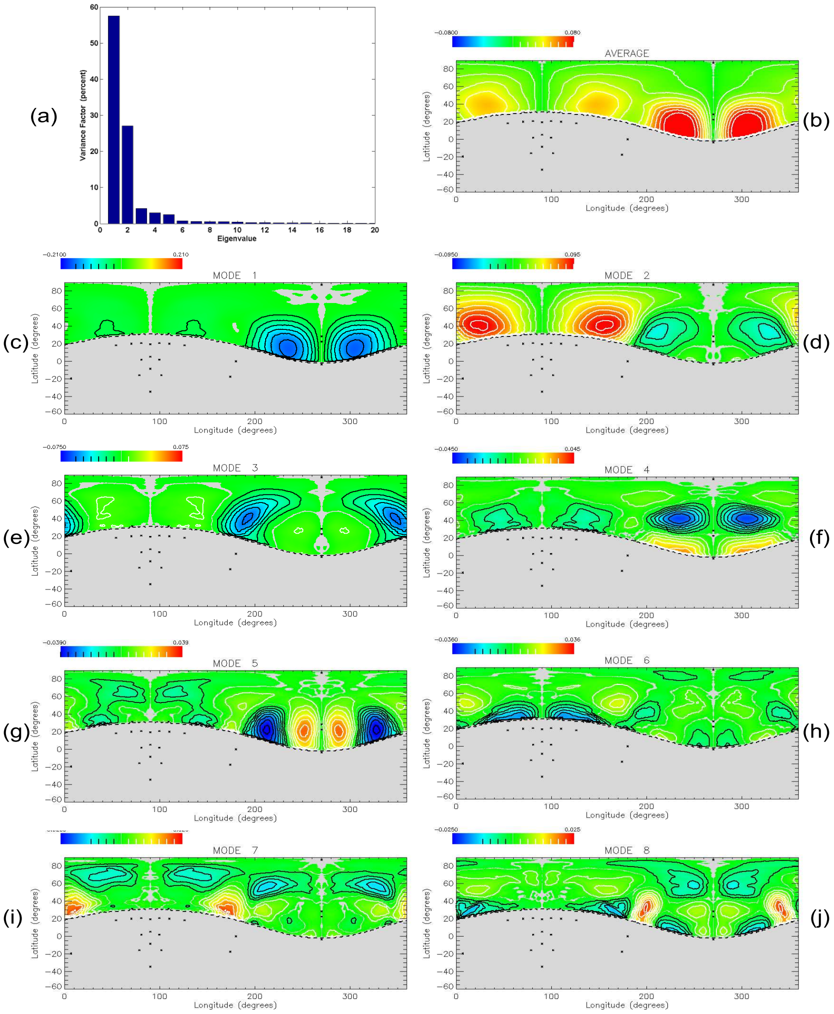

Figure 10.5: Presentation of the asymmetry model. (a) Eigenvalues (as percentage of the total variation). (b) Mean asymmetry. (c)–(j) Modes 1 to 8. Modes are shown as variation at −3 standard deviations from the mean. Within the same mode, regions displayed with opposite contour colors (black and white) vary in opposite directions.

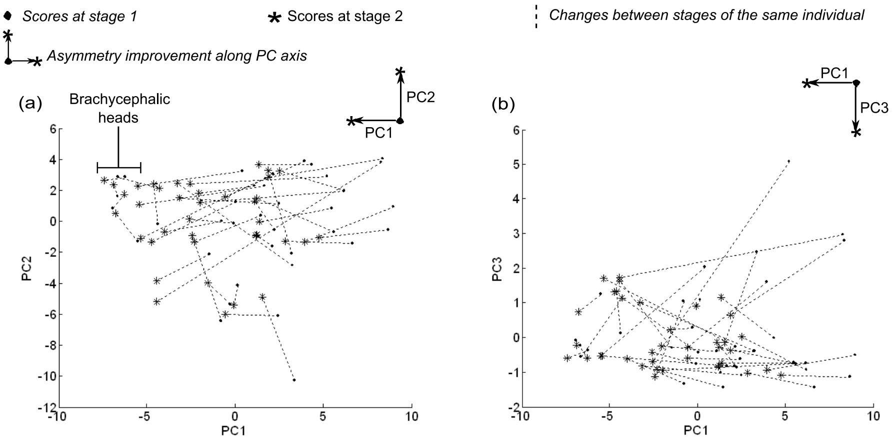

Figure 10.6: Score plots of the asymmetry model: (a) PC2 vs. PC1. (b) PC3 vs. PC1.

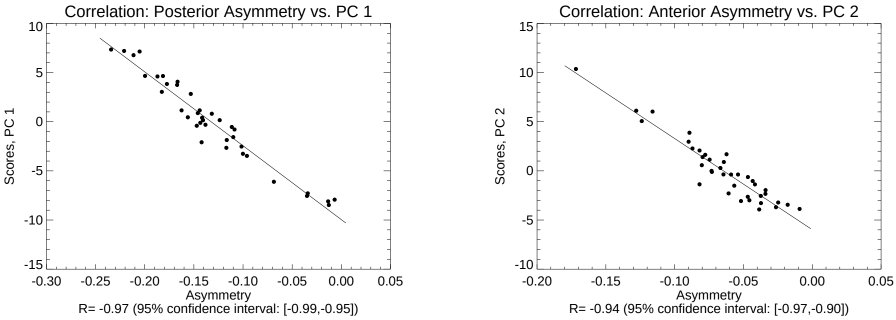

Figure 10.7: Correlation between clinical parameters and model PC scores.

10.5 Discussion

The computed asymmetry corresponded well (Figure 10.4) to observed asymmetry in the scans. Limitations of the method of establishing point correspondence between scans were the use of the ears (that are often affected in DP) for the registration, and the use of constructed landmarks instead of anatomical landmarks on top of the head. None of these limitations seem to have severely affected a valid asymmetry measurement. PCA is often used for summarizing data. The new variables created by PCA, however, are not guaranteed to be interpretable. The success of the asymmetry model (Figure 10.7) could be due to the less complex, "global" types of asymmetry variation present in the DP dataset. The excellent properties of the model makes using the model attractive compared to other methods of asymmetry assessment. Other methods, as direct anthropometry of the head [e.g. 113], measurement systems using a head ring or strip [e.g. 27, 228], or even measurements on 3D scans [e.g. 176], produce a multitude of parameters, making the interpretation difficult in terms of asymmetry and less intuitive. Contrary to [128] and [16], which use a sparse set of inter-landmark distances, computing the asymmetry at every surface point provides the opportunity to create a high spatial resolution asymmetry model.

10.6 Conclusion

A new 3D asymmetry measure was developed, providing a detailed surface map of asymmetry covering the whole head. The asymmetry measure was seen to reflect observed asymmetry in DP very well. A statistical model was created by performing PCA on the asymmetry maps in 38 patients. PCA modes were seen to correspond very well to clinically relevant parameters. In particular, the first and second modes corresponded to variation at the back and front of the head, respectively. The method is suitable for monitoring asymmetry treatment in individuals, as well as for classifying asymmetry in population studies.

10.7 Acknowledgements

SL acknowledges the BIOP graduate school for financial support.

CHAPTER 11

A Volumetric Quantification of Asymmetry Using Non-rigid Registration

---

Hildur Ólafsdóttir, Tron A. Darvann, Stéphanie Lanche, Nuno V. Hermann, Karl Sjöstrand, Estanislao Oubel, Alejandro F. Frangi, Per Larsen, Chad A. Perlyn, Daniel Govier, Hanne Dahlgaard Hove, Jyri Hukki, Alex A. Kane, Gillian M. Morriss-Kay, Sven Kreiborg, Bjarne K. Ersbøll, Rasmus Larsen

Abstract

This paper presents a volumetric measure of asymmetry. The measure is derived from the deformation fields acquired by non-rigid registration of a patient volume to a symmetric reference volume. Compared to related methods, the main advantage of the proposed approach is that it is free of defining the mid-sagittal plane in every subject. The proposed measure is evaluated using representative data for two different craniofacial anomalies, Crouzon syndrome in mice, and human unicoronal synostosis (UCS). Example results for individuals are presented along with mean group asymmetries. Using multiple hypothesis testing, point-wise significance maps are derived. This shows that Crouzon mice are significantly more asymmetric than controls in the regions of the nose, zygoma, and posterior skull. Furthermore, children with UCS are significantly more asymmetric than normal children in the mid-face, posterior skull and anterior cranial fossa. The image registrations are validated by determination of point to surface errors. The average registration accuracy is 0.83-1.72 mm for the UCS dataset. For the Crouzon data the average accuracy is 0.041-0.047 mm. The asymmetry measure is validated by a comparison to a visual rating by a clinical expert for the Crouzon mouse application, revealing a sensitivity of 66% and specificity of 95%.

11.1 Introduction

In biology, symmetry refers to a balanced distribution of duplicate body parts or shapes. The body of most organisms exhibits some type and amount of symmetry. The human body reveals an organization according to a bilateral symmetry; the vertical plane passing through the middle, the midsagittal plane (MSP), divides the body into right and left, mirrored halves. Asymmetry may be defined as the difference or the lack of symmetry between these halves.

The skull of the newborn child is composed of a collection of bone plates connected with wide growth zones (consisting mainly of connective tissue), which are often referred to as sutures. Growth perpendicular to these sutures permits the rapid expansion of the neural mass which occurs especially during the first two years of life. Figure 11.1 shows a schematic drawing of the sutures in an infant's skull. To further facilitate the discussion in the remainder of this paper, Figures 11.2 and 11.3 show the main regions of the skull of a human and a mouse, respectively.

Conditions involving disturbances in the development of the cranium and facial skeleton are often referred to as craniofacial anomalies. Asymmetry is an im-

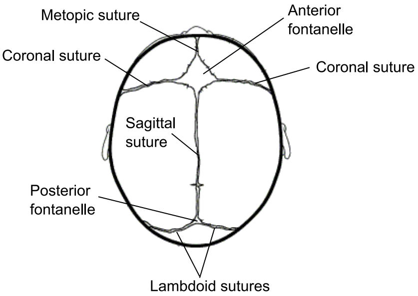

Figure 11.1: Schematic drawing of a normal child's skull, seen from above.

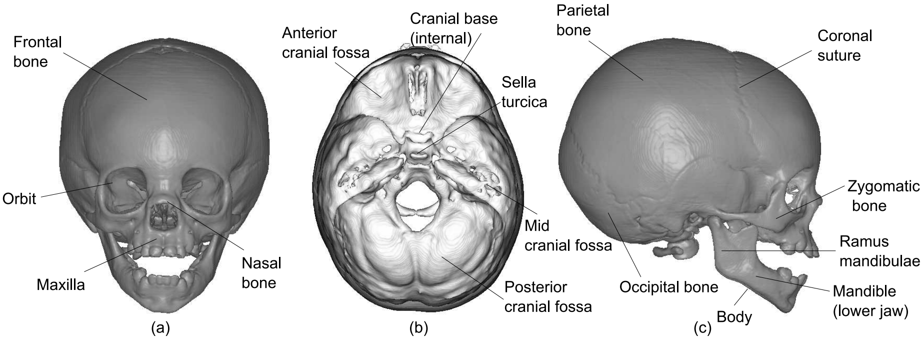

Figure 11.2: The normal human skull at approximately eighteen months of age. A surface representation of one of the CT scans used in the paper. (a) Frontal view, (b) Cut, top view, (c) Right lateral view.

portant measure for diagnosing and evaluating severity of the anomaly, as well as for evaluating the outcome of treatment.

Estimation of asymmetry from images may be divided into two types. *Structural asymmetry* deals with the asymmetry of the shape of the organ or body part of interest while *radiometric asymmetry* concerns the dissimilarity of the corresponding voxel intensities on each side of the symmetry plane. Structural asymmetry is of primary interest for craniofacial applications while radiometric asymmetry is of additional interest for e.g. brain studies.

This paper presents a novel approach for volumetric quantification of asymmetry. The approach taken is to create a symmetric reference volume and subsequently registering the volume of interest to this reference. Having established a left/right correspondence in each subject volume, it is now possible to assess both types of asymmetries. The main focus of this paper will, however, be on structural asymmetry. A volumetric measure of structural asymmetry

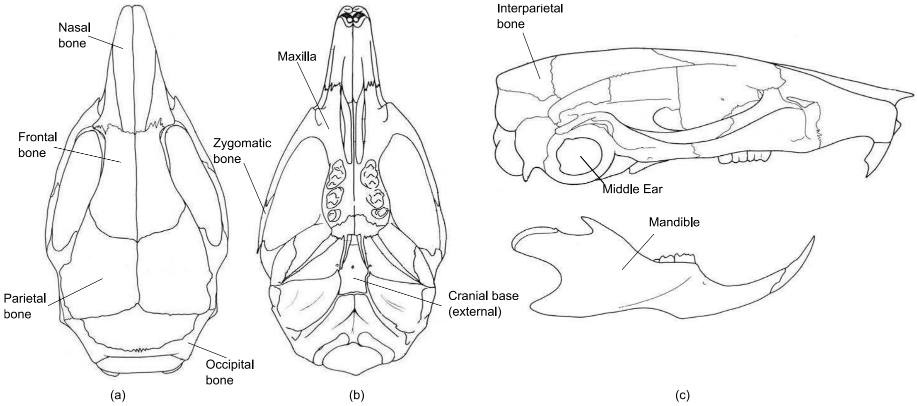

Figure 11.3: Schematic drawing of a normal mouse skull. (a) Top view, (b) Basal view, (c) Right lateral view. From [38]

is obtained by a comparison of the resulting left and right side displacement vectors. Using the proposed approach, asymmetry is quantified in two different craniofacial anomalies; Crouzon syndrome, using a mouse model, and unicoronal synostosis (UCS) in human data. This paper is an extension of our previous papers [121, 164]. In [164], the approach from [121] was improved by using deformation vectors instead of distances of deformed surface points to a fixed midpoint. Compared to [164], the asymmetry measure in the present study is extended from a surface-based measure to a full volumetric measure. Further, the paper introduces the decomposition of the asymmetry vector into its individual x-, y-, and z-components for more complete clinical interpretations and it includes point-wise estimates of statistical significance. Finally, the measure is evaluated in an additional application, namely the quantification of asymmetry in a group of infants with UCS.

11.1.1 Related Work

Many approaches for estimating radiometric asymmetry exist, especially in the brain literature (see an extensive review of asymmetry studies in brain image analysis in [222]). The following overview is limited to the discussion of existing approaches for estimating structural asymmetry.

The simplest forms of determining structural head asymmetry include direct anthropometry of the head, [e.g. 95, 113] or manual measurements on 3D scans, [e.g. 176]. Using image data, some authors have defined asymmetry with respect to a sparse set of inter-landmark distances [16, 128]. Methods providing denser measurements are provided in a few papers. In [32], deviation of the midsagittal surface with respect to the midsagittal plane was assessed, and in a previous study of ours, asymmetry in children with deformational plagiocephaly was measured. Here, the ratio of left and right distances to a midpoint of a deformed symmetric template was used to define the asymmetry [121].

The estimation of structural asymmetry has received some attention in the field of brain image analysis. In [8], asymmetry was defined by dividing the registration coefficients, obtained from a registration to a symmetric template, into symmetric and asymmetric before applying a Principal Components Analysis (PCA). In [120] structural asymmetry was defined by warping group-representative left and right hemispheric images to each other. In [232], hippocampal asymmetry was studied by analysing deformation fields from left to right halves. Hippocampal asymmetry was also the subject of [208, 209], where thickness measures from medial representations were applied. In [105], voxel-wise structural and radiometric asymmetry was assessed in tumour brain images by defining a symmetry plane in each image and registering to the reflection and in [66] asymmetry was estimated from brain variability maps from sulcal lines registration.

This paper introduces a novel asymmetry measure based on the deformation vectors resulting from non-rigid registration of a given subject image to a perfectly symmetric atlas image. The relationship between the corresponding vectors on the left and right side of the mid-sagittal plane is used to define the asymmetry. The main advantage of the proposed method, compared to most of the above mentioned approaches, is that it avoids defining a symmetry plane in each subject. This is important since defining such a symmetry plane in a skull affected by malformation is prone to errors.

11.1.2 Clinical Applications

Craniosynostosis involves the premature closing of one or more of the cranial sutures. This results in a disturbed brain growth and abnormal head shape. Craniosynostosis can be divided into two groups, syndromic and non-syndromic craniosynostosis. The present study will deal with examples from both groups, Crouzon syndrome and unicoronal synostosis.

Crouzon syndrome was first described nearly a century ago when calvarial and facial anomalies, and abnormal protrusion of the eyeballs were reported in a mother and her son [43]. Later, the condition was characterised as a constellation of premature fusion of the cranial sutures (craniosynostosis), orbital deformity, maxillary hypoplasia, beaked nose, crowding of teeth, and high arched or cleft palate. The fusion of the sutures at different time points and on different sides of the skull leads to asymmetric head shape. Heterozygous mutations in the gene encoding *fibroblast growth factor receptor type 2* (*FGFR2*) have been found responsible for Crouzon syndrome [180]. Recently a mouse model was created to study one of these mutations ($FGFR2^{Cys342Tyr}$)[63] and applying advanced small animal imaging techniques such as Micro CT, a detailed examination of the craniofacial growth disturbances is allowed.

Unicoronal synostosis is defined by the premature closure of one of the coronal sutures. This may result in a highly asymmetric head shape, growth disturbances, increased intracranial pressure and developmental delays. During treatment, one or more surgeries are carried out and a CT scan is usually required. Typically, the scans are qualitatively inspected with respect to head shape and symmetry, and the state (patent or fused) of the coronal suture is assessed.

Asymmetry is highly relevant for both syndromic and non-syndromic craniosynostosis. Firstly, it is interesting to study which regions of the head are asymmetric and how this is related to the suture fusion. Secondly, an accurate and localised assessment of asymmetry will improve surgery planning and treatment evaluation of children with craniosynostosis and other related diseases.

Asymmetry in UCS patients has been previously investigated in a few studies using reference points or visual inspection. The main findings include asymmetry in the anterior and middle cranial fossae [22, 75, 114, 136, 142, 149], the orbital region [24, 114, 135, 142, 149] and the mandible [109, 114, 142, 149]. In [149], more landmarks were used, compared to previous studies, and asymmetries were additionally reported in the maxilla, zygomatic bone and parietal bone.

We found one study concerning asymmetry in Crouzon patients, concluding that one out of 19 Crouzon patients had asymmetric cranial base [115].

11.2 Methods

11.2.1 Creation of a Symmetric Template Volume

The proposed method is based on the registration of a subject of interest to a symmetric template volume. The template volume is created preferably from a shape- and intensity-based atlas of normal subjects (see e.g. [187],[106]), otherwise from a selected representative image. The key point is that it is fully symmetric. The symmetric property is obtained by defining the mid-sagittal plane, e.g. by the average of ear landmarks. Subsequently, one half of the image is reflected across the plane. The resulting image is the perfectly symmetric volume, where each voxel on the right side has a corresponding voxel on the left side.

11.2.2 B-spline-based Non-rigid Registration

To create a left/right correspondence for all subject images, all subject images are matched to the anatomy of the symmetric reference image. A widely used non-rigid registration algorithm based on B-splines [185, 188] is applied in this study. This algorithm uses a transformation model which is a combination of global and local transformations. The global transformation model consists in our case of an affine transformation model with either 7 or 9 degrees of freedom depending on the application. The more interesting local transformation model describing the non-rigid part of the model is described by a free-form deformation model. This is defined by an $p_x \times p_y \times p_z$ mesh of control points $\mathbf{c}$ with spacing $(\delta_x, \delta_y, \delta_z)$. The underlying image is then deformed by manipulating the mesh. The model is written as the tensor product of 1D cubic B-splines,

$$\mathbf{T}_{local}(x, y, z) = \sum_{l=0}^{3} \sum_{m=0}^{3} \sum_{n=0}^{3} B_l(u) B_m(v) B_n(w) \mathbf{c}_{i+l,j+m,k+n} \tag{11.1}$$

where B_0 to B_3 are the pre-defined basis functions of the B-spline, i, j and k are control point indices and u, v and w are (x, y, z) image coordinates translated into the lattice coordinates.

11.2.3 Volumetric Quantification of Asymmetry

For asymmetry calculations, only the local displacements are considered, in order to make the measure insensitive to pose and scale differences. From the non-rigid registration, asymmetry can be calculated at any point in the deformed symmetric atlas.

The basic idea of the proposed asymmetry measure is to compare a displacement vector on one side to the corresponding displacement vector on the other side. More formally, asymmetry, A_L, of a point L on the left side involves the comparison of the local displacement vector, $\mathbf{dL}$ in point L and the corresponding vector, $\mathbf{dR}$ in point R on the right side. Since the task is to quantify bilateral asymmetry, one of the vectors is mirrored across the midsagittal plane,

$$\mathbf{dR}^m(x, y, z) = \mathbf{dR}(-x, y, z).$$

Now the asymmetry vector may be defined by the difference vector between the two vectors and an absolute value of asymmetry is defined by the magnitude of the asymmetry vector,

$$\begin{aligned} \mathbf{a_L} &= \mathbf{dL} - \mathbf{dR}^m \\ |A_L| &= ||\mathbf{a_L}||. \end{aligned} \tag{11.2}$$

This, obviously gives $A_L = 0$ if the left and right displacement vectors are perfectly symmetric. Figure 11.4 illustrates the vectors involved in the calculation of the asymmetry measure.

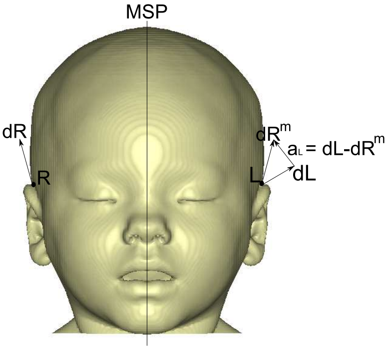

Figure 11.4: Schematic figure of vectors involved in asymmetry calculation. Corresponding displacement vectors in points L and R, on the left ($\mathbf{dL}$) and right side ($\mathbf{dR}$) shown on the symmetric template surface. $\mathbf{dR}^m$ denotes the mirrored version of $\mathbf{dR}$. The asymmetry vector is the difference vector, $\mathbf{a_L} = \mathbf{dL} - \mathbf{dR}^m$. The magnitude of the asymmetry vector defines the absolute asymmetry, $|A_L|$.

Mirroring $\mathbf{dL}$ instead of $\mathbf{dR}$ would give $\mathbf{a}_R = \mathbf{dR} - \mathbf{dL}^m$. Obviously, $|A_R| = ||\mathbf{a}_R|| = |A_L|$, i.e. absolute asymmetry in L is equal to the one in R. This is illustrated in Figure 11.5. However, in order to determine the direction of asymmetry, A_R and A_L are distinguished by a sign.

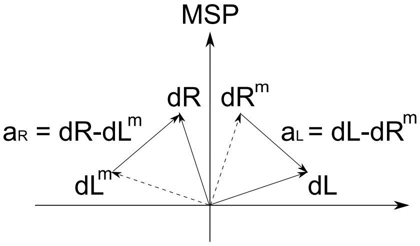

Figure 11.5: Illustration of $||a_R|| = ||a_L||$. Vectors involved in asymmetry calculation shown at the origin.

11.2.3.1 Determining the Direction of Asymmetry

We define the direction of asymmetry by a sign, indicating whether an expansion or contraction, with respect to the corresponding point on the other side, has occurred. Previously, we have used the surface normal vector to determine the sign [164]. In order to extend the surface-based measure to a volumetric measure, another approach is needed. Using the Jacobian as in many deformation studies [35, 132, 207, 221] is not suitable here since the information provided by the proposed asymmetry vector in point L, $\mathbf{a_L}$, on one hand, and the Jacobians of the deformations in points L and R, on the other hand, are very different. For example, a uniform displacement field across the MSP results in large values of A_i, as expected, while providing Jacobians close to 1. Using e.g. the difference between the corresponding left and right Jacobians to determine the sign of A_i would give inadequate information.

Instead, a more direct approach is taken where a comparison of the left and right distances to the midpoint (MP) is carried out. The midpoint is defined in the symmetric atlas as the average of ear landmarks. This is slightly related to our previous approach defining asymmetry as the ratio of distances to the midpoint [121]. Formally, we define

$$\begin{array}{ll} \text{if } ||(L+\mathbf{dL})-MP|| > ||(R+\mathbf{dR})-MP|| & \rightarrow A_L = ||\mathbf{dL}-\mathbf{dR}^m|| \\ \text{otherwise} & \rightarrow A_L = -||\mathbf{dL}-\mathbf{dR}^m||. \end{array} \tag{11.3}$$

The opposite sign is assigned to A_R,

$$A_R = -A_L. \tag{11.4}$$

The use of a reference point, such as the MP instead of using the distance to MSP ensures that all asymmetry components are taken into account when determining the sign (not only the transversal component).

A comparison of the MP-method and a Jacobian approach to determine the sign of asymmetry is provided by an example illustration in Figure 11.6.

Each component of the asymmetry vector may be visualised to give a more complete clinical interpretation. This means that transversal (x-component), sagittal (y-component) and vertical (z-component) asymmetry can be analysed separately. Determining a sign for each component is done by setting the other two components to zero in (11.3).

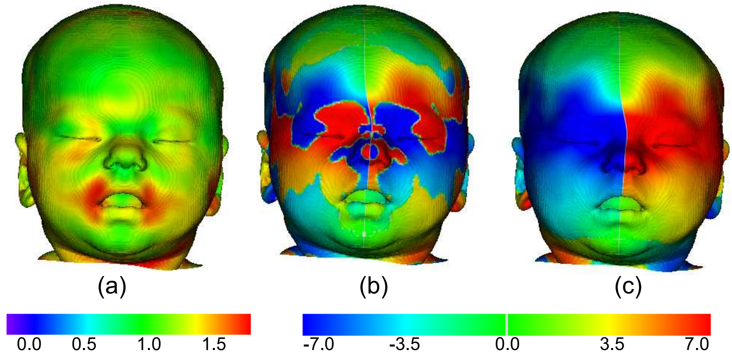

Figure 11.6: Determination of the sign of asymmetry comparing the use of Jacobians versus distance to midpoint. Illustration on an example case (a) Jacobians (det(Jac)) of deformation in each point visualised on the deformed symmetric surface. (b-c) Asymmetry (A_i) in each point of the deformed symmetric surface, where the sign is determined by (b) difference of Jacobians in corresponding left and right points, (c) distance to midpoint (MP). Note that where $|A_i|$ is large, as in the nose region, the Jacobians are close to 1, indicating uniform displacement fields. This leads to inaccurate determination of the sign of A_i in (b).

11.2.4 Testing for Significance

After estimating asymmetry in each point of a volume it is important to know whether or not the finding is significant. This is a non-trivial task due to the spatial correlation between points and the fact that multiple hypotheses tests need to be carried out simultaneously. Many authors have addressed this problem [8, 21, 62, 71, 150, 212]. We will follow the approach by Efron [62]. This approach aims at improving the estimation of false discovery rate (fdr) [12] by replacing the theoretical null-hypothesis by an estimated empirical null-hypothesis. Given (uncorrected) p-values at each point, their corresponding z-values are estimated,

$$z_i = \Phi^{-1}(p_i), \qquad i = 1, \dots M \tag{11.5}$$

where Φ is the standard normal cumulative distribution function and M is the number of points under consideration (i.e. all vertices of a surface or all voxels in an image). The theoretical null-hypothesis states that $z_i \sim N(0, 1)$. Now, local false discovery rate can be estimated at each point to distinguish “interesting” (significant) values from “uninteresting”. This is defined by

$$fdr(z) = f_0(z)/f(z) \tag{11.6}$$

where $f(z)$ is the value of the curve fitted to the z-histogram (including both classes, interesting and uninteresting) and $f_0(z)$ is the null-hypothesis density. Instead of using the theoretical null-hypothesis for $f_0(z)$, Efron proposed to use the empirical null-hypothesis, obtained by estimating the mean and standard deviation from $f(z)$. Now, the input values may be classified as interesting or uninteresting, by assigning a certain threshold to the fdr (Efron suggests that $fdr(z_i) \leq 0.10$ gives an interesting finding).

This simple methodology requires the estimation of a statistical distribution for the input data and corresponding p-values in each point. In the asymmetry case, we will use absolute asymmetry values and test for significance of difference in mean asymmetry in each point of group G1, compared to group G2.

$$\begin{aligned} H_{0,i} &: \bar{A_i}^{G1} = \bar{A_i}^{G2},\ i = 1, \ldots, M \\ H_{1,i} &: \bar{A_i}^{G1} \neq \bar{A_i}^{G2},\ i = 1, \ldots, M \end{aligned} \tag{11.7}$$

where

$$\bar{A_i}^{G1} = \frac{1}{N_{G1}} \sum_{j \in G1} A_i^j$$

is the mean asymmetry in point i across subjects j in group $G1$ and N_{G1} is the number of observations (subjects) in group $G1$. Since the absolute asymmetry values in the left half are equal to the corresponding values on the right half, we will only use one half when checking for significance.

Now we need to estimate the probability distribution of the asymmetry values. Assuming that the displacement vector components are normally distributed, it is noted that the squared magnitude of the asymmetry vector approximately follows a χ^2 distribution. The two vectors ($\mathbf{dL}$ and $\mathbf{dR}^m$) span a plane, which gives two degrees of freedom, i.e.

$$|A_i|^2 \sim \chi^2(2). \tag{11.8}$$

The significance of the differences between groups may now be estimated by an F-test, since the ratio of two χ^2 distributions follows an F-distribution. Now, the χ^2 distribution for each group is a sum of $\chi^2(2)$ distributions for each observation and the degrees of freedom is equal to the sum of degrees of freedom for the individual distributions,

$$\frac{|\bar{A_i}^{G1}|/(2N_{G1})}{|\bar{A_i}^{G2}|/(2N_{G2})} \sim F(2N_{G1}, 2N_{G2}).$$

By evaluating the F-statistic in each point of the surface or volume, p-values are obtained and inserted into (11.5) and (11.6).

11.3 Data Material

11.3.1 Crouzon Data

Micro-CT scans of **10** wild type and **10** $Fgfr2^{C342Y/+}$ mice were used in the study. Production of the $Fgfr2^{C342Y/+}$ and $Fgfr2^{C342Y/C342Y}$ mutant mouse (Crouzon mouse) was done as described in [63]. All procedures were carried out in agreement with the United Kingdom Animals (Scientific Procedures) Act, guidelines of the Home Office, and regulations of the University of Oxford. Images of the skulls were obtained at approximately 46μm × 46μm × 46μm resolution using a General Electric Medical Systems EVS-RS9 Micro-CT scanner. All mice were six weeks old (42 days).

11.3.2 UCS Data

20 CT scans of children with UCS were available resulting from a collaboration between three hospitals, Copenhagen University Hospital, Denmark; Helsinki University Central Hospital, Finland; and St. Louis Children's Hospital, MO, USA. The control group of 10 children stems from St. Louis Children's Hospital. The controls were suspected to have head injury after a fall or such, but were diagnosed as having no craniofacial anomaly. The data varied considerably in resolution and size, ranging from $0.3 \times 0.3 \times 0.6$ mm per voxel to $1 \times 1 \times 3$ mm pr. voxel. The age of the children at the time of scanning ranged from 2-20 months.

11.4 Experimental Results

The method was tested and validated on the two different craniofacial applications. For the Crouzon data, affine registration was performed using 9 degrees of freedom, involving anisotropic scaling since the main differences in the mouse skull were the height, width and length of the skull. This was followed by non-rigid registrations, which were run on resampled data, 0.2 mm pr. voxel and using a control point grid spacing of 3, 1.5, and .75 mm. The UCS data were treated similarly, except that the affine registration included 7 degrees of freedom (isotropic scaling) and the non-rigid registration was carried out using a resolution of 1 mm per voxel with control point spacing of 16, 8, and 4 mm.

11.4.1 Example Results

Figure 11.7 presents example results of the asymmetry computations for the Crouzon mouse application.

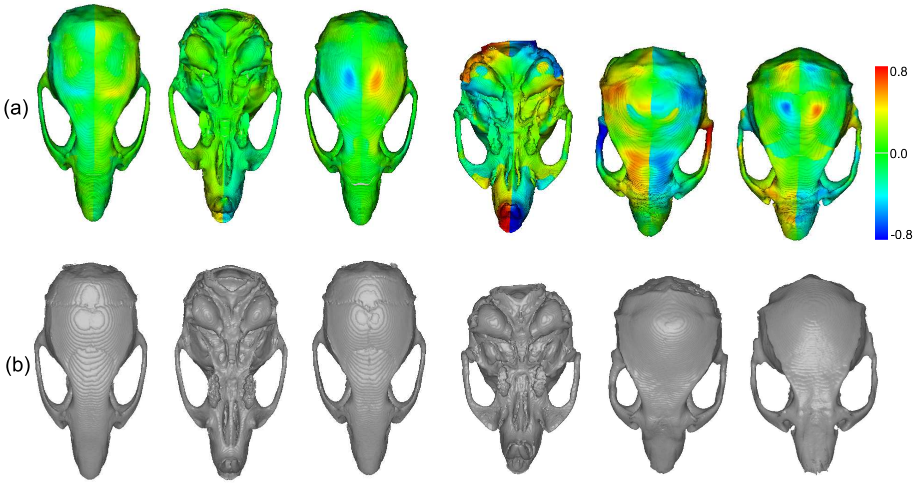

Figure 11.7: Example results for wild-type mice (first three columns) and Crouzon mice (last three columns). Row (a) Asymmetry values displayed on the deformed symmetric atlas, given in mm according to the colorscale. The scale ranges from blue (contracted) to red (expanded). Note that $A_R = -A_L$, i.e. each value on the left side has a corresponding negative value on the right side. (b) Original surfaces for comparison.

UCS asymmetry was calculated at both soft tissue and skull surfaces. Figures 11.8 and 11.9 give examples of soft-tissue asymmetries for two normal and two UCS cases. Figure 11.10 shows skull asymmetries for the same cases. In order to demonstrate the completeness of the asymmetry measure, each component of the asymmetry vector is shown (x,y,z), providing transversal, sagittal and vertical asymmetry, respectively.

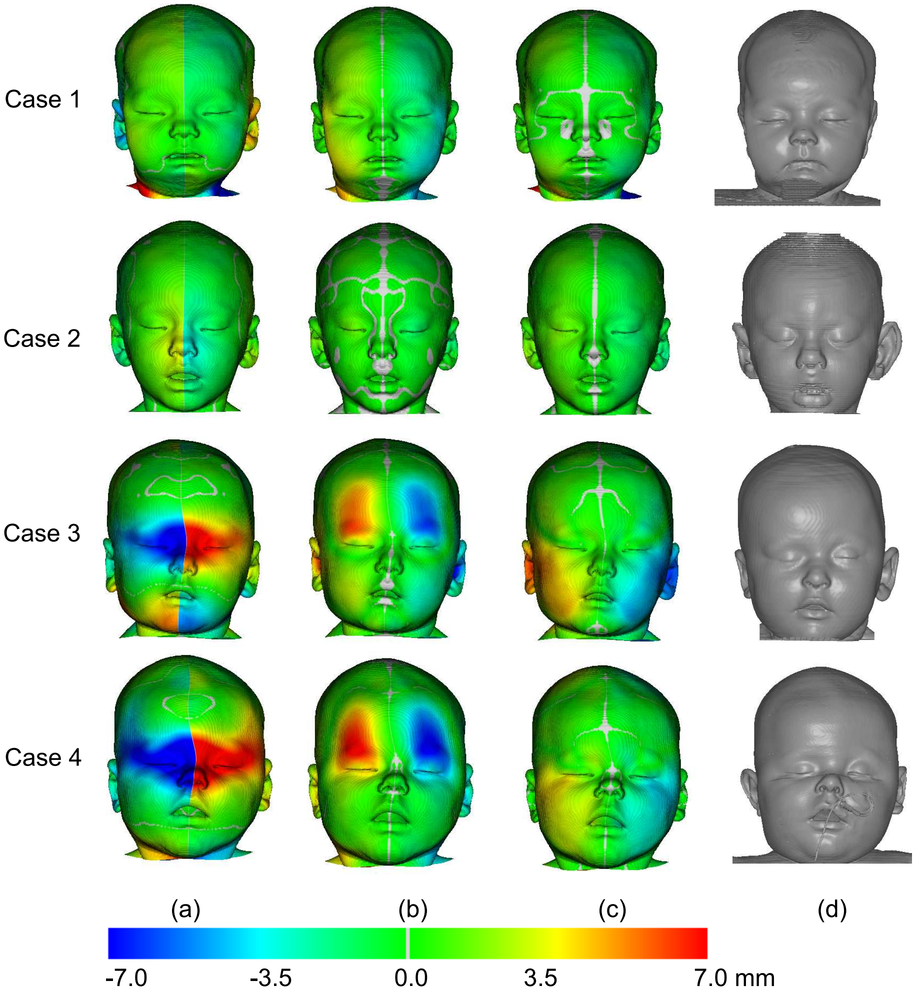

Figure 11.8: Example results for UCS data shown on the deformed symmetric soft-tissue surface in front view. First and second case are normal, third and fourth case have UCS. (a) Transversal, (b) sagittal and (c) vertical asymmetries are shown. (d) Original surfaces for comparison.

11.4.2 Group Comparison

Figure 11.11 provides a comparison of the groups of mice in terms of absolute mean asymmetry. To test if the groups are significantly different in each point, approximately 500,000 simultaneous hypotheses (each vertex from half of the surface) were evaluated according to the local fdr method discussed in

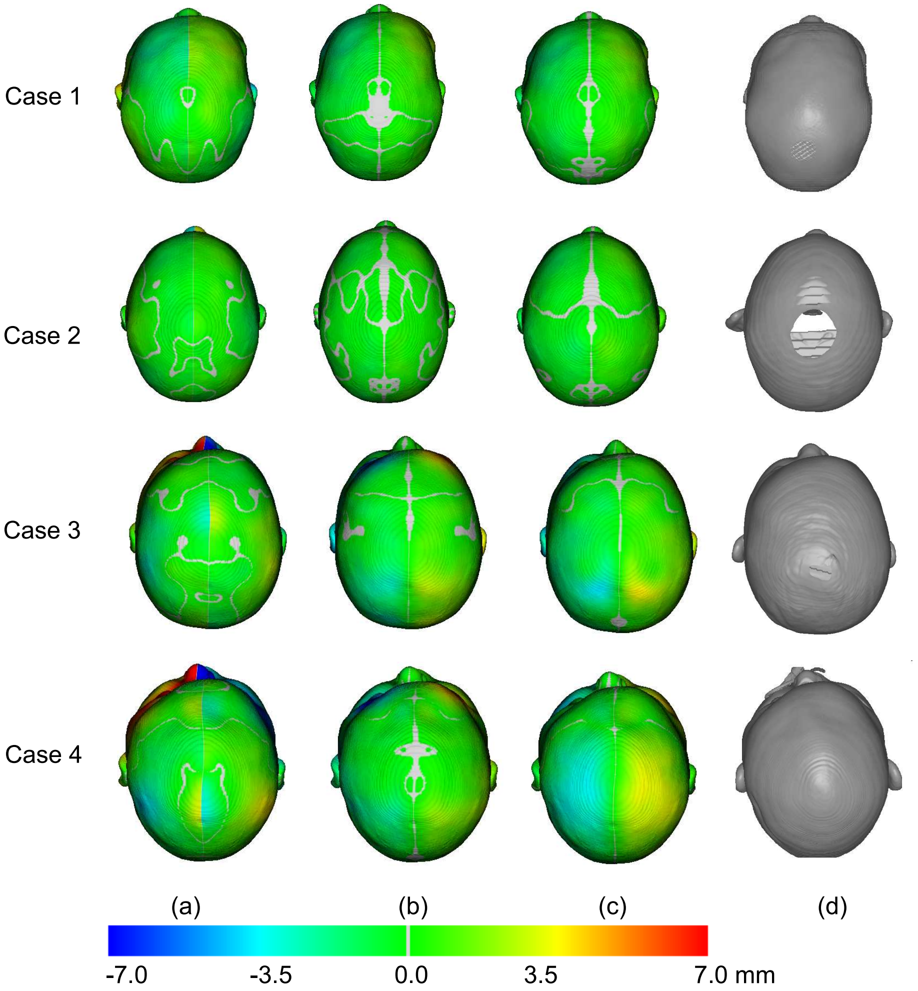

Figure 11.9: Example results for UCS data shown on the deformed symmetric soft-tissue surface in top view. First and second case are normal, third and fourth case have UCS. (a) Transversal, (b) sagittal and (c) vertical asymmetries are shown. (d) Original surfaces for comparison.

Section 11.2.4. The UCS data were treated similarly in Figure 11.12 except that group asymmetries are shown for both soft tissue and skull. To further investigate the asymmetry in a UCS skull, Figure 11.13 provides a similar demonstration for the total asymmetry in the cranial base.

To conclude the group comparison, Figure 11.14 provides box-and-whisker plots

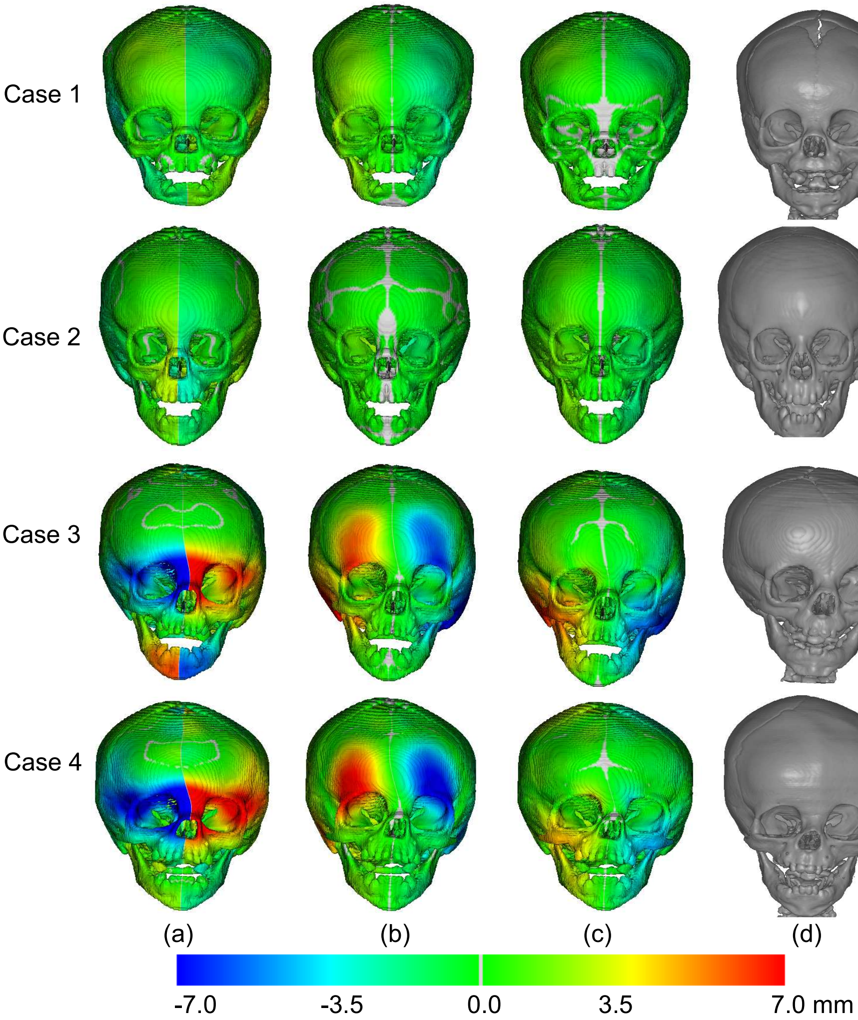

Figure 11.10: Example results for UCS data shown on the deformed symmetric skull surface in front view. First and second case are normal, third and fourth case have UCS. (a) Transversal, (b) sagittal and (c) vertical asymmetries are shown. (d) Original surfaces for comparison.

for group differences in mean absolute asymmetries for both applications.

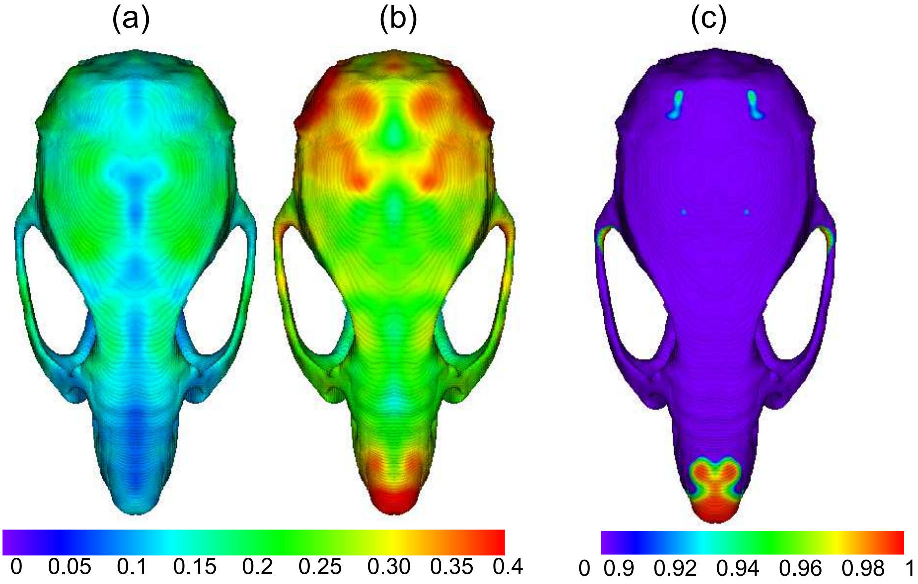

Figure 11.11: Difference between groups. Mean absolute asymmetry of (a) wild-type and (b) Crouzon mice, displayed on the symmetric atlas in top views. (c) Significance of group difference, given as 1-fdr.

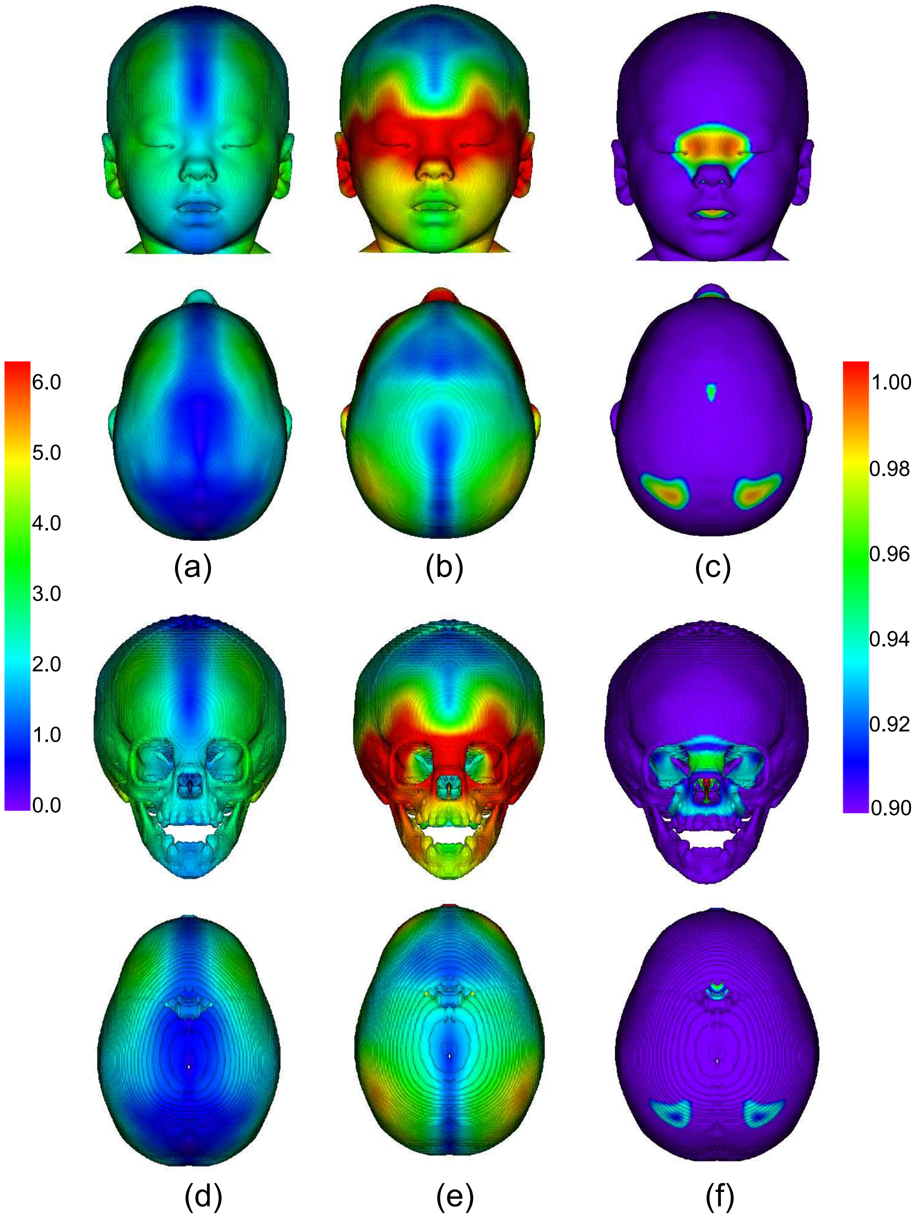

Figure 11.12: Group comparison of mean total asymmetries for the UCS study. (a-c) Soft tissue surfaces in front and top views. (d-e) Skull surfaces in front and top views. The surfaces are colored by (a,d) Mean normal absolute asymmetry in mm (left colorbar), (b,e) mean UCS absolute asymmetry in mm (left colorbar), (c,f) Significance of group difference, given as 1-fdr (right colorbar).

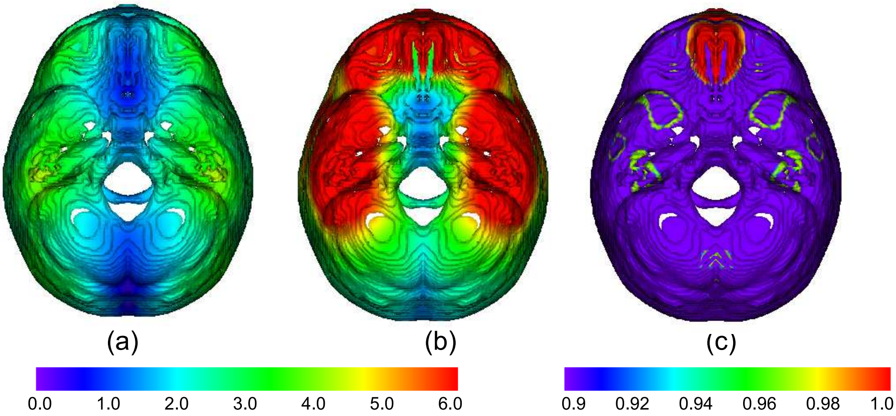

Figure 11.13: (a,b) Mean total asymmetries in the cranial base, given in mm: (a) Normal group, (b) UCS group, (c) Significance of differences, given as 1-fdr.

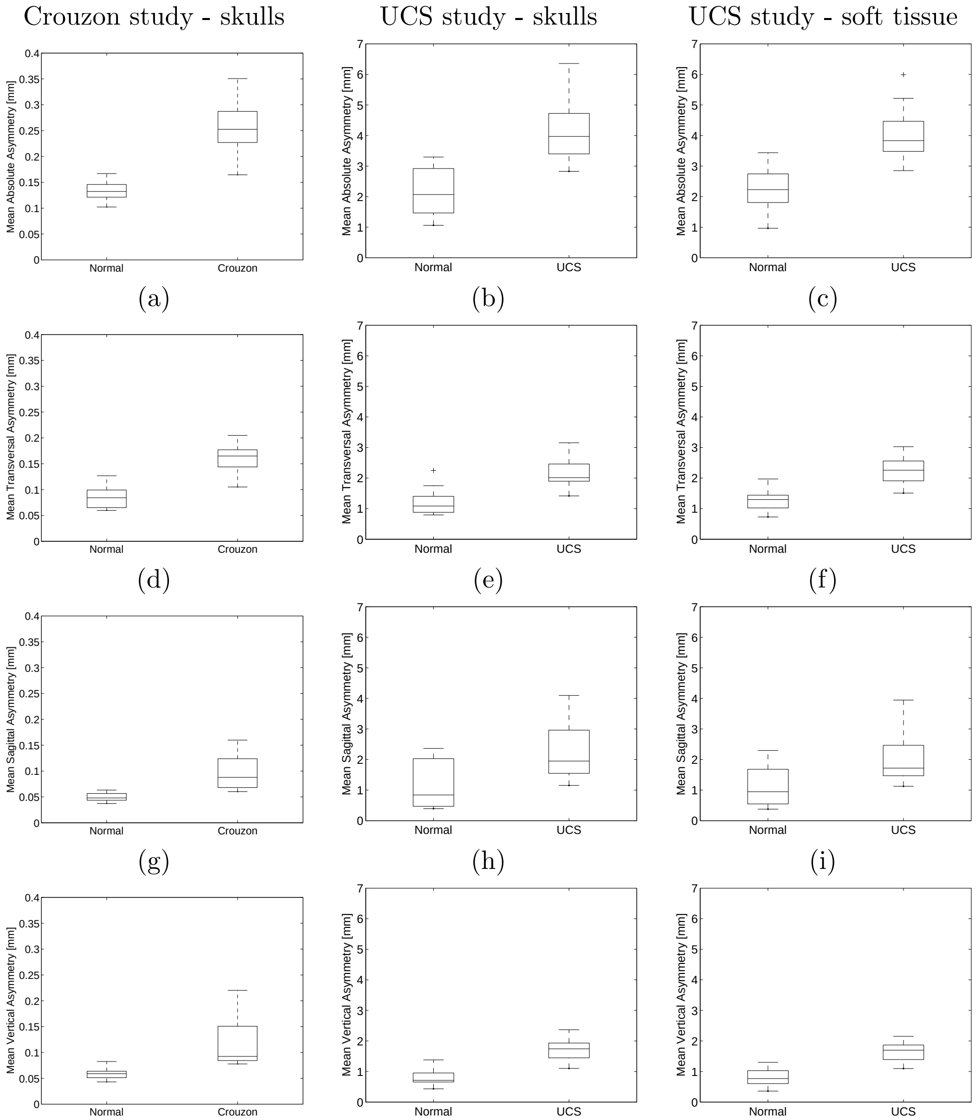

(a) (b) (c)

(d) (e) (f)

(g) (h) (i)

(j) (k) (l)

Figure 11.14: Group differences in asymmetry for Crouzon and UCS studies: (a-c) Total asymmetry, (d-f) transversal asymmetry (x), (g-i) sagittal asymmetry (y), (j-l) vertical asymmetry (z). (a,d,g,j) Crouzon skulls. (b,e,h,k) UCS skulls. (c,f,i,l) UCS soft tissue. $H_0 : \mu_{Crouzon} = \mu_{normal}$ and $H_0 : \mu_{UCS} = \mu_{normal}$ are rejected for all cases. Highest p-value: 0.002 for (h)

11.5 Validation

11.5.1 Registration Accuracy

Previously, we have evaluated landmark errors for the mouse registrations by estimating landmark positions automatically using the registration results and comparing to manual assessment. Statistical analysis showed that the automatic approach performed on equal terms with the inter-observer variability [162].

For this study, we estimated the accuracy by the point to surface distance, i.e. the distance from each point on the deformed atlas surface to the closest point on the original subject surface. For the mice, only the skull surface was investigated, since the soft tissue was not present. For the UCS data, both soft tissue and skull surface were evaluated. Table 11.1 summarises the results from this analysis.

Table 11.1: Point to surface errors for registration of both datasets. RMS errors are given in mm ± one standard deviation.

	Normal children	UCS children	Normal mice	Crouzon mice
Skull	0.84 ± 0.51	0.83 ± 0.43	0.041 ± 0.032	0.047 ± 0.032
Soft	1.72 ± 1.76	1.36 ± 1.34	–	–

A further analysis of these errors involved their position on the surfaces. Figure 11.15 shows the root-mean-square error, for normal and UCS data, displayed on the symmetric surface.

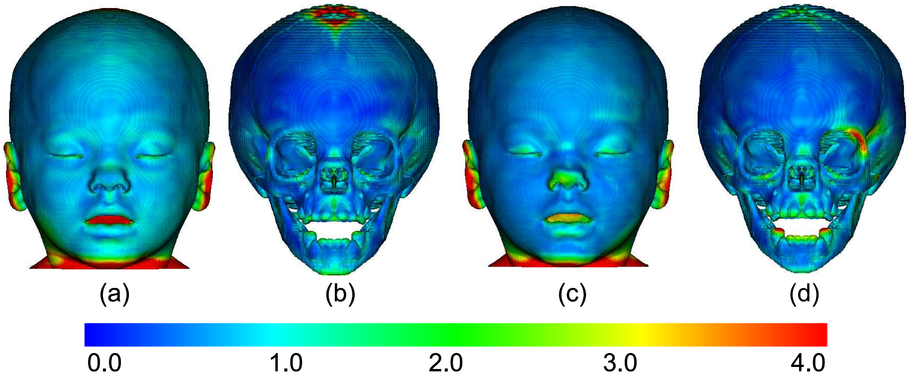

Figure 11.15: RMS errors in mm displayed in each point of the symmetric surface for (a) normal soft tissue, (b) normal skull, (c) UCS soft tissue, (d) UCS skull.

11.5.2 Clinical Expert Rating

The asymmetry measure was validated with respect to a clinical expert for the Crouzon mouse dataset. The expert rated nine different regions of anatomical interest on the skull of the original Crouzon surfaces. These were the nose (viewed from above and below), zygoma, anterior skull, mid skull, posterior skull, basal maxilla, anterior cranial base and posterior cranial base. The expert marked each region by 0 or 1 depending on whether the given region was symmetric or asymmetric, relatively. Similar ratings were obtained from the automatic method where regions with $|A_i| > 0.25$ mm were marked by 1 and the remaining regions by 0. Figure 11.16 gives the number of regions where the automatic approach and the expert rating agreed.

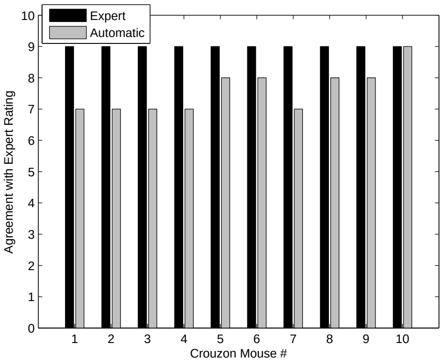

Figure 11.16: Validation with respect to expert rating. The gold standard is defined by the expert (black bars), who agrees with herself in rating of the nine regions for each mouse. The gray bars denote the number of regions where the automatic method agrees with the expert.

A further analysis of these results revealed a specificity of 66% and sensitivity of 95%.

11.6 Discussion

Judged from Figure 11.7, the three Crouzon mice are more asymmetric than the three wild-type mice. The wild-type mice have a few asymmetric regions of up to approximately 0.4 mm. It is quite hard for a layman to detect any asymmetry merely by looking at the original wild-type mouse surfaces in row (b) (first three). The measured asymmetries in Crouzon mice are much higher, or more than 0.8 mm in some regions. Regions of highest asymmetry are located in the regions of the nose, the posterior skull, the anterior skull and the zygomatic bone. In most cases, these detections are easily verified by looking at the original surfaces.

Figure 11.11 reveals that, on average, the Crouzon mouse skull is more asymmetric than the wild-type mouse skull in the posterior skull, the zygomatic bone and the nose. The nose finding is significant while only small regions in the posterior skull and zygomatic bone are significantly more asymmetric in the Crouzon skull. Perhaps larger significant regions would be revealed given a larger data set.

The two children from the control group in Figure 11.8, 11.9 and 11.10, are mostly symmetric. For case 1, the detected asymmetry in the chin seems to be related to scanning artifacts (see the original surface) rather than the actual anatomy. For both UCS children, transversal asymmetries are detected in the mid-face. For case 3, mandibular transversal asymmetry is also present. This may especially be seen from the skull representation in Figure 11.10 but it is also seen to affect the asymmetry of the chin in the soft-tissue representation in Figure 11.8. Sagittal asymmetry is present in the forehead and eyes and vertical asymmetry is seen at the zygoma in Figure 11.10, especially for case 3. This trend is reflected, although slightly less evident, in the cheeks of cases 3 and 4 in Figure 11.8. The majority of these findings is in good agreement with a qualitative inspection of the original surfaces.

The group comparison of total absolute asymmetries in the UCS data in Figure 11.12 indicates that for soft tissue, UCS children are on average more asymmetric than the controls in the midface, ears and posterior head, although only the midface and posterior head findings are significant. For the skull, UCS skulls are on average more asymmetric than normal skulls in the midface (including nasal and orbital region), maxilla, mandible and the parietal bone (at posterior skull). These findings are significant in the midface, maxilla and a small region of the parietal bone. These significant differences are observed despite of the limited number of controls. In fact, there was a large variation in the control group and perhaps, given more controls, significant regions differing in asymmetry would be larger.

The comparison of interior cranial base asymmetries in Figure 11.13 indicates that UCS skulls are on average more asymmetric in the anterior and mid-cranial fossae. The middle part of the anterior cranial fossae is strongly significant, while only parts of the mid-cranial fossae are found to be significant.

These results for the UCS data confirm previous findings with respect to asymmetry in the orbital region and cranial fossae in [22, 75, 114, 135, 136, 142, 149]. Further, the approach detects asymmetry in part of the posterior head in addition to the maxilla and part of the mandible as reported in [109, 114, 149].

However, the mandibular findings were not significant. In the present study, we have only looked at group differences with respect to total absolute asymmetries. It still remains to investigate the group difference in terms of the individual asymmetry components (transverse, sagittal and vertical) leaving a great potential for a further clinical study on the condition.

Figure 11.14 strongly indicates that Crouzon mice are more asymmetric than wild-type mice in all types of asymmetry (total, transverse, sagittal and vertical). The same is evident from the UCS plots, both for soft tissue and skull, i.e. UCS heads are more asymmetric than normal. The largest variation appears to be in the sagittal asymmetry for both UCS and normal children. Paired t-tests confirmed the group means to be different for both applications and all types of asymmetries.

The registration accuracy was validated by a point to surface approach in Table 11.1 and Figure 11.15. Even though only a lower bound on the point to point (correspondence) accuracy is provided, the approach has the advantage of demonstrating the error spatially, as opposed to landmark validation. The results strongly indicate good registration accuracy for both applications. The soft tissue results are slightly worse than the skull results for the UCS data set. This has to do firstly with the scan quality (see e.g. case 1 and 2 in Figure 11.8(d)). Secondly, even though pre-processing was carried out, the data varied heavily from scan to scan, with respect to the presence of the neck and shoulders. This constituted a larger part for the soft tissue than for the skull. However, the neck is of minimal interest for the asymmetry calculations and these errors were considered irrelevant. Thirdly, there are more complicated structures in the soft tissue than in the skull, such as the ears, which are not matched accurately as seen in Figure 11.15(a,c). The mouth region is also difficult since some children have open mouths while others have closed mouths during scanning. Moreover, the errors are high on the top of the skull. This is due to the different size of the fontanelle, the opening between the parietal bone and the frontal bone. Such large differences are hard to match. If e.g. the fontanelle is fully closed in the source skull, the non-rigid registration does not allow it to open to match the target skull. The same applies to the open/closed mouth example. One way to solve this problem would be to include landmarks in the difficult regions. The quantification of registration accuracy is an important indicator of the reliability of the subsequent asymmetry determination. Fortunately, none of the above mentioned regions with relatively high registration error is of particular interest for the study of asymmetry in UCS and it is therefore concluded that the overall registration accuracy is sufficient for further analysis.

The expert validation of cranial asymmetry in Crouzon mice in Figure 11.16 indicates that the method localizes and quantifies asymmetry in close agreement with a clinical expert. With the selected threshold of asymmetry ($(|A_i > 0.25|)$, a sensitivity of 95% was reached. The specificity was only 66% indicating a high number of false positives. This indicates that selecting a higher level of detection (threshold) would further improve the results but this kind of validation is obviously subjective. It is our belief that a clinical expert rating for the Crouzon mice was necessary since only one previous study was found where asymmetry due to Crouzon syndrome was mentioned. This, in addition to the fact that we confirm the locations of asymmetry with respect to previous studies on UCS, leads to the conclusion that the proposed approach accurately locates correct regions of asymmetry.

11.7 Conclusions

It has been shown that the proposed asymmetry measure is able to convincingly assess asymmetries in craniofacial data. Previous findings with respect to UCS were confirmed and good agreement with respect to a clinical expect rating on Crouzon skulls was obtained. The presented approach differs from previous studies on UCS in the level of detail. Instead of relying on a sparse set of reference points, it provides a full volumetric quantification. The presented results are of high value for craniofacial surgery planning and evaluation. With respect to other medical applications, the essence of the presented methodology is that it is free of defining the mid-sagittal plane in every subject and should be easily extendable to any application where bilateral asymmetry is of interest.

Acknowledgments

For all image registrations, the Image Registration Toolkit was used under Licence from Ixico Ltd[1].

For all surface visualisations, landmarking and closest point calculations, the freely available, VTK-based software, landmarker[2] was used [52].

---

[1] http://www.doc.ic.ac.uk/ dr/software/

[2] http://www.lab3d.odont.ku.dk/landmarker

List of Tables

List of Figures

List of Algorithms

Bibliography

[1] www.emedicine.com: Craniosynostosis. positional plagiocephaly, Nov 2007.

[2] www.sickkids.ca: Unicoronal synostosis, Nov 2007.

[3] Y. Amit, U. Grenander, and M. Piccioni. Structural Image Restoration Through Deformable Templates. *Journal of the American Statistical Association*, 86(414):376–387, 1991.

[4] R.J. Anderson, T.A. Darvann, H. Ólafsdóttir, D.W. Hansen, R. Larsen, N.V. Hermann, P. Larsen, A.E. Van Pelt, D. Govier, M.J. Tenenbaum, S. Naidoo, , S. Kreiborg, and A.A. Kane. Automated landmarking of 3d infant face surfaces using 2d active appearance models. In *Mouth and Face Forum 2008 - in silico Dentistry, Osaka, Japan (accepted)*, 2008.

[5] P.R. Andresen and M. Nielsen. Non-rigid registration by geometry-constrained diffusion. *Medical Image Analysis*, 5(2):81–88, 2001.

[6] P.R. Andresen, F.L. Bookstein, K. Conradsen, B.K. Ersboll, J.L. Marsh, and S. Kreiborg. Surface-bounded growth modeling applied to human mandibles. *IEEE Transactions on Medical Imaging*, 19(11):1053–63, 2000.

[7] J. Ashburner and K.J. Friston. Nonlinear spatial normalization using basis functions. *Human Brain Mapping*, 7(4):254–266, 1999.

[8] J. Ashburner, C. Hutton, R. Frackowiak, I. Johnsrude, C. Price, and K. Friston. Identifying global anatomical differences: Deformation-based morphometry. *Human Brain Mapping*, 6(5-6):348–357, 1998.

[9] T. Baccetti, L. Franchi, J.A. McNamara, et al. Thin-plate spline analysis of treatment effects of rapid maxillary expansion and face mask therapy in early Class III malocclusions. *The European Journal of Orthodontics*, 21(3):275, 1999.

[10] R. Bajcsy and S.Kovačič. Multiresolution elastic matching. *Comput. Vision Graph. Image Process.*, 46(1):1–21, 1989.

[11] S. Baker and I. Matthews. Lucas-kanade 20 years on: A unifying framework. *International Journal of Computer Vision*, 56(3):221–255, 2004.

[12] Y. Benjamini and Y. Hochberg. Controlling the false discovery rate: a practical and powerful approach to multiple testing. *Journal of the Royal Statistical Society - Series B Statistical Methodology*, 57(1):289, 1995.

[13] J.M. Bland and D.G. Altman. Statistical methods for assessing agreement between two methods of clinical measurement. *The Lancet*, i:307–310, 1986.

[14] M.M. Boere-Boonekamp and L.T. van der Linden-Kuiper. Positional Preference: Prevalence in Infants and Follow-Up After Two Years. *Pediatrics*, 107(2):339–343, 2001.

[15] F. L. Bookstein. Principal warps: thin-plate splines and the decomposition of deformations. *IEEE Transactions on Pattern Analysis and Machine Intelligence*, 11(6):567–85, 1989.

[16] F.L. Bookstein. *Morphometric Tools for Landmark Data.* Cambridge, 1997.

[17] F.L. Bookstein. Thin-Plate Splines and the Atlas Problem for Biomedical Images. *Proceedings of the 12th International Conference on Information Processing in Medical Imaging*, pages 326–342, 1991.

[18] R. Brandt, T. Rohlfing, J. Rybak, S. Krofczik, A. Maye, M. Westerhoff, H-C. Hege, and R. Menzel. Three-dimensional average-shape atlas of the honeybee brain and its applications. *Journal of Comparative Neurology*, 492(1):1–19, 2005.

[19] B.H. Broadbent. A new X-ray technique and its application to orthodontia. *Angle Orthodontist*, 1(2):45–66, 1931.

[20] T. Brown and A.H. Abbott. Computer-assisted location of reference points in three dimensions for radiographic cephalometry. *American Journal of Orthodontics and Dentofacial Orthopedics*, 95(6):490–498, 1989.

[21] J. Cao and K. J. Worsley. The detection of local shape changes via the geometry of hotelling's T2 fields. *Ann. Statist.*, 27:925–942, 1999.

[22] G. Captier, N. Leboucq, M. Bigorre, F. Canovas, F. Bonnel, A. Bonnafé, and P. Montoya. Plagiocephaly: morphometry of skull base asymmetry. *Surgical and Radiologic Anatomy*, 25(3):226–233, 2003.

[23] F. Carinci, A. Avantaggiato, and C. Curioni. Crouzon syndrome: Cephalometric analysis and evaluation of pathogenesis. *Cleft Palate Craniofacial Journal*, 31(3):201–209, 1994.

[24] L.B. Cassileth, S.P. Bartlett, P.M. Glat, K.W. Gripp, M. Muenke, E.H. Zackai, and L.A. Whitaker. Clinical characteristics of patients with unicoronal synostosis and mutatio ns of fibroblast growth factor receptor 3: A preliminary report. *Plastic and Reconstructive Surgery*, 108(7):1849, 2001.

[25] L.H.S. Cevidanes, A.A. Franco, G. Gerig, W.R. Proffit, D.E. Slice, D.H. Enlow, H.K. Yamashita, Y-J Kim, M.A. Scanavini, and J.W. Vigorito. Assessment of mandibular growth and response to orthopedic treatment with 3-dimensional magnetic resonance images. *American Journal of Orthodontics and Dentofacial Orthopedics*, 128(1):16, 2005.

[26] L.H.S. Cevidanes, L.T.J. Bailey, S.F. Tucker, M.A. Styner, A. Mol, C.L. Phillips, W.R. Proffit, and T. Turvey. Three-dimensional cone-beam computed tomography for assessment of mandibular changes after orthognathic surgery. *American Journal of Orthodontics and Dentofacial Orthopedics*, 131(1):44, 2007.

[27] P.Y. Chang, N.C. Chang, D.B. Perng, Y.W. Chien, and F.Y. Huang. Computer-aided measurement of cranial asymmetry in children with and without torticollis. *Clinical Orthodontics and Research*, 4:200–205, 2001.

[28] F. S. Chebib and A. M. Chamma. Indices of craniofacial asymmetry. *Angle Orthodontist*, 51(3):214–26, 1981.

[29] G. E. Christensen, R. D. Rabbitt, and M. I. Miller. Deformable templates using large deformation kinematics. *IEEE Trans. on Image Processing*, 4(10):1435–1447, 1996.

[30] G.E. Christensen, M.I. Miller, J.L. Marsh, and M.W. Vannier. Automatic analysis of medical images using a deformable textbook. *Computer assisted radiology*, pages 146–151, 1995.

[31] G.E. Christensen, A.A. Kane, J.L. Marsh, and M.W. Vannier. Synthesis of an individualized cranial atlas with dysmorphic shape. *Proceedings of the Workshop on Mathematical Methods in Biomedical Image Analysis*, pages 309–18, 1996.

[32] G.E. Christensen, H.J. Johnson, T. Darvann, N. Hermann, and J.L. Marsh. Midsagittal surface measurement of the head: an assessment of craniofacial asymmetry. *Proceedings of the SPIE - The International Society for Optical Engineering*, 3661:612–19, 1999.

[33] G.E. Christensen, X. Geng, J.G. Kuhl, J. Bruss, T.J. Grabowski, I.A. Pirwani, M.W. Vannier, J.S. Allen, and H. Damasio. Introduction to the non-rigid image registration evaluation project (NIREP). *Proceedings of SPIE*, 4057:128–135, 2006.

[34] G.E. Christensen, H.J. Johnson, and M.W. Vannier. Synthesizing average 3D anatomical shapes. *Neuroimage*, 32(1):146–158, 2006.

[35] M.K. Chung, K.J. Worsley, T. Paus, C. Cherif, D.L. Collins, J.N. Giedd, J.L. Rapoport, and A.C. Evans. A unified statistical approach to deformation-based morphometry. *NeuroImage*, 14(3):595–606, 2001.

[36] M.M. Cohen and R.E. MacLean. *Craniosynostosis: diagnosis, evaluation, and management*. Raven Press, 1986.

[37] M.M. Cohen Jr and S. Kreiborg. Birth prevalence studies of the Crouzon syndrome: comparison of direct and indirect methods. *Clinical Genetetics*, 41(1):12–5, 1992.

[38] M.J. Cook. The anatomy of the laboratory mouse (reprinted on the web), 1965. URL `http://www.informatics.jax.org/cookbook/`.

[39] T. F. Cootes and Taylor. Active shape models – 'smart snakes'. In *Proceedings of the British Machine Vision Conference*, pages 266–275, 1992.

[40] T.F. Cootes, G.J. Edwards, and C.J. Taylor. Active appearance models. *Pattern Analysis and Machine Intelligence, IEEE Transactions on*, 23(6):681–685, 2001.

[41] T.F. Cootes, C.J. Twining, and C.J. Taylor. Diffeomorphic Statistical Shape Models. *Proceedings of the British Machine Vision Conference*, 1:447–456, 2004.

[42] T.F. Cootes, C.J. Twining, V. Petrovic, R. Schestowitz, and C.J. Taylor. Groupwise construction of appearance models using piece-wise affine deformations. *Proceedings of the British Machine Vision Conference*, 2005.

[43] O. Crouzon. Dysostose cranio-faciale héréditère. *Bull Mem Soc Méd Hôp Paris*, 33: 545–555, 1912.

[44] W.R. Crum, O. Camara, and D.L.G. Hill. Generalized Overlap Measures for Evaluation and Validation in Medical Image Analysis. *IEEE Transactions on Medical Imaging*, 25 (11):1451–1461, 2006.

[45] J. Csernansky, J. Sarang, L. Wang, J.W. Haller, M. Gado, J.P. Miller, U. Grenander, and M.I. Miller. Hippocampal morphometry in schizophrenia by high dimensional brain mapping. *Proceedings of the National Academy of Sciences of the United States of America*, 95(19):11406–11411, 1998.

[46] J.G. Csernansky, L. Wang, S.C. Joshi, J.T. Ratnanather, and M.I. Miller. Computational anatomy and neuropsychiatric disease: probabilistic assessment of variation and statistical inference of group difference, hemispheric asymmetry, and time-dependent change. *NeuroImage*, 23(Supplement 1):S56–S68, 2004.

[47] J.G. Csernansky, L. Wang, J.P. Miller, J.E. Galvin, and J.C. Morris. Neuroanatomical predictors of response to donepezil therapy in patients wit h dementia. *Archives of Neurology*, 62(11):1718, 2005.

[48] M.B Cuadra, C. Pollo, A. Bardera, O. Cuisenaire, J.-G. Villemure, and J.-P. Thiran. Atlas-based segmentation of pathological MR brain images using a model of lesion growth. *IEEE Transactions on Medical Imaging*, 23(10):1301–1314, 2004.

[49] C. Cutting, D. Dean, F.L. Bookstein, B. Haddad, D. Khorramabadi, F.W. Zonneveld, and J.G. McCarthy. A three-dimensional smooth surface analysis of untreated Crouzon´s syndrome in the adult. *Journal of Craniofacial Surgery*, 6(6):444–453, 1995.

[50] A.M. Dale, A.K. Liu, B.R. Fischl, R.L. Buckner, J.W. Belliveau, J.D. Lewine, and E. Halgren. Dynamic Statistical Parametric Mapping Combining fMRI and MEG for High-Resolution Imaging of Cortical Activity. *Neuron*, 26(1):55–67, 2000.

[51] S. Darkner, R. Larsen, and R.R. Paulsen. Analysis of deformation of the human ear and canal caused by mandibular movement. In *Medical image computing and computer assisted intervention*, volume 4792 of *Lecture Notes in Computer Science*, page 801, 2007.

[52] T.A. Darvann. Landmarker: A vtk-based tool for landmarking of polygonal surfaces. In *Mouth and Face Forum 2008 - in silico Dentistry, Osaka, Japan (invited contribution)*, 2008.

[53] T.A. Darvann. *Methods for Measurements and Analysis of Craniofacial Morphology and Growth in Children with Cleft Lip and Palate.* PhD thesis, Informatics and Mathematical Modelling, Technical University of Denmark, DTU, 2003.

[54] T.A. Darvann, N.V. Hermann, Tenenbaum, Govier M.J., S. D., Naidoo, P. Larsen, S. Kreiborg, and A.A. Kane. Head shape development in positional plagiocephaly: Methods for registration of surface scans. In T.A. Darvann, Hermann N.V., P. Larsen, and S. Kreiborg, editors, *MICCAI 2006 workshop: Craniofacial Image Analysis for Biology, Clinical Genetics, Diagnostics and Treatment*, pages 59–66, 2006.

[55] T.A. Darvann, H. Ólafsdóttir, N.V. Hermann, P. Larsen, S. Lanche, R. Larsen, B.K. Ersbøll, D. Govier, A.E. Van Pelt, A.A. Kane, and S. Kreiborg. On the measurement of craniofacial asymmetry. In *Mouth and Face Forum 2008 - in silico Dentistry, Osaka, Japan (invited contribution)*, 2008.

[56] R. H. Davies, C. J. Twining, T. F. Cootes, J. C. Waterton, and C. J. Taylor. A minimum description length approach to statistical shape modeling. *IEEE Transactions on Medical Imaging*, 21(5):525–537, 2002.

[57] T.S. Douglas. Image processing for craniofacial landmark identification and measurement: a review of photogrammetry and cephalometry. *Computerized Medical Imaging and Graphics*, 28(7):401–409, 2004.

[58] I.L. Dryden and K.V. Mardia. *Statistical Shape Analysis.* John Wiley & Sons, 1998.

[59] V. Duay, N. Houhou, and J.-P. Thiran. Atlas-based segmentation of medical images locally constrained by level sets. *International Conference on Image Processing 2005. Proceedings*, pages II–1286–1289, 2006.

[60] S. Durrleman, X. Pennec, A. Trouve, and N. Ayache. Measuring brain variability via sulcal lines registration: A diffeomorphic approach. In *Medical Image Computing and Computer-Assisted Intervention*, volume 4791 of *Lecture Notes in Computer Science*, page 675, 2007.

[61] R. Edler, D. Wertheim, and D. Greenhill. Outcome measurement in the correction of mandibular asymmetry. *American Journal of Orthodontics and Dentofacial Orthopedics*, 125(4):435, 2004.

[62] B. Efron. Large-scale simultaneous hypothesis testing: The choice of a null hypothesis. *Journal of the American Statistical Association*, 99(465):96–104, 2004.

[63] V. P. Eswarakumar, M. C. Horowitz, R. Locklin, G. M. Morriss-Kay, and P. Lonai. A gain-of-function mutation of fgfr2c demonstrates the roles of this receptor variant in osteogenesis. *Proceedings of the National Academy of Sciences*, 101:12555–12560, 2004.

[64] V.F Ferrario, C. Sforza, C.E. Poggio, and G. Tartaglia. Distance from symmetry: a three-dimensional evaluation of facial asymmetry. *Journal of Oral Maxillofacial Surgery*, 52(11):1126–32, 1994.

[65] V.F. Ferrario, C. Sforza, V. Ciusa, C. Dellavia, and G.M. Tartaglia. The effect of sex and age on facial asymmetry in health y subjects: A cross-sectional study from adolescence to mid-adulthood. *Journal of Oral and Maxillofacial Surgery*, 59(4):382, 2001.

[66] P. Fillard, V. Arsigny, X. Pennec, P.M. Thompson, and N. Ayache. Extrapolation of sparse tensor fields: Application to the modeling of brain variability. In G.E. Christensen and M. Sonka, editors, *Proceedings of IPMI*, volume 3565 of *Lecture Notes in Computer Science*, pages 27–38. Springer-Verlag, 2005.

[67] B. Fischer and J. Modersitzki. A unified approach to fast image registration and a new curvature based registration technique. *Linear Algebra and Its Applications*, 380: 107–124, 2004.

[68] J.M. Flores, I. Bloch, F. Schmitt, C. Grangeat, and T. Bousquet. Shape-Based Averaging for Craniofacial Anthropometry. *Proceedings of the Sixth Mexican International Conference on Computer Science*, pages 314–319, 2005.

[69] L. Franchi, T. Baccetti, and J.A. McNamara. Thin-plate spline analysis of mandibular growth. *Angle Orthodontist*, 71(2):83, 2001.

[70] A.F. Frangi, D. Rueckert, J.A. Schnabel, and W.J. Niessen. Automatic construction of multiple-object three-dimensional statistical shape models: Application to cardiac modeling. *IEEE Transactions on Medical Imaging*, 21(9):1151–66, 2002.

[71] K. J. Friston, A. P. Holmes, K. J. Worsley, J.-P. Poline, C. D. Frith, and R. S. J. Frackowiak. Statistical parametric maps in functional imaging: A general linear approach. *Human Brain Mapping*, 2(4):189–210, 1995.

[72] R. Gan and A.C.S. Chung. Multi-dimensional mutual information based robust image registration using maximum distance-gradient-magnitude. *Lecture Notes in Computer Science*, 3565:210–221, 2005.

[73] C. Gaser, H.P. Volz, S. Kiebel, S. Riehemann, and H. Sauer. Detecting structural changes in whole brain based on nonlinear deformations-application to schizophrenia research. *NeuroImage*, 10(2):107–113, 1999.

[74] C. Gaser, I. Nenadic, B.R. Buchsbaum, E.A. Hazlett, and M.S. Buchsbaum. Deformation-based morphometry and its relation to conventional volumetry of brain lateral ventricles in MRI. *NeuroImage*, 13(6):1140–1145, 2001.

[75] L. Genitori, N. Zanon, D. Denis, P. Erdincler, M. Achouri, G. Lena, and M. Choux. The skull base in plagiocephaly. *Child's Nervous System*, 10(4):217–223, 1994.

[76] G. Gerig, M. Styner, D. Jones, D. Weinberger, and J. Lieberman. Shape analysis of brain ventricles using SPHARM. *IEEE Workshop on Mathematical Methods in Biomedical Image Analysis, 2001. MMBIA 2001.*, pages 171–178, 2001.

[77] N. Glerup. *Asymmetry Measures in Medical Image Analysis.* PhD thesis, The IT University of Copenhagen, Copenhagen, Denmark, 2005.

[78] S. Good, R. Edler, D. Wertheim, and D. Greenhill. A computerized photographic assessment of the relationship between skeletal discrepancy and mandibular outline asymmetry. *The European Journal of Orthodontics*, 28(2):97–102, 2006.

[79] J. Gregersen and C. Madsen. Shape analysis and point correpondence of facial surfaces. Master's thesis, Master's Thesis no.99/05, Informatics and Mathematical Modelling, Technical Univeristy of Denmark, 2005.

[80] U. Grenander and M. I. Miller. Representation of knowledge in complex systems. *Journal of Royal Statistical Society, Series B*, 56(4):549–603, 1994.

[81] U. Grenander and M.I. Miller. Computational anatomy: An emerging discipline. *Quarterly of Applied Mathematics*, 56(4):617, 1998.

[82] A. Guimond, J. Meunier, and J-P. Thirion. Average brain models: A convergence study. *Computer Vision and Image Understanding*, 77(2):192–210, 2000.

[83] Y. Guo, C-H. Lo, and C-C. Lu. Multi-modality image registration using gradient vector flow intensity. *Lecture Notes in Computer Science*, 4091:277–284, 2006.

[84] E. Haber and J. Modersitzki. Intensity gradient based registration and fusion of multi-modal images. *Lecture Notes in Computer Science*, 4191:726–733, 2006.

[85] M.Y. Hajeer, A.F. Ayoub, and D.T. Millett. Three-dimensional assessment of facial soft-tissue asymmetry before and after orthognathic surgery. *British Journal of Oral & Maxillofacial Surgery*, 42(5):396–404, 2004.

[86] J.V. Hajnal, N Saeed, A Oatridge, E.J. Williams, I.R. Young, and G.M. Bydder. Detection of subtle brain changes using subvoxel registration and subtraction of serial MR images. *Journal of Computer Assisted Tomography*, 19(5):677–91, 1995.

[87] D.J. Halazonetis. Morphometrics for cephalometric diagnosis. *American Journal of Orthodontics and Dentofacial Orthopedics*, 125(5):571, 2004.

[88] B. Hallgrímsson, C.J. Dorval, M.L. Zelditch, and R.Z. German. Craniofacial variability and morphological integration in mice susceptible to cleft lip and palate. *Journal of Anatomy*, 205(6):501–517, 2004.

[89] B. Hallgrímsson, DE Lieberman, W. Liu, AF Ford-Hutchinson, and FR Jirik. Epigenetic interactions and the structure of phenotypic variation in the cranium. *Evolution & Development*, 9(1):76–91, 2007.

[90] P. Hammond, T.J. Hutton, J.E. Allanson, L.E. Campbell, R.C.M. Hennekam, S. Holden, M.A. Patton, A. Shaw, I.K. Temple, M. Trotter, et al. 3D analysis of facial morphology. *Americal Journal of Medical Genetics*, 126(4):339–48, 2004.

[91] M.S. Hansen, H. Ólafsdóttir, T.A. Darvann, N.V. Hermann, E. Oubel, R. Larsen, B.K. Ersbøll, A.F. Frangi, P. Larsen, C.A. Perlyn, G.M. Morris-Kay, and S. Kreiborg. Estimation of independent non-linear deformation modes for analysis of craniofacial malformations in Crouzon mice. In J.A. Fessler M. Wernick, editor, *2007 IEEE International Symposium on Biomedical Imaging*. IEEE, 2007.

[92] M.S. Hansen, H. Ólafsdóttir, K. Sjöstrand, H.B. Larsson, M.B. Stegmann, and R. Larsen. Ischemic segment detection using the support vector domain description. In The International Society for Optical Engineering (SPIE), editor, *International Symposium on Medical Imaging*, 2007.

[93] M.S. Hansen, K. Sjostrand, H. Ólafsdóttir, H.B.W. Larsson, M.B. Stegmann, and R. Larsen. Robust pseudo-hierarchical support vector clustering. In *Scandinavian Conference on Image Analysis 2007*, volume 4522 of *Lecture Notes in Computer Science*, pages 808–17, 2007.

[94] R.J. Hennessy and C.B. Stringer. Geometric morphometric study of the regional variation of modern human craniofacial form. *American Journal of Physical Anthropology*, 117(1):37–48, 2002.

[95] R.J. Hennessy, A. Lane, A. Kinsella, C. Larkin, E. O'Callaghan, and J.L. Waddington. 3D morphometrics of craniofacial dysmorphology reveals sex-specific asymmetries in schizophrenia. *Schizophrenia Research*, 67(2-3):261–268, 2004.

[96] N.V. Hermann, B.L. Jensen, E. Dahl, T.A. Darvann, and S. Kreiborg. A method for three-projection infant cephalometry. *Cleft Palate Craniofac Journal*, 38(4):299–316, 2001.

[97] N.V. Hermann, T.A. Darvann, B.L. Jensen, E. Dahl, S. Bolund, and S. Kreiborg. Early craniofacial morphology and growth in children with bilateral complete cleft lip and palate. *Cleft Palate Craniofac Journal*, 41(4):424–38, 2004.

[98] K.B. Hilger, R. Larsen, and M. Wrobel. Growth modeling of human mandibles using non-Euclidean metrics. *Medical Image Analysis*, 7:425–433, 2003.

[99] R.E. Hogan, L. Wang, M.E. Bertrand, L.J. Willmore, R.D. Bucholz, A.S. Nassif, and J.G. Csernansky. Predictive Value of Hippocampal MR Imaging-Based High-Dimensional Mapping in Mesial Temporal Epilepsy: Preliminary Findings. *American Journal of Neuroradiology*, 27(10):2149, 2006.

[100] C.A. Hood, M. Bock, M.T. Hosey, A. Bowman, and A.F. Ayoub. 3D assessment of infants with cleft lip & palate. *International Journal of Paediatric Dentistry*, 13(6): 404, 2003.

[101] P. Hummel and D. Fortado. A parents' guide to improving head shape. *Adv. Neonatal Care*, 5:341–342, 2005.

[102] T.J. Hutton, B.F. Buxton, P. Hammond, and H.W.W. Potts. Estimating average growth trajectories in shape-space using kernel smoothing. *IEEE Transactions on Medical Imaging*, pages 747–753, 2003.

[103] H.S. Hwang, C.H. Hwang, K.H. Lee, and B.C. Kang. Maxillofacial 3-dimensional image analysis for the diagnosis of facial asymmetry. *American Journal of Orthodontics and Dentofacial Orthopedics*, 130(6):779, 2006.

[104] A. Hyvärinen. Survey on independent component analysis. *Neural Computing Surveys*, 2:94–128, 1999.

[105] S. Joshi, P. Lorenzen, G. Gerig, and E. Bullitt. Structural and radiometric asymmetry in brain images. *Medical Image Analysis*, 7(2):155–170, 2003.

[106] S. Joshi, B. Davis, M. Jomier, and G. Gerig. Unbiased diffeomorphic atlas construction for computational anatomy. *NeuroImage*, 23:S151–S160, 2004.

[107] S. Kabus, T. Netsch, B. Fischer, and J. Modersitzki. B-spline registration of 3D images with Levenberg-Marquardt optimization. *Proceedings of SPIE*, 5370:304–313, 2004.

[108] P. Kambylafkas, S. Kyrkanides, and R.H. Tallents. Mandibular Asymmetry in Adult Patients with Unilateral Degenerative Joint Disease. *Angle Orthodontist*, 75(3):297–302, 2005.

[109] A.A. Kane, L.J. Lo, M.W. Vannier, and J.L. Marsh. Mandibular dysmorphology in unicoronal synostosis and plagiocephaly without synostosis. *Cleft Palate Craniofac J*, 33(5):418–23, 1996.

[110] J. Kattwinkel, J. Brooks, and D. Myerberg. Positioning and SIDS. AAP Task Force on Infant Positioning and SIDS. *Pediatrics*, 89:1120–1126, 1992.

[111] C.P. Klingenberg. Morphometrics and the role of the phenotype in studies of the evolution of developmental mechanisms. *Gene*, 287(1-2):3–10, 2002.

[112] C.P. Klingenberg, M. Barluenga, and A. Meyer. Shape analysis of symmetric structures: quantifying variation among individuals and asymmetry. *Evolution*, 56(10):1909–1920, 2000.

[113] J.C. Kolar and E.M. Salter. *Craniofacial Anthropometry. Practical Measurement of the Head and Face for Clinical, Surgical and Research Use.* Charles C. Thomas Publisher, 1997.

[114] S. Kreiborg and A. Bjork. Craniofacial asymmetry of a dry skull with plagiocephaly. *The European Journal of Orthodontics*, 3(3):195, 1981.

[115] S. Kreiborg, J.L. Marsh, M. M. Jr. Cohen, M. Liversage, H. Pedersen, F. Skovby, S.E. Borgesen, and M.W. Vannier. Comparative three-dimensional analysis of CT scans of the calvaria and cranial base in Apert and Crouzon syndromes. *Journal of Craniomaxillofacial Surgery*, 21(5):181–188, 1993.

[116] S. Kreiborg, P. Larsen, T.A. Darvann, H. Ólafsdóttir, N.V. Hermann, and H.H. Dahlgard. 3D craniofacial growth analysis. In *Mouth and Face Forum 2008 - in silico Dentistry, Osaka, Japan (invited contribution)*, 2008.

[117] Sven Kreiborg. *Crouzon Syndrome - A Clinical and Roentgencephalometric Study*, 1981. Doctorate thesis, Institute of Orthodontics, The Royal Dental College, Copenhagen.

[118] T.G. Kwon, H.S. Park, H.M. Ryoo, and S.H. Lee. A comparison of craniofacial morphology in patients with and without facial asymmetry-: a three-dimensional analysis with computed tomography. *International Journal of Oral and Maxillofacial Surgery*, 35(1):43–48, 2006.

[119] Y.F. Lam, D.F. Gillies, D. Rueckert, P. Charters, P. Groom, and S. Roughley. A generic anatomical model of the human mandible. *Proceedings of the IASTED International Conference on Biomechanics*, pages 247–251, 2003.

[120] J.L. Lancaster, P.V. Kochunov, P.M. Thompson, A.W. Toga, and P.T. Fox. Asymmetry of the brain surface from deformation field analysis. *Human Brain Mapping*, 19(2):79–89, 2003.

[121] S. Lanche, T.A. Darvann, H. Ólafsdóttir, N.V. Hermann, A.E. Van Pelt, D. Govier, M.J. Tenenbaum, S. Naidoo, P. Larsen, S. Kreiborg, R. Larsen, and A.A. Kane. A statistical model of head asymmetry in infants with deformational plagiocephaly. In B.K. Ersbøll and K.S. Pedersen, editors, *Scandinavian Conference on Image Analysis 2007*, volume 4522 of *LNCS*, pages 898–907. Springer, 2007.

[122] S. Lanche, T.A. Darvann, H. Ólafsdóttir, N.V. Hermann, A.V. Pelt, D. Gover, M.J. Tenebaum, S. Naidoo, P. Larsen, S. Kreiborg, R. Larsen, and A.A. Kane. A method for evaluating treatment in infants with deformational plagiocephaly. In *Image Analysis and In-Vivo Pharmacology*, 2007.

[123] S. Lanche, T.A. Darvann, H. Ólafsdóttir, N.V. Hermann, A.E. Van Pelt, D. Govier, M.J. Tenenbaum, S. Naidoo, P. Larsen, S. Kreiborg, R. Larsen, and A.A. Kane. Validation of a statistical model of head asymmetry in infants with deformational plagiocephaly. In *Mouth and Face Forum 2008 - in silico Dentistry, Osaka, Japan (accepted)*, 2008.

[124] B.J Langberg, K. Arai, and R.M. Miner. Transverse skeletal and dental asymmetry in adults with unilateral lingual posterior crossbite. *American Journal of Orthodontics and Dentofacial Orthopedics*, 127(1):6, 2005.

[125] G. Le Goualher, E. Procyk, D.L. Collins, R. Venugopal, C. Barillot, and A.C. Evans. Automated extraction and variability analysis of sulcal neuroanatomy. *IEEE Transactions on Medical Imaging*, 18(3):206–217, 1999.

[126] S. Lee, G. Wolberg, and S.Y. Shin. Scattered data interpolation with multilevel B-splines. *IEEE Transactions on Visualization and Computer Graphics*, 3(3):228–244, 1997.

[127] W.T. Lee, K. Richards, J. Redhed, and F.A. Papay. A pneumatic orthotic cranial molding helmet for correcting positional plagiocephaly. *J. Craniofac. Surg.*, 17:139–144, 2006.

[128] R. Lele and T. Richtsmeier. *An Invariant Approach to Statistical Analysis of Shapes.* Chapman & Hall/CRC., 2001.

[129] S. Lele and J.T. Richtsmeier. Euclidean distance matrix analysis: A coordinate-free approach for comparing biological shapes using landmark data. *American Journal of Physical Anthropology*, 86(3):415–427, 1991.

[130] L. Lemieux, N. D. Kitchen, S. W. Hughes, and D. G. T. Thomas. Voxel-based localization in frame-based and frameless stereotaxy and its accuracy. *Medical Physics*, 21: 1301–1310, 1994.

[131] R. Leonardi, D. Giordano, F. Maiorana, and C. Spampinato. Automatic Cephalometric Analysis. *Angle Orthodontist*, 78(1):145–151, 2007.

[132] A. Leow, C.L. Yu, S.J. Lee, S.C. Huang, H. Protas, R. Nicolson, K.M. Hayashi, A.W. Toga, and P.M. Thompson. Brain structural mapping using a novel hybrid implicit/explicit framework based on the level-set method. *Neuroimage*, 24(3):910–927, 2005.

[133] N. Lepore, C. A. Brun, M.C. Chiang, Y.Y Chou, R. A. Dutton, K. M. Hayashi, O. L. Lopez, H. J. Aizenstein, A. W. Toga, J. T. Becker, and P. M. Thompson. Multivariate statistics of the jacobian matrices in tensor based morphometry and their application to hiv/aids. *Lecture Notes in Computer Science*, 4190:191–198, 2006.

[134] T.R Littlefield. Cranial remodeling devices: treatment of deformational plagiocephaly and postsurgical applications. *Semin. Pediatr. Neurol.*, 11:268–277, 2004.

[135] L.J. Lo, J.L. Marsh, A.A. Kane, and M.W. Vannier. Orbital dysmorphology in unilateral coronal synostosis. *Cleft Palate Craniofac J*, 33(3):190–7, 1996.

[136] L.J. Lo, J.L. Marsh, T.K. Pilgram, and M.W. Vannier. Plagiocephaly: Differential diagnosis based on endocranial morphology. *Plastic and Reconstructive Surgery*, 97(2): 282, 1996.

[137] D. Loeckx, F. Maes, D. Vandermeulen, and P. Suetens. Temporal subtraction of thorax CR images using a statistical deformation model. *Medical Imaging, IEEE Transactions on*, 22(11):1490–1504, 2003.

[138] M. Lorenzo-Valdes, D. Rueckert, R. Mohiaddin, and G.I. Sanchez-Ortiz. Segmentation of cardiac MR images using the EM algorithm with a 4D probabilistic atlas and a global connectivity filter. *Proceedings of the 25th Annual International Conference of the IEEE Engineering in Medicine and Biology Society, 2003.*, 1:626–629, 2003.

[139] F. Maes, A. Collignon, D. Vandermeulen, G. Marchal, and P. Suetens. Multimodality image registration by maximization of mutual information. *IEEE Transactions on Medical Imaging*, 16(2):187–198, 1997.

[140] J. B. Maintz and M. A. Viergever. A survey of medical image registration. *Medical Image Analysis*, 2(1):1–36, 1998.

[141] K.V. Mardia, F. L. Bookstein, and I. J Moreton. Statistical assessment of bilateral symmetry of shapes. *Biometrika*, 87(2):285–300, 2000.

[142] J.L. Marsh, M.H. Gado, M.W. Vannier, and W.G. Stevens. Osseous anatomy of unilateral coronal synostosis. *Cleft Palate J*, 23(2):87–100, 1986.

[143] J. Mazziotta, A. Toga, A. Evans, P Fox, J. Lancaster, K. Zilles, R. Woods, T. Paus, G. Simpson, B. Pike, C. Holmes, L. Collins, P. Thompson, D. Macdonald, M. Iacoboni, T. Schormann, K. Amunts, N. Palomero-Gallagher, S. Geyer, L. Parsons, K. Narr, N. Kabani, G. Le Goualher, D. Boomsma, T. Cannon, R. Kawashima, and B. Mazoyer. A probabilistic atlas and reference system for the human brain: International consortium for brain mapping (ICBM). *Philosophical Transactions of the Royal Society – Biological Sciences*, 356(1412):1293–1322, 2001.

[144] G. T. McIntyre and P. A. Mossey. Asymmetry of the parental craniofacial skeleton in orofacial clefting. *Journal of Orthodontics*, 29(4):299–305, 2002.

[145] J. Meinguet. Multivariate interpolation at arbitrary points made simple. *Zeitschrift für Angewandte Mathematik und Physik (ZAMP)*, 30(2):292–304, 1979.

[146] C.R. Meyer, J.L. Boes, B. Kim, P.H. Bland, K.R. Zasadny, P.V. Kison, K. Koral, K.A. Frey, and R.L. Wahl. Demonstration of accuracy and clinical versatility of mutual information for automatic multimodality image fusion using affine and thin-plate spline warped geometric deformations. *Medical Image Analysis*, 1(3):195–206, 1997.

[147] J. Modersitzki. *Numerical Methods for Image Registration.* Oxford University Press, 2004.

[148] A. Mohamed, E.I. Zacharaki, D. Shen, and C. Davatzikos. Deformable registration of brain tumor images via a statistical model of tumor-induced deformation. *Medical Image Analysis*, 10(5):752–763, 2006.

[149] D.J. Netherway, A.H. Abbott, N. Gulamhuseinwala, K.L. McGlaughlin, and P.J. Anderson. Three-dimensional computed tomography cephalometry of plagiocephaly: Asymmetry and shape analysis. *Cleft Palate Craniofacial Journal*, 43(2):201, 2006.

[150] T.E. Nichols and A.P. Holmes. Nonparametric permutation tests for functional neuroimaging: a primer with examples. *Human Brain Mapping*, 15(1):1–25, 2002.

[151] E.S. O'Broin, D. Allcutt, and M.J. Earley. Posterior plagiocephaly: proactive conservative management. *British Journal of Plastic Surgery*, 52(1):18–23, 1999.

[152] American Academy of Pediatrics Task Force on Sudden Infant Death Syndrome. A parents' guide to improving head shape. *Pediatrics*, 116:1245–1255, 2005.

[153] K.F. O'Grady and O.M. Antonyshyn. Facial asymmetry: three-dimensional analysis using laser surface scanning. *Plastic Reconstructive Surgery*, 104(7):928–937, 1999.

[154] P. O'Higgins and N. Jones. Facial growth in cercoeebus torquatus: An application of three-dimensional geometric morphometric techniques to the study of morphological variation. *Journal of Anatomy*, 193(2):251, 1998.

[155] H. Ólafsdóttir. Nonrigid registration of myocardial perfusion MRI. In *Proc. Svenska Symposium i Bildanalys, SSBA 2005, Malmø, Sweden*. SSBA, 2005.

[156] H. Ólafsdóttir, M.B. Stegmann, and H.B.W. Larsson. Automatic assessment of cardiac perfusion MRI. In *Medical image computing and computer assisted intervention*, LNCS, 2004.

[157] H. Ólafsdóttir, T.A. Darvann, E. Oubel, A.F. Frangi, N.V. Hermann, B.K. Ersbøll, and C.A. Perlyn. Towards describing Crouzon syndrome via a craniofacial atlas. In S.I. Olsen, editor, *15th Danish Conference on Pattern Recognition and Image Analysis (DSAGM)*, pages 108–114, 2006.

[158] H. Ólafsdóttir, E. Oubel, A.F. Frangi, T.A. Darvann, N.V. Hermann, S. Kreiborg, P. Larsen, B.K. Ersbøll, C.A. Perlyn, and G.M. Morriss-Kay. Automatic assessment of global craniofacial differences between Crouzon mice and wild-type mice in terms of the cephalic index. In P. Larsen T.A. Darvann, N.V. Hermann and S. Kreiborg, editors, *MICCAI 2006 workshop: Craniofacial Image Analysis for Biology, Clinical Genetics, Diagnostics and Treatment*, pages 49–57, 2006.

[159] H. Ólafsdóttir, M.B. Stegmann, B.K. Ersbøll, and H.B. Larsson. A comparison of FFD-based nonrigid registration and AAMs applied to myocardial perfusion MRI. In *International Symposium on Medical Imaging 2006, San Diego, CA*, volume 6144. The International Society for Optical Engineering (SPIE), 2006.

[160] H. Ólafsdóttir, T.A. Darvann, Ersboll B.K., N.V. Hermann, E. Oubel, R. Larsen, A.F. Frangi, P. Larsen, C.A. Perlyn, G.M. Morriss-Kay, and S. Kreiborg. Craniofacial statistical deformation models of wild-type mice and Crouzon mice. In J.P.W. Pluim and J.M. Reinhardt, editors, *Medical Imaging 2007: Image Processing*, volume 6512, page 65121C. SPIE, 2007.

[161] H. Ólafsdóttir, T.A. Darvann, N.V. Hermann, B.K. Ersbøll, E. Oubel, R. Larsen, A.F. Frangi, P. Larsen, C.A. Perlyn, G.M. Morriss-Kay, and S. Kreiborg. Automatic detection of wild-type mouse cranial sutures. In *Image Analysis and In-Vivo Pharmacology*, 2007.

[162] H. Ólafsdóttir, T.A. Darvann, N.V. Hermann, E. Oubel, B.K. Ersbøll, A.F. Frangi, P. Larsen, C.A. Perlyn, G.M. Morriss-Kay, and S. Kreiborg. Computational mouse atlases and their application to automatic assessment of craniofacial dysmorphology caused by the Crouzon mutation Fgfr2$^{\mathrm{C342Y}}$. *Journal of Anatomy*, 211(1):37–52, 2007.

[163] H. Ólafsdóttir, M.S. Hansen, K. Sjöstrand, T.A. Darvann, N.V. Hermann, E. Oubel, B.K. Ersbøll, R. Larsen, A.F. Frangi, P. Larsen, C.A. Perlyn, G.M. Morriss-Kay, and S. Kreiborg. Sparse statistical deformation model for the analysis of craniofacial malformation in the Crouzon mouse. In B.K. Ersbøll and K.S. Pedersen, editors, *Scandinavian Conference on Image Analysis 2007*, volume 4522 of *LNCS*, pages 112–121. Springer, 2007.

[164] H. Ólafsdóttir, S. Lanche, T.A. Darvann, N.V. Hermann, R. Larsen, B.K. Ersbøll, E. Oubel, A.F. Frangi, P. Larsen, C.A. Perlyn, G.M. Morriss-Kay, and S. Kreiborg. A point-wise quantification of asymmetry using deformation fields. application to the study of the Crouzon mouse model. In N. Ayache, S. Ourselin, and A. Maeder, editors, *Medical Image Computing and Computer-Assisted Intervention*, volume 4792 of *Lecture Notes in Computer Science*, pages 452–459, 2007.

[165] H. Ólafsdóttir, T.A. Darvann, N.V. Hermann, P. Larsen, Govier D., A.A. Kane, R. Larsen, B.K. Ersbøll, and S. Kreiborg. Non-rigid registration in craniofacial image analysis: Application to the study of unicoronal synostosis. In *Mouth and Face Forum 2008 - in silico Dentistry, Osaka, Japan (invited contribution)*, 2008.

[166] H. Ólafsdóttir, S. Lanche, T.A. Darvann, N.V. Hermann, K. Sjöstrand, E. Oubel, A.F. Frangi, P. Larsen, C.A. Perlyn, D. Govier, H.D. Hove, J. Hukki, A.A. Kane, G.M. Morriss-Kay, S. Kreiborg, B.K. Ersbøll, and R. Larsen. A volumetric quantification of asymmetry using non-rigid registration. *Transactions on Medical Imaging (submitted)*, 2008.

[167] E. Oubel, H. Neemuchwala, A. Hero, L. Boisrobert, M. Laclaustra, and A.F. Frangi. Assessment of artery dilation by using image registration based on spatial features. *Progress in Biomedical Optics and Imaging - Proceedings of SPIE*, 5747(II):1283–1291, 2005.

[168] D. Pantazis, R.M. Leahy, T.E. Nichols, and M. Styner. Statistical surface-based morphometry using a non-parametric approach. *Biomedical Imaging: Macro to Nano, 2004. IEEE International Symposium on*, pages 1283–1286, 2004.

[169] H. Park, P.H. Bland, and C.R. Meyer. Construction of an abdominal probabilistic atlas and its application in segmentation. *IEEE Transactions on Medical Imaging*, 22(4): 483–492, 2003.

[170] R.R. Paulsen, R. Larsen, S. Laugesen, C. Nielsen, and B.K. Ersbøll. Building and testing a statistical shape model of the human ear canal. In *Medical Image Computing and Computer-Assisted Intervention*, Lecture Notes in Computer Science. Springer, 2002.

[171] M.J. Paulus, S.S. Gleason, M.E. Easterly, and C.J. Foltz. A review of high-resolution X-ray computed tomography and other imaging modalities for small animal research. *Lab Animal*, 30(3):36–45, 2001.

[172] A. Van Pelt, T.A. Darvann, D. Govier, S. Naidoo, M.J. Tenebaum, N.V. Hermann, S. Lanche, H. Ólafsdóttir, P. Larsen, R. Larsen, S. Kreiborg, and A.A. Kane. Longitudinal evaluation of 3D asymmetry following orthotic helmet treatment of deformational plagiocephaly. In *Annual Meeting of the Americal Cleft Palate Craniofacial Association (ACPA) (accepted)*, 2008.

[173] C.A. Perlyn, V.B. DeLeon, C. Babbs, D. Govier, L. Burell, T.A. Darvann, S. Kreiborg, and G. M. Morriss-Kay. The craniofacial phenotype of the Crouzon mouse: Analysis of a model for syndromic craniosynostosis using 3D MicroCT. *Cleft Palate Craniofacial Journal*, 43(6):740–747, 2006.

[174] D. Perperidis, R. Mohiaddin, and D. Rueckert. Construction of a 4D statistical atlas of the cardiac anatomy and its use in classification. *Medical Image Computing and Computer-Assisted Intervention, LNCS*, 3750:402–410, 2005.

[175] D. Perperidis, R.H. Mohiaddin, and D. Rueckert. Spatio-temporal free-form registration of cardiac MR image sequences. *Medical Image Analysis*, 9(5):441–456, 2005.

[176] L.H. Plank, B. Giavedoni, J.R. Lombardo, M.D. Geil, and A. Reisner. Comparison of infant head shape changes in deformational plagiocephaly following treatment with a cranial remolding orthosis using a noninvasive laser shape digitizer. *Journal of Craniofacial Surgery*, 17(6):1084–1091, 2006.

[177] J.P.W. Pluim, J.B.A. Maintz, and M.A. Viergever. Image registration by maximization of combined mutual information and gradient information. *IEEE Transactions on Medical Imaging*, 19(8):809–814, 2000.

[178] J.P.W. Pluim, J.B.A. Maintz, and M.A. Viergever. Mutual-information-based registration of medical images: a survey. *IEEE Transactions on Medical Imaging*, 22(8): 986–1004, 2003.

[179] B.R. Postle, E. Zarahn, and M. D'Esposito. Using event-related fMRI to assess delay-period activity during performance of spatial and nonspatial working memory tasks. *Brain Research Protocols*, 5(1):57–66, 2000.

[180] W. Reardon, R. M. Winter, P. Rutland, L. J. Pulleyn, B. M. Jones, and S. Malcolm. Mutations in the fibroblast growth factor receptor 2 gene cause Crouzon syndrome. *Nature Genetics*, 8:98–103, 1994.

[181] R.F. Recinos, C.C. Hanger, R.B. Schaefer, C.A. Dawson, and A.K. Gosain. Microfocal CT: A method for evaluating murine cranial sutures in situ. *Journal of Surgical Research*, 116(2):322–329, 2004.

[182] J.T. Richtsmeier. Comparative study of normal, Crouzon, and Apert craniofacial morphology using finite element scaling analysis. *American Journal of Physical Anthropology*, 74(4):473–493, 1987.

[183] T. Rohlfing. Transformation model and constraints cause bias in statistics on deformation fields. *Lecture Notes in Computer Science*, 4190:207–214, 2006.

[184] T. Rohlfing, C.R. Maurer Jr, D.A. Bluemke, and M.A. Jacobs. Volume-preserving nonrigid registration of MR breast images using free-form deformation with an incompressibility constraint. *IEEE Transactions on Medical Imaging*, 22(6):730–741, 2003.

[185] D. Rueckert, L.I. Sonoda, C. Hayes, D.L.G. Hill, M.O. Leach, and D.J. Hawkes. Nonrigid registration using free-form deformations: application to breast MR images. *IEEE Trans. on Medical Imaging*, 18(8):712–721, 1999.

[186] D. Rueckert, M.J. Clarkson, D.L.G. Hill, D.J. Hawkes, and Hanson Kenneth M. Nonrigid registration using higher-order mutual information. *SPIE Medical Imaging: Image Processing, San Diego, CA*, pages 438–447, 2000.

[187] D. Rueckert, A.F. Frangi, and J.A. Schnabel. Automatic construction of 3D statistical deformation models of the brain using nonrigid registration. *IEEE Trans. on Medical Imaging*, 22(8):1014–1025, 2003.

[188] J.A. Schnabel, D. Rueckert, M. Quist, J.M. Blackall, A.D. Castellano-Smith, T. Hartkens, G.P. Penney, W.A. Hall, H. Liu, C.L. Truwit, F.A. Gerritsen, D.L.G. Hill, and D.J. Hawkes. A generic framework for non-rigid registration based on non-uniform multi-level free-form deformations. *Fourth Int. Conf. on Medical Image Computing and Computer-Assisted Intervention (MICCAI '01)*, 2208:573–581, 2001.

[189] J.A. Schnabel, C. Tanner, A.D. Castellano-Smith, A. Degenhard, M.O. Leach, D.R. Hose, D.L.G. Hill, and D.J. Hawkes. Validation of nonrigid image registration using finite-element methods: application to breast MR images. *IEEE Transactions on Medical Imaging*, 22(2):238–247, 2003.

[190] S.M. Shah and M.R. Joshi. An assessment of asymmetry in the normal craniofacial complex. *Angle Orthodontist*, 48:141–8, 1978.

[191] C.E. Shannon. A mathematical theory of communication. *Bell Systems Technical Journal*, 27:379–423 and 623–656, 1948.

[192] R. Shekhar and V. Zagrodsky. Mutual information-based rigid and nonrigid registration of ultrasound volumes. *IEEE Trans. on Medical Imaging*, 21(1):9–22, 2002.

[193] X. Shen, H.C. Huang, and N. Cressie. Nonparametric Hypothesis Testing for a Spatial Signal. *Journal of the American Statistical Association*, 97(460):1122–1141, 2002.

[194] G.D. Singh, J.A. McNamara, and S. Lozanoff. Thin-plate spline analysis of the cranial base in subjects with Class III malocclusion. *The European Journal of Orthodontics*, 19(4):341, 1997.

[195] G.D. Singh, J. Rivera-Robles, and J. de Jesus-Vinas. Longitudinal Craniofacial Growth Patterns in Patients With Orofacial Clefts: Geometric Morphometrics. *The Cleft Palate-Craniofacial Journal*, 41(2):136–143, 2003.

[196] K. Sjöstrand, M.B. Stegmann, and R. Larsen. Sparse principal component analysis in medical shape modeling. In *International Symposium on Medical Imaging 2006, San Diego, CA, USA*, volume 6144. The International Society for Optical Engineering (SPIE), 2006.

[197] K.V. Skoglund, M.B. Stegmann, C. Ryberg, H. Ólafsdóttir, and E. Rostrup. Estimation and perturbation of the mid-sagittal plane and its effects on corpus callosum morphometry. In *Proc. International Society of Magnetic Resonance In Medicine - ISMRM 2005, Miami, Florida, USA*. ISMRM, 2005.

[198] X. Song, E.C. Frey, and B.M.W. Tsui. Development and evaluation of a MicroCT system for small animal imaging. *IEEE Nuclear Science Symposium and Medical Imaging Conference*, 3:1600–1604, 2001.

[199] M. Sonka and J. M. Fitzpatrick, editors. *Medical Imaging - Vol. 2. Medical Image Processing and Analysis*. SPIE - The International Society for Optical Engineering, 2000.

[200] D. St John, J.B. Mulliken, L.B. Kaban, and B.L. Padwa. Anthropometric analysis of mandibular asymmetry in infants with deformation al posterior plagiocephaly. *Journal of Oral and Maxillofacial Surgery*, 60(8):873, 2002.

[201] J. Staubesand, editor. *Atlas of Human Anatomy*. Urban & Scwarzenberg, 20 edition, 1989.

[202] M.B. Stegmann. *Active Appearance Models: Theory, Extensions and Cases*. Informatics and Mathematical Modelling, Technical University of Denmark, DTU, Richard Petersens Plads, Building 321, DK-2800 Kgs. Lyngby, 2 edition, 2000.

[203] M.B. Stegmann, H. Ólafsdóttir, and H.B.W. Larsson. Unsupervised motion-compensation of multi-slice cardiac perfusion MRI. *Medical Image Analysis*, 9(4):394–410, 2005.

[204] C. Studholme, D.L.G. Hill, and D.J. Hawkes. An overlap invariant entropy measure of 3D medical image alignment. *Pattern Recognition*, 32(1):71–86, 1999.

[205] C. Studholme, R.T. Constable, and J.S. Duncan. Accurate alignment of functional EPI data to anatomical MRI using a physics-based distortion model. *IEEE Transactions on Medical Imaging*, 19(11):1115–1127, 2000.

[206] C. Studholme, V. Cardenas, A. Maudsley, and M. Weiner. An intensity consistent filtering approach to the analysis of deformation tensor derived maps of brain shape. *NeuroImage*, 19(4):1638–1649, 2003.

[207] C. Studholme, V. Cardenas, R. Blumenfeld, N. Schuff, and H.J. Rosen. Deformation tensor morphometry of semantic dementia with quantitative validation. *NeuroImage*, 21(4):1387–1398, 2004.

[208] M. Styner and G. Gerig. Medial models incorporating object variability for 3d shape analysis. *Lecture Notes in Computer Science*, 2082:502, 2001.

[209] M. Styner, G. Gerig, J. Lieberman, D. Jones, and D. Weinberger. Statistical shape analysis of neuroanatomical structures based on medial models. *Medical Image Analysis*, 7(3):207, 2003.

[210] G. Subsol, J-P. Thirion, and N. Ayache. A scheme for automatically building three-dimensional morphometric anatomical atlases: application to a skull atlas. *Medical Image Analysis*, 2(1):37–60, 1998.

[211] P. Svanholt and B. Solow. Assessment of midline discrepancies on the postero-anterior cephalometric radiograph. *Trans Eur Orthod Soc*, 1:261–8, 1977.

[212] J.E. Taylor and K.J. Worsley. Random fields of multivariate test statistics, with applications to shape analysis. annals of statistics. *Annals of Statistics (accepted)*, 2007.

[213] S.J. Teipel, C. Born, M. Ewers, A.L.W. Bokde, M.F. Reiser, H.J. Mller, and H. Hampel. Multivariate deformation-based analysis of brain atrophy to predict alzheimer's disease in mild cognitive impairment. *Neuroimage*, 38(1):13–24, 2007.

[214] D. Terzopoulos. Regularization of inverse visual problems involving discontinuities. *IEEE Transactions on Pattern Analysis and Machine Intelligence*, 8(4):413–242, 1986.

[215] P. Thevenaz and M. Unser. Optimization of mutual information for multiresolution image registration. *IEEE Transactions on Image Processing*, 9(12):2083–2099, 2000.

[216] J.P. Thirion. Image matching as a diffusion process: an analogy with Maxwell's demons. *Medical Image Analysis*, 2(3):243–260, 1998.

[217] H.H. Thodberg and H. Ólafsdóttir. Adding curvature to minimum description length shape models. In *Proceedings of the British Machine Vision Conference*, volume 2, pages 251–260, 2003.

[218] C.E. Thomaz, J.P. Boardman, S. Counsell, D.L.G. Hill, J.V. Hajnal, A.D. Edwards, M.A. Rutherford, D.F. Gillies, and D. Rueckert. A whole brain morphometric analysis of changes associated with pre-term birth. *Progress in Biomedical Optics and Imaging - Proceedings of SPIE*, 6144 III:1903–10, 2006.

[219] D.A.W. Thompson. On growth and form. The complete revised edition. *Cambridge University.(Original work published 1917)*, 1992.

[220] P.M. Thompson and A.W. Toga. Detection, visualization and animation of abnormal anatomic structure with a deformable probabilistic brain atlas based on random vector field transformations. *Medical Image Analysis*, 1(4):271–294, 1997.

[221] P.M. Thompson, J.N. Giedd, R.P. Woods, D. MacDonald, A.C. Evans, and A.W. Toga. Growth patterns in the developing brain detected by using continuum mechanical tensor maps. *Nature*, 404(6774):190–3, 2000.

[222] P.M. Thompson, J. Moussai, S. Zohoori, A. Goldkorn, A.A. Khan, M.S. Mega, G.W. Small, J.L. Cummings, and A.W. Toga. Cortical variability and asymmetry in normal aging and Alzheimer's disease. *Cerebral Cortex*, 8:492–509, 2003.

[223] T. Thyagarajan, S. Totey, M.J. Danton, and A.B. Kulkarni. Genetically altered mouse models: the good, the bad, and the ugly. *Critical reviews in oral biology and medicine*, 2003.

[224] B. Trpkova, P. Major, B. Nebbe, and N. Prasad. Craniofacial asymmetry and temporomandibular joint internal derangement in female adolescents: A posteroanterior cephalometric study. *Angle Orthodontist*, 70(1):81–88, 2000.

[225] C.J. Twining, T. Cootes, S. Marsland, V. Petrovic, R. Schestowitz, and C.J. Taylor. A unified information-theoretic approach to groupwise non-rigid registration and model building. *Proceedings of IPMI*, pages 1–14, 2005.

[226] M. Vaillant, A. Qiu, J. Glaunes, and M.I. Miller. Diffeomorphic metric surface mapping in subregion of the superior temporal gyrus. *Neuroimage*, 34(3):1149–1159, 2007.

[227] L. Van Valen. A study of fluctuating asymmetry. *Evolution*, 16(2):401–415, 1962.

[228] L.A. van Vlimmeren, T. Takken, L.N.A. van Adrichen, Y. van der Graaf, P.J.M. Helders, and R.H.H. Engelbert. Cplagiocephalometry: a non-invasive method to quantify asymmetry of the skull; a reliability study. *European Journal of Pediatrics*, 165:149–157, 2006.

[229] M. Vester-Christensen, S. G. Erbou, S. Darkner, and R. Larsen. Accelerated 3D image registration. *International Symposium on Medical Imaging 2007, San Diego, CA*, 2007.

[230] P.S. Vig and A.B. Hewitt. Asymmetry of the human facial skeleton. *Angle Orthodontist*, 45:125–9, 1975.

[231] P. Viola and W. M. Wells. Alignment by maximization of mutual information. *International Journal of Computer Vision*, 24(2):137–154, 1997.

[232] L. Wang, S.C. Joshi, M.I. Miller, and J.G Csernansky. Statistical analysis of hippocampal asymmetry in schizophrenia. *NeuroImage*, 14(3):531, 2001.

[233] W.M. Wells, P. Viola, H. Atsumi, S. Nakajima, and R. Kikinis. Multi-modal volume registration by maximization of mutual information. *Medical Image Analysis*, 1(1): 35–51, 1996.

[234] K.J. Worsley, J.E. Taylor, F. Tomaiuolo, and J. Lerch. Unified univariate and multivariate random field theory. *Neuroimage*, 23:189–195, 2004.

[235] J. Wouters, E. D'Agostino, F. Maes, D. Vandermeulen, and P. Suetens. Non-rigid brain image registration using a statistical deformation model. *Medical Imaging 2006: Image Processing*, 6144:338–345, 2006. doi: 10.1117/12.653081.

[236] A. Xhiahai and L. Gu. Normal vector information registration and comparisons with mutual information. *Engineering in Medicine and Biology Society, EMBS 2006. 28th Annual International Conference of the IEEE*, pages 3827–3830, 2006.

[237] Z. Xue, D. Shen, and C. Davatzikos. Statistical representation of high-dimensional deformation fields with application to statistically constrained 3D warping. *Medical Image Analysis*, 10(5):740–751, 2006.

[238] L. Zhang, E.A. Hoffman, and J.M. Reinhardt. Atlas-driven lung lobe segmentation in volumetric X-ray CT images. *IEEE Transactions on Medical Imaging*, 25(1):1–16, 2006.

[239] G. Zhijun and Q. Binjie. Multi-modal and multi-temporal image registration in the presence of gross outliers using feature voxel-weighted normalized mutual information. *Nuclear Science Symposium Conference Record, 2006. IEEE*, 6:3209–3212, 2006.

[240] B. Zitova and J. Flusser. Image registration methods: a survey. *Image and Vision Computing*, 21(11):977–1000, 2003.

[241] H. Zou and T. Hastie. Regularization and variable selection via the elastic net. *Journal of the Royal Statistical Society: Series B (Statistical Methodology)*, 67(2):301–320, 2005.

[242] H. Zou, T. Hastie, and R. Tibshirani. Sparse principal component analysis. *Journal of Computational and Graphical Statistics*, 15(2):265, 2006.